Development of Low-Temperature Ammonia Cracking Catalysts

Thesis submitted to the University of Nottingham for the degree of Doctor of Philosophy

November 2024

Corrected July 2025

Benjamin James Young

14288288

Supervisor: Jesum Alves Fernandes

School of Chemistry, Faculty of Science

University of Nottingham

Declaration

This thesis is the result of my own investigations and is not being concurrently submitted in candidature for any degree.

Signed: B.young

Date: 29/11/2024

1. Table of Contents

Abstract

Hydrogen shows promise as the energy vector of the future, but problems with storage and transport are significant. Storage of hydrogen as ammonia has the potential to solve these problems, but current catalysts for its cracking are not efficient enough to enable the large-scale application of ammonia. Carbon materials, such as carbon nanotubes (CNTs), have shown potential as supports for ammonia decomposition catalysts. This thesis investigates the use of graphitised nanofibers (GNFs), which offer high purity and graphitisation, as a support material for Ru catalysts. Ru/GNF was synthesised using magnetron sputtering and tested for catalytic activity in ammonia decomposition and the catalyst exhibited self-improvement over the course of the reaction. The evolution of the Ru nanoclusters on GNF was studied by Identical Location Scanning Transmission Electron Microscopy (IL-STEM). The analysis revealed that the Ru nanoclusters undergo significant morphological changes during the reaction - transforming from flat and amorphous structures to more three-dimensional crystalline nanoclusters. The step-edges on the GNF surface help to stabilise the Ru nanoclusters, preventing excessive growth and maintaining a high density of active sites. Spectroscopic analysis using in-operando EXAFS and ex-situ XPS provide further insights into the mechanism behind the self-improvement. EXAFS data suggest that the Ru nanoparticles undergo bulk nitridation during the reaction. This is supported by XPS analysis, which confirms the formation of a metal nitride species. It is proposed that the formation of bulk nitrided Ru nanoclusters leads to a change in the reaction mechanism, increasing the number of active sites and enhancing the catalyst's activity. This thesis highlights the importance of studying the dynamic behaviour of catalysts and provides an understanding of the self-improvement mechanism in Ru/GNF. This knowledge can contribute to the design of more efficient and stable catalysts for low-temperature ammonia cracking, advancing sustainable hydrogen production technologies.

Acknowledgements

Firstly, I would like to thank my supervisor Jesum Alves Fernandes. Quite frankly without your unwavering support over the years, I wouldn't have made it here. Thank you for advising when I needed advice, listening when I needed an ear, and being stern when I needed a bit of that too.

I would also like to thank Yifan, Andrei, Gazi and Wolfgang for the contributions made to this project – the best collaborators I could wish for. A shoutout to Gazi for being an incredible microscopist and a wonderful human being. I would like to thank the School of Chemistry, the NMRC and all the technicians I have worked with through the years (especially to Sam Tang for making me feel so welcomed). Finally, a special thanks to Mark Guyler and Sam Kilgour for keeping the ICP machine going despite its own long-awaited desire to retire.

I would like to thank all the folks in my group and my lab through the years: Andreas, Emerson, Tom, Hiba, Hamza, Ryan, Luke, Matt, Rob (and everyone else that I have certainly forgotten). Your help, conversations and support have helped me through one of the hardest times of my life.

I'd like to say a special thank you to Pekka. There was a time during my studies that I felt isolated and my days were spent silently, but you always made the effort to stop me in the corridor and lift that loneliness a little.

I would like to thank my family and my friends. Thank you to my parents for encouraging me into science – it has been the journey of a lifetime. Thank you to my brother and sister for the time we have spent together – I know that we haven't always been close, but I am so excited for the future. Thank you to Isaac for hearing me, to Archie for reigniting my fire and to Ewan for your steadfast companionship.

Finally, I would like to thank my love, Michaela - these years have been tough on you the most. Thank you for your patience, your kindness and your care. Here's to our little family, and to many more years to come.

2. Background and Introduction

2.1. Hydrogen

The shift towards renewable energy is urgent. The environmental concerns associated with burning fossil fuels, their depletion and the instability of crude oil harvesting regions is accelerating the shift towards renewable energy. As such, in recent years there has been an increasing interest in the study of replacements to fossil fuels – a concept known as "energy transition".[1] One of the first explored, most promising and most studied of these replacements has been H_2 due to its high energy density and ease of production using green energy.[2] The "hydrogen economy" as a concept was first introduced in 1972 in a proposition to base the energy transition on the use of hydrogen as a vector for generation of clean and environmentally sustainable energy.[3] Over the last few decades the production, transportation, storage and use of hydrogen to provide low emission energy have been extensively investigated.[4] Hydrogen is currently mostly supplied by steam reforming of methane (SMR) and subsequent water-gas shift (WGS), which is a well-established commercial technology and is currently the least expensive way to produce hydrogen on a large scale. From SMR and WGS, 5.5 kg of CO_2 is produced per kilogram of H_2 from the reaction alone without considering carbon costs of the energy required to run the reaction. Taking this into account, close to 10 kg of CO_2 is produced per kilogram of H_2, vastly diminishing the environmental appeal.[5] Although the electrolysis of water is a well-known and established technology which produces clean, high purity hydrogen; it suffers from heavy energy losses.[6] A large cost reduction of the electricity from renewable sources and electrolysers would be needed to compete with conventional energy sources on a large scale.[7] It's not hyperbole to say that the decoupling of our society from its addiction to fossil fuels will be one of the biggest efforts that humanity will ever undertake, and that the results that effort will determine the course of the planet's future.

Currently, most of the hydrogen produced is used on-site in industry, mainly for ammonia production and petroleum refining, which account for two-thirds of total hydrogen use.[8] Hydrogen is an explosive gas, and the storage of it in pressurised and cooled tanks is dangerous and inefficient. Although hydrogen is a good potential future energy vector, the problems of safety and cost arise when large amounts are produced to store energy.

A key challenge of a hydrogen economy is therefore its storage and transport. Hydrogen is incredibly difficult to store due to its tendency to diffuse through materials, leading to embrittlement and weakening of the storage material.[9] Further, in its most common storage method (as compressed gas), hydrogen has a very low energy density by volume at pressures up to 700 bar at room temperature.[10] Whilst it can also be stored as a liquid at low temperatures (-253 °C, 1 bar) resulting in a higher energy density, there are serious energy costs associated with the low temperatures.

Other methods for hydrogen storage include adsorption onto high surface area materials and direct chemical storage. In adsorption, hydrogen is captured on materials such as carbon nanotubes through low temperatures and high pressures. In direct chemical storage, hydrogen acts as a reagent to form hydrogen-rich compounds that are easier to transport.[11] These compounds are later decomposed to release the stored hydrogen. Examples of such materials include organic compounds that can be hydrogenated and dehydrogenated, such as cyclic hydrocarbons (e.g., converting benzene to cyclohexane), and metal hydrides. However, both of these options have relatively low hydrogen storage densities. This thesis will focus on ammonia as an emerging hydrogen storage material.[12]

The storage of hydrogen as ammonia is a very attractive option due to the high hydrogen storage density (17.6 wt%) and the maturity of its synthesis, handling, and transportation processes. Ammonia can liquefy at low pressure (8.6 bar at 20 °C), so its transport and storage are relatively easy and require a low amount of energy.[13,14] Another great advantage of ammonia is that when it is decomposed, it produces high purity hydrogen. The equilibrium conversion of ammonia decomposition is 99 to 99.7% at 400 °C and 500 °C respectively at 1 atm. The hydrogen produced by this reaction is, importantly, CO_x free which is a requirement in Proton-Exchange Membrane Fuel Cells (PEMFCs).[15]

2.1.1. Ammonia as a Hydrogen Storage Medium

The hydrogen storage capacity of ammonia was evaluated by Klerke *et al.* in 2008,[13] showing that the volumetric storage density of ammonia was 7.7 times that of gaseous hydrogen at 200 bar and 1.5 times that of liquid hydrogen. Further, apart from pure hydrogen, ammonia had the highest gravimetric hydrogen storage density at 10.4 wt%. These findings are illustrated in Figure 2.1.

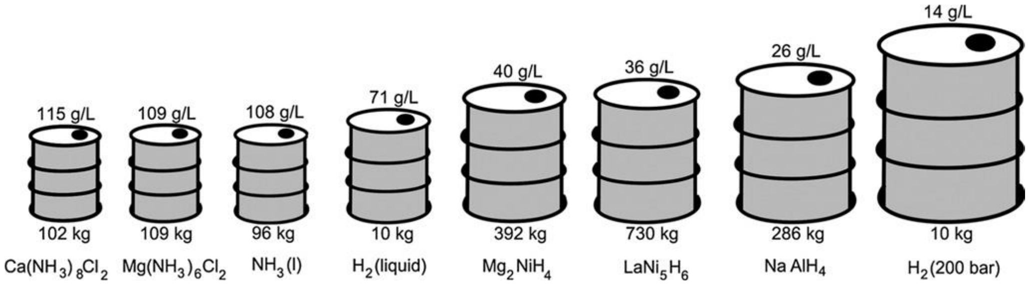

Figure 2.1. Mass and volume of 10 kg hydrogen stored reversibly by 8 different methods, based on the best obtained reversible densities reported in the literature without considering the space or weight of the container. Directly reproduced from Klerke et al.[13]

Ammonia is already widely stored and distributed thanks to its ubiquitous use in the agricultural industry as a main component of fertilisers. Ammonia synthesis is one of the oldest industrial processes and as such has a very mature existing infrastructure, exemplified by the US, which has 4800 km of ammonia pipelines that can transport 2 Mt of ammonia per year.[16] Ammonia is typically stored as a liquid at 10 bar in small quantities (below 1500 t) and as a liquid at 238 K in larger quantities.[13]

Ammonia is produced predominantly through the Haber-Bosch process from H_2 and N_2. This process typically operates over an Fe based catalyst at temperatures of 400-500 °C and pressures of 100-300 atm.[17] The hydrogen is produced mainly through steam reforming methane, a process by which the methane is reacted with water to produce gaseous H_2, CO and CO_2. In fact, this process emits close to 10 kg of CO_2 per kg of H_2 produced and is the source of nearly 3% of global industrial sector CO_2 emissions.[18] The world consumption of ammonia has increased over time as NH_3 uses have become more widespread in both agriculture and industry. In 2018, the world ammonia production was around 150 million metric tons.[19]

In the application of ammonia as a hydrogen storage medium, equally important to its synthesis is its decomposition, or "cracking". In the cracking reaction, ammonia is flowed over a catalyst bed at high temperatures, decomposing the ammonia into its constituent hydrogen and nitrogen. This process will be discussed in detail later.

The most important areas for technical improvement in hydrogen storage in ammonia was identified as insufficient catalytic activity of commonly used catalyst by Schuth *et al.* in their review of hydrogen storage in ammonia.[20] This view is similarly held by the U.S. Department of Energy (DoE) who showed that the efficiency of catalytic ammonia cracking systems must increase by around 100 times.[21] This came with a recommendation that research should focus on the reduction of temperature to align with conditions onboard a PEM fuel-cell vehicle, operating at around 370 K.

The safety issues related to ammonia are also of concern. In particular, the toxicity, smell and social acceptance of ammonia are amongst the most important factors. Ammonia is very commonly used as an agrochemical and industrial chemical, where its safe handling is very well understood. This being said, Schuth *et al.* believed that despite the feasibility of scaling and applying the infrastructure, the storage in cars in liquid or gaseous form would probably not be tolerated due to its toxicity and smell.[20] The corrosive nature of ammonia, especially when exposed to a small amount of moisture is also of concern – especially in large scale long-term storage applications, where a leak could result in a large exposure.

Ammonia is classified as a poisonous gas with a safe exposure limit of 50 ppm for an immediate exposure, 35 ppm for short term (<15 mins) and a time weight average exposure limit of 25 ppm over 8 hours.[21] The health effects range from “no discomfort for prolonged exposure” below 100 ppm, to “immediate fatality” at concentrations above 10,000 ppm (1 %).

Further regarding safety, it is also important to consider the flammability of ammonia compared to other fuels. In their 2020 perspective on the use of ammonia as a clean fuel, Erdemir and Dincer reported the flammability limits of a number of common fuels, compared to ammonia.[22] For ammonia, the concentration in air that would be required for flammability is far higher than that of gasoline, 16.25 vol% compared to 1.4 - 7.5 vol%. This is also significantly higher than LPG at 1.81 - 8.86 vol% and CNG at 5.0 – 15.0 vol%. As a result, an ammonia leak presents a vastly reduced flammability risk than similar fossil fuel leaks. The flammability risk of hydrogen by comparison is huge, due to its flammability limits of 4-75 vol%.

One thing to note is that the odour of ammonia is detectable at concentrations as low as 5 ppm and becomes readily detectable above 20 ppm. Small spills, leaks etc, around filling stations (that are to be expected) could have a cumulative effect on ammonia concentrations in the vicinity. The overall effect this will have on public perception of ammonia as a fuel is very likely to be negative.[20] This being said, its smell can also act as a safety measure – ammonia is easily detected well below its exposure limit, which means that there is very little chance of exposure without knowledge.

The US Department of Energy (DoE) reviewed the case of safety and public perception of ammonia, and recommended that further research should be conducted into lightweight indestructible tanks, cheap ammonia detectors and a better understanding of the health effects of ammonia exposure.[21]

To conclude, ammonia is a very promising hydrogen storage medium owing to its high density of storage and the maturity of its processes of synthesis and handling. The sustainability of ammonia as a hydrogen storage medium depends heavily on the development of better catalysts for both ammonia synthesis and cracking.[17,23] Although ammonia is much less flammable than current fuels, the safety of ammonia is questionable due to the toxicity hazard that it poses. Overall, it seems unlikely that ammonia will see use on the small scale of personal vehicles but is very likely to be used on larger scale in transportation and shipping.

The focus of this thesis be to explore the development of novel catalysts for ammonia cracking at low temperatures.

2.2. *Catalysis*

It is difficult to overstate the role that catalysis plays in 21st century life. All around us are the results of countless different reactions. Plastic products are a prime example of numerous catalysed steps such as cracking (the breaking down of large molecules in crude oil into smaller, useful molecules) and polymerisation (building up of small molecules into repeating chains) that allow preparation from raw materials.[24-26] In fact catalysts are of such importance that 80% of chemical reactions in industry are accomplished in the presence of a catalyst.[27,28]

2.2.1. What is a catalyst?

A catalyst is a substance that can reduce the activation energy of a reaction, thereby increasing the reaction rate. It does this by reacting with the reagents to form intermediate species, splitting the reaction into multiple steps with lower energy transition states.[29] These lower energy transition states result in a lower activation energy, which causes the reaction to proceed quicker and sometimes more selectively than in the absence of a catalyst. A catalyst participates in the reaction but is not consumed in the process. As a result, it can participate in many cycles of the reaction and thus, it does not need to be present in stoichiometric amounts to catalyse a large quantity of reactant molecules.[27,28] Catalysts do degrade over many cycles of the reaction in different ways depending on the nature of the catalyst and much of the field of catalysis focuses on the resistance of the catalyst to degradation.

Catalysts can broadly be split into 2 categories which describe their state of matter. Homogeneous catalysts are those that are in the same phase as the reactants, e.g. solution phase catalysts in a solution phase reaction. Heterogeneous catalysts are those in a different phase to the reactants, e.g. a solid catalyst in a gas phase reaction. Both types of catalyst have their drawbacks. Homogenous catalysts are usually highly active but more difficult to recycle/reuse, are less stable and are expensive. Heterogeneous catalysts generally have lower activity and selectivity but are usually preferred due to their recoverability. This is economically important in industry and aligns with sustainability goals, such as offering low-energy routes to products.[30,31] In this thesis, the focus will be placed on heterogeneous catalysts.

2.2.2. Why are catalysts needed?

Catalysts play a critical role in various industries for different reasons including legislative requirements, economic benefits, and most of all necessity (reactions that will not occur under reasonable conditions without a catalyst). Firstly, in processes like ammonia synthesis, it would be impossible to meet the quantity demands of bulk chemical production without the use of a catalyst. In the automotive industry, legal pressures have resulted in the ubiquitous use of catalytic converters to meet increasingly strict emissions regulations, which in turn drives ongoing research and improvement of these catalysts.[32,33] Economically, catalysts pose several advantages. By enabling reactions at lower temperatures and pressures, they save significantly on both set-up costs and running costs. High-pressure systems are particularly expensive and high running costs are unavoidable with high-temperature and high-pressure reactions.

Further, developing more selective catalysts can increase the yield of the desired product and reduce the need for post-reaction purification, which boosts profitability and efficiency in industrial operations.

2.3. *Ammonia Synthesis: A Case Study for Catalysis*

Ammonia synthesis is key to the development of an ammonia economy and is an excellent case study into the application of heterogeneous catalysts into an industrial reaction. This brief study will also serve another purpose; as with many forward and reverse reactions, ammonia synthesis is deeply linked to ammonia decomposition, which is the focus of this thesis. By first covering the basics of ammonia synthesis, we will come to a deeper understanding of the ammonia decomposition reaction.

2.3.1. A Short History of Ammonia

In 1798, Thomas Malthus famously proposed his principle that population of humanity increases in a geometrical ratio, whereas the subsistence for humanity increases in an arithmetical ratio.[34] In simpler words, the population increases exponentially whereas the food produced increases only linearly. Soon it became clear that Malthus was right, and that food would very soon become scarce if we could not augment crop yield. It was found in 1847 by Justus von Liebig that the source of nitrogen in plants was in fact ammonia, and therefore that one of the most important components of fertiliser was “fixed” nitrogen.[35] At the time, most fixed nitrogen was produced from the production of coke from coal, but nitrogenous fertiliser also began to be imported from Chile to Europe, in the form of sodium nitrate.

Fixed nitrogen was also increasingly being used for other purposes such as dyes and explosives, necessary for the military and mining. As such, at the turn of the 20th century, it became clear that the natural supply of fixed nitrogen could not keep up with demand and that something must be done.

In 1898, Sir William Crookes made a famous speech during his presidential address to the British Association for the Advancement of Science. He stated that, *"all civilized nations stand in deadly peril of not having enough to eat,"* and that, *"it is the chemist who must come to the rescue of the threatened communities. It is through the laboratory that starvation may ultimately be turned into plenty."*[36]

In 1895 Frank and Caro discovered the first industrially and economically applicable chemical reaction to fix atmospheric nitrogen – that being the cyanamide process. The reaction is exothermic, and although it requires temperatures of about 1000 °C, it is self-sustaining once the reaction temperature is reached. For the next 20 or so years, fixed nitrogen was produced primarily through the Frank-Caro process.

Fritz Haber and his assistant Robert de Rossignol began their work on the catalytic production of ammonia from atmospheric nitrogen in 1904, eventually achieving high-pressure success at 200 atm. BASF had a keen interest in the reaction and sent 2 engineers, Bosch and Mittasch, to visit Haber's laboratory, which sparked the development of the reaction to industrial scale. Haber was awarded a Nobel Prize in 1919 for his study of the synthesis of ammonia, and Bosch later received the Nobel Prize in 1931 for his application of high-pressure technology in the Haber-Bosch process.

The Haber-Bosch process today is responsible for more than 40% of food production.[37] As the largest chemical process in the world, it consumes more than 2% of the worlds energy and accounts for 1.6% of total global CO_2 emissions.[38]

2.3.2. Thermodynamics and Kinetics of Ammonia Synthesis

The Haber-Bosch process is typically conducted in industry in large plants (1000 to 1500 t/day) at temperatures in the range of 400–500°C and pressure in the range of 150-300 atm.[39] The equation for the reaction is seen in equation 1, alongside the enthalpy change of the reaction:

Equation 1. Ammonia synthesis reaction

$$\mathrm{N_2 + 3H_2 \rightleftharpoons 2NH_3} \quad \Delta\mathrm{H}° = -92\ \mathrm{kJmol^{-1}}$$

As per Le Chatelier's principle, in ammonia synthesis, the formation of ammonia is favoured by high pressure. This would reduce the overall number of molecules present, thus decreasing the overall pressure. The enthalpy change for the forward reaction is negative (exothermic), and thus the reaction would be higher yielding at lower temperatures due to the equilibrium shifting to the right (increasing equilibrium constant).[40] However kinetically speaking, the rate of reaction would be too slow for equilibrium to be reached at normal temperatures, so a trade-off temperature of about 450 °C is used.

The mechanism for ammonia synthesis was reported in 1980 by Gerhard Ertl, as seen in Equation 2.

Equation 2. The sequence of elementary steps involved in the synthesis (and decomposition) of ammonia on iron, as reported by Ertl et al. in 1980.[41]

$$H_2 \rightleftharpoons 2\,\mathrm{H}_{ad}$$

$$N_2 \rightleftharpoons N_{2,ad} \rightleftharpoons 2\,N_{ad}$$

$$\mathrm{N_{ad} + H_{ad} \rightleftharpoons NH_{ad}}$$

$$NH_{ad} + H_{ad} \rightleftharpoons NH_{2,ad}$$

$$NH_{2,\mathrm{ad}} + H_{\mathrm{ad}} \rightleftharpoons NH_{3,\mathrm{ad}} \rightleftharpoons NH_3$$

The rate determining step of the synthesis reaction was also determined to be the N_2 dissociation under "normal" N_2:H_2 partial pressure ratios and at ≥300°C. Interestingly in the same work, it was also reported that for the reverse reaction, ammonia decomposition, the inverse of this step (recombination of adsorbed atomic nitrogen) was rate limiting, which we will revisit later.

2.3.3. Catalysts for Ammonia Synthesis

After the development of the multi-promoted iron catalyst based on magnetite by Mittasch,[42] the most used industrial catalyst has remained remarkably similar.[43] Iron catalysts are based on magnetite ore (Fe_3O_4) with structural promoters for stability (e.g. Al_2O_3, CaO, MgO, SiO_2) and electronic promoters to increase activity (e.g. K_2O). These are mostly used in industry due to thermal stability and chemical stability against oxygen species. In a typical reaction, the catalyst is activated *in-situ* by reduction of the iron oxide to metallic iron. Promoters mostly remain in their oxide form.

Later studies on iron catalysts focused on supported iron nanoparticles. Studies by Dumesic *et al.* showed that the ammonia synthesis over Fe/MgO is surface sensitive - the rate of ammonia synthesis was increased over larger iron particles when compared to smaller particles.[44] This would not normally be expected, as a smaller nanoparticle would lead to high surface area and therefore increased rate. In following work, Dumesic *et al.* showed that ammonia treatment of the surface of iron decreases surface anisotropy, and that C7 sites were some of those with the lowest surface anisotopy.[45] C7 sites – iron atoms with 7 nearest neighbours. In other words, the effect of ammonia treatment on the surface of iron catalysts is the production of C7 sites. Further investigation of these materials showed the most active site for the reaction is the C7 site.[46,47]

In more recent years, ruthenium (Ru) has emerged as the most active catalyst metal for ammonia synthesis and has since been commercialised.[48] In Ru catalysts, the B5 site rather than the C7 is recognised as the most active site and as such, the size and morphology of the most active site is different. The B5 site occurs on a step edge where 3 atoms of Ru occupy one layer and 2 atoms are positioned in the layer above, as seen in the Figure 2.2 insert "Ru(0001) surface". Where C7 sites are favoured in larger particles, B5 sites are most abundant in particles with sizes between 1.8 and 2.5 nm – as shown in Figure 2.2.

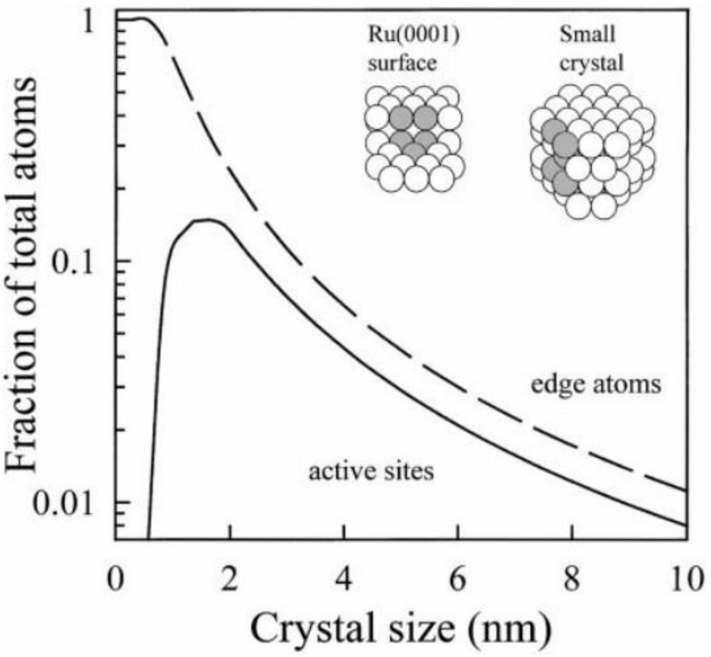

Figure 2.2. Fraction of edge atoms and active sites on small Ru crystals relative to total number of atoms, as a function of crystal size. Reproduced from Jacobsen et al.[49]

Ruthenium catalysts have a tendency to be less stable than their iron cousins,[50] which is likely a result of the size dependency on the active site as discovered by Jacobsen *et al.* It is, therefore, important for Ru catalysts to be held by a stable support material that prevents the deactivation of the Ru by sintering in ammonia synthesis.[51] It has also been shown that electronic promotion has a very strong positive effect on the catalysis of ammonia synthesis. Ba, Cs and K were shown by Kowalczyk *et al.* to promote Ru. Cs and K promotion occurs via electron transfer from the alkali to the active metal. The promotion pathway of Ba is more debated, but it either acts as a structural support modifying local Ru arrangement, or as an electronic promoter like alkali metals.

2.3.4. Summary

Ammonia synthesis is a cornerstone of industrial chemistry. It's development has not only shaped global agricultural practice, allowing us to support an ever-increasing population, but also laid the foundation for modern catalysis.

Thermodynamically, ammonia synthesis is favoured by high pressures and low temperatures but is kinetically hindered under these conditions. Industrial operation requires a compromise, typically around 450 °C and 150–300 atm, to balance yield and reaction rate. Mechanistic studies by Ertl and co-workers in 1980 revealed the dissociation of molecular nitrogen as the rate-determining step in synthesis, and conversely, the recombination of atomic nitrogen as rate-limiting in decomposition.

Catalyst development has historically centred on iron-based systems, particularly magnetite-derived materials promoted with structural and electronic additives. These catalysts remain dominant due to their robustness and cost-effectiveness. However, the discovery of structure-sensitive activity, particularly the role of C7 sites on iron surfaces, has refined our understanding of active site architecture. More recently, ruthenium has been further studied as a superior catalytic metal, with B5 sites identified as the most active for ammonia synthesis. The size-dependence of these sites, and the associated stability challenges, have necessitated the development of advanced support materials and electronic promoters to maintain catalytic performance.

This overview of ammonia synthesis not only illustrates the principles of gas-phase heterogeneous catalysis but also to establishes the historical and scientific context for the detailed investigation of ammonia decomposition. By understanding the synthesis process in depth, we are better equipped to explore its reverse—an essential reaction in the context of hydrogen storage and the emerging ammonia economy.

2.4. Ammonia Decomposition

The reverse reaction of ammonia synthesis is the catalytic decomposition of ammonia (also called cracking). This process occurs at atmospheric pressure, and conventionally requires temperatures upwards of 550 °C for complete conversion due to the endothermicity of the reaction.[52] Catalytic ammonia decomposition has long been studied in the past as a convenient method for gaining insight into the mechanism for ammonia synthesis.[53-57] In recent years, focus has shifted towards low-temperature production of clean H_2, where low-temperature is considered to be 450 °C and below, as at these temperatures conventional catalysts show very low conversion.[15,52,58,59]

2.4.1. Mechanism and Reaction Scheme

Ammonia decomposition is an endothermic process (as seen in equation 2), meaning that thermodynamically, it is favoured by a high temperature. As per Le Chatelier's principle, due to the increase in number of molecules produced, the reaction is favoured by a low pressure.

Equation 3. Ammonia decomposition reaction

$$2NH_3 \rightleftharpoons N_2 + 3H_2 \qquad \Delta H^\circ = 92\ kJmol^{-1}$$

Below is the mechanism for ammonia decomposition, as laid out by Ertl *et al.* in 1980 in an investigation of the decomposition of ammonia over single Fe crystal surfaces. This mechanism is also illustrated in Figure 2.3.

Equation 4. Ammonia decomposition mechanism

$$\mathrm{NH_3} \rightleftharpoons \mathrm{NH_{3,ad}} \rightarrow \mathrm{NH_{2,ad}} + \mathrm{H_{ad}} \rightarrow \mathrm{NH_{ad}} + 2\,\mathrm{H_{ad}} \rightarrow \mathrm{N_s} + 3\,\mathrm{H_{ad}}$$

$$2\,H_{ad} \rightarrow H_2$$

$$2\,N_s \rightarrow N_2$$

Where N_s denotes "surface nitride" species. NH_3 first adsorbs onto the surface (Figure 4. a) and N-H bonds are sequentially cleaved (Figure 2.3. b). This leaves adsorbed H (H_{ad}), and eventually, a N_s species. Finally, two surface nitrides recombine to form N_2, which desorbs (Figure 2.3. c).

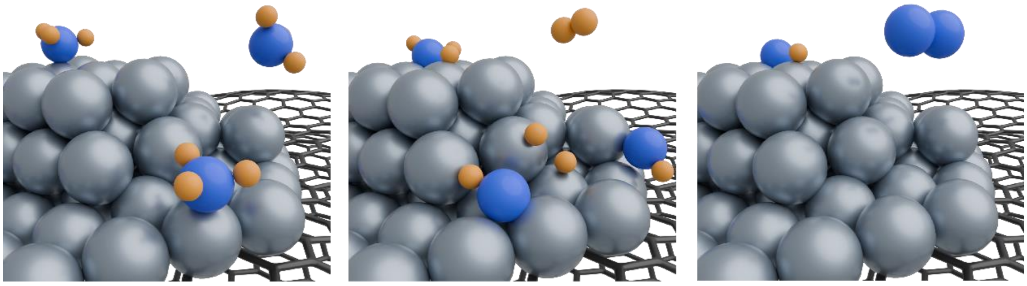

Figure 2.3. An illustration of the mechanism for ammonia decomposition in 3 steps; a) NH3 adsorption, b) N-H bond cleavage and H2 desorption, c) N2 desorption.

The rate-determining step has been heavily scrutinised. Early studies were characterised by the strong binding of N to catalyst surface, leading to suggestions that the nitrogen desorption step is rate-determining.[60,61] In 1978, Danielson and colleagues found that molecular nitrogen (N_2) does not appreciably absorb on Ru(0001), even at 100 K. This implies that the desorption of N_2 is rapid and therefore not kinetically significant (and not rate-determining).[62] This leaves only the recombination of nitrogen, which must therefore be rate-determining. In 1987, Tsai and Weinberg investigated the reaction over a Ru(001) surface at low pressure and showed that the surface of Ru was increasingly saturated with N at temperatures below 650 K. It was therefore concluded that at high temperatures (low N coverage), the reaction was limited by N-H cleavage, whereas at lower temperatures, the limit was the recombination of N_2.

This was furthered by Ganley *et al.* in 2004 and Hansgen *et al.* in 2010.[63,64] Ganley showed that the rate determining step was dependent on the specific catalyst metal, where N-H scission was shown to be rate determining for Rh, Ir, Pd, Pt, Cu, and N-N recombination was rate determining for Ni, Co, Fe. This information is laid out in a volcano curve in Figure 2.4.

Hansgen and colleagues developed this area, showing that the rate determining step is dependent on the nitrogen binding energy to the metal surface. They concluded that for surfaces whose nitrogen binding energy is less than 523 kJ mol^{-1}, the removal of the 2nd hydrogen was rate determining. This is different in surfaces with a higher binding energy, where the recombination of N_2 and the removal of 1st and 2nd hydrogen are all kinetically significant.[64]

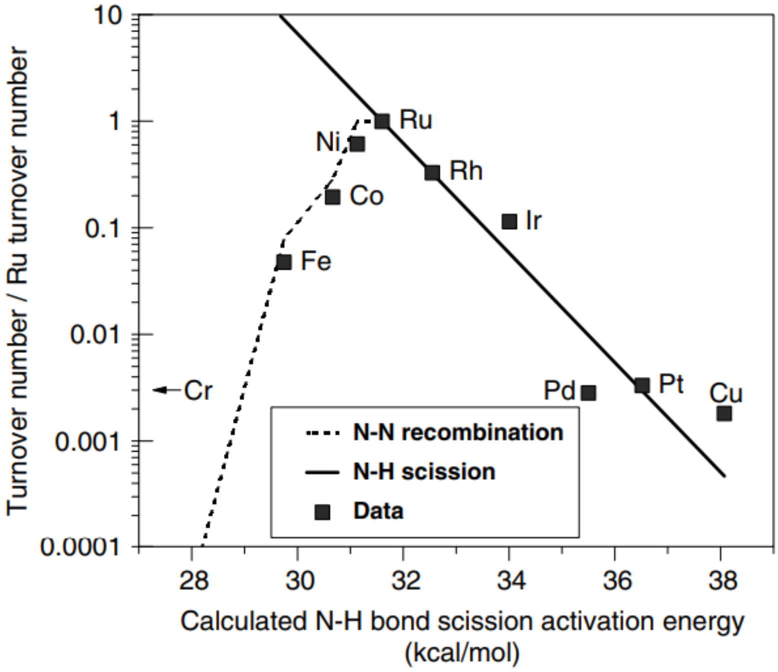

Figure 2.4. Correlation between the rate of ammonia decomposition on several metals and the relative rate of N-H bond scission, and N-N recombination (as estimated from the Blowers-Masel correlation). Reproduced from Ganley et al.[63]

2.4.2. Catalysts for Ammonia Decomposition

Modern catalysts for ammonia decomposition are, in most cases, similar to those used in ammonia synthesis - supported metal nanoparticles with promoters.[8,65] The main considerations when designing this type of catalyst are the active metal, the support material, and the promoters. For the active metal, the electrical and structural properties must be considered, with special focus to the interaction with the reaction species (NH_3, surface H, surface nitrides). For the support, important considerations include stability under reaction conditions, surface area, porosity, and electronic properties such as binding of the active metal and conductivity. In this thesis, promoters are not the focus but for information will be discussed in brief.

2.4.2.1. Active Metal

Research into active metals were some of the earliest standalone studies into ammonia decomposition that did not focus on their applicability to the synthesis reaction. In 1954, Amano and Taylor studied Ru, Rh, and Pd catalysts supported on alumina and reported the log(NH_3 decomposed) vs T. They found that Ru showed linear relationship from around 350 °C, Rh around 400 °C, and Pd around 500 °C, indicating that Ru was much more active at lower temperatures.[66] In 1997, Papapolymerou and Bontozoglou showed that iridium displays as much as an order of magnitude higher activity than Rh, which was in turn more active than Pd and Pt.[67] More recently in 2004, Yin *et al.* produced and tested a series of catalysts using different active metal (Ru, Rh, Pt, Pd, Ni, Fe), showing that, on a given support, the order of rates for H_2 formation were as follows: Ru >> Ir >Rh > Ni > Pt, Pd > Fe.

The work by Ganley *et al.* related the experimental activity of a metal for ammonia decomposition to the nitrogen-hydrogen bond scission energy (calculated using density functional theory). As seen in Figure 2.4, Ru, Ni, Co, Fe and Cr follow the predicted increase in decomposition rate with N_2 desorption rate. Also shown in Figure 2.4 is the trend expected when the scission of adsorbed N-H is rate-determining, showing excellent correlation to experimental values and confirming that the rate-determining step is different on different catalyst metals.

Ru is generally reported to be the most active metal for ammonia decomposition, which is reflected in its position at the top of the volcano curve in Figure 2.4.[8]

There are generally two branches of research of novel catalysts for hydrogen production from ammonia. These are defined by the active metal used to produce the catalyst: Ru (the most active), and any other metals. Ru, being the most active metal in this reaction can be considered apart from other catalysts, whereas other metal catalysts, such as those that use Co, Ni or Fe as an active phase, are typically researched due to lower material cost.

To produce catalysts that are the highest activity, Ru should be of particular interest as the active phase. The application of ammonia for hydrogen storage is dependent on the economisation of the processes of ammonia synthesis and ammonia cracking. To enable the prompt application of this technology, it is important to produce the highest activity catalysts possible – hence the use of Ru. Ru is an incredibly scarce material and as such, the optimisation of its use is of the utmost importance. The use of Ru in ammonia cracking catalysts is expected to be phased out in the longer term, once more active catalysts are made without it.

2.4.2.2. Support Materials and Promoters

Although the active metal is one of the main considerations in catalyst design, the support material can vastly affect the activity and selectivity (where applicable) of the resultant catalyst.

Support materials act as the foundational structure upon which the catalyst is built. These are typically high surface area materials upon which the active metal is deposited and must also be thermally and chemically stable if they are to be used under harsh conditions. In the case of ammonia cracking, these must be stable up to ~500°C under an ammonia atmosphere.

Support materials play two distinct roles (often simultaneously) – structural promotion and electronic promotion. Structurally, the support material anchors the metal in place, and the binding of the metal to the surface controls the distribution of the metal across the surface. In the case of wet-chemistry deposition, this is a direct effect: if the binding of the metal to the surface is more favourable than that of the metal salt to itself, then the nanoparticles produced will be smaller. In the case of direct atomic deposition such as magnetron sputtering, the binding of the metal to the support will affect the degree of agglomeration – resulting in size control of the nanoparticles.

Size control is of particular importance in Ru catalysts due to the strict geometry constraints of the active site – the B5 site. In 2009 Garcia-Garcia and colleagues studied the optimum size distribution of Ru particles on activated carbon supports.[68] In this study it was found that the optimum size for Ru nanoparticles lies in the 1.8 to 2.5 nm range. The reason for this being that in this range there is a much higher number of B5-sites on the surface of the Ru, as shown in Figure 2.5. Control of the size of the nanoparticles is therefore of paramount importance to ensure the highest concentration of active sites.

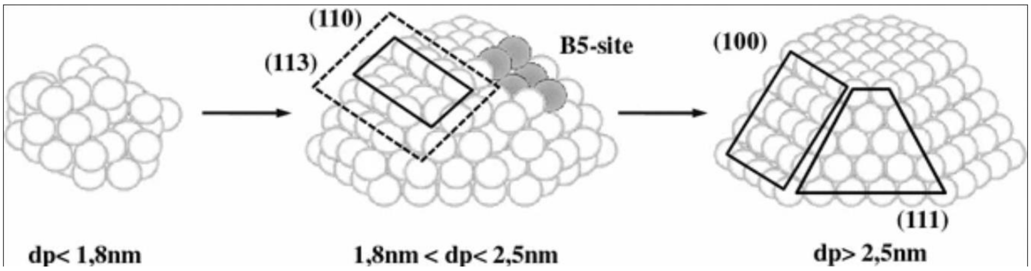

Figure 2.5. Three stages of the growth of Ru particle on C, reproduced from Garcia-Garcia et al. 2009.[68]

The support also often acts as an electronic promoter for the active metal. In the case of ammonia cracking, it has been shown that the basicity of the catalyst increases the activity of the resultant Ru based catalyst.[69] As such, the support can affect the activity of the catalyst by increasing basicity. In the case of conductive supports (such as graphitic materials), these can conduct electron density to the metal centre from other areas of the support or from additional basic promoters.

2.4.2.2.1 Ru Catalysts

A vast array of materials can be used successfully as support materials, but amongst the most prolific in Ru catalysts for ammonia cracking are carbon supports.[8] Carbon supports tend to be high in surface area and often lend a degree of electronic conductivity to allow the shuttling of electrons into the supported metal.

The most famous example of this in ammonia cracking is carbon nanotubes (CNTs). Carbon nanotubes are hollow, cylindrical nanotubes that are made from rolled-up sheets of graphene. They come in a wide variety of sizes and wall-thicknesses but are generally categorized as single-walled (SWCNTs) or multi-walled (MWCNTs). In their application to catalysis, they are very attractive due to a few factors – their large surface area-to-weight ratio, their excellent thermal and mechanical stability, and their unique delocalised electron structure. In this application, the multi-walled variety are often used.

In 2004, Yin *et al.* investigated the effects of the support material on activity by depositing metal on a number of supports (CNTs, activated carbon (AC), Al_2O_3, MgO, ZrO_2, TiO_2).[69] In terms of hydrogen production, the CNTs were found to be most active, followed by MgO and TiO_2. According to turnover frequency (TOF) and activation energy (E_a) data, the activity increases with increasing basicity of the support. Further, when neutral CNTs were modified with KOH to increase basicity, there was an increase in the conversion and TOF. They concluded that a highly basic support is necessary for high catalytic activity over Ru. In this case, they reported that the high electronic conductivity of CNTs facilitated a greater transfer of electron to the Ru centres, which improved the desorption of N_2 from the catalyst. Yin *et al.* followed this work in 2004 by investigating the production of a Ru/CNTs catalyst using a potassium promoter.[70] The K-

Ru/CNTs catalyst produced was long considered to be the most active catalyst for ammonia decomposition, until 2014.

In 2014, Hill and Torrente-Murciano reported a catalyst considered to be one of the most active catalysts in low temperature ammonia cracking: Ru/CNTs promoted with Cs (20 wt%).[71] In this work, they investigated the effects of a Cs promoter and found that the addition of Cs reduces the activation energy of the reaction. However, it was also found that the addition of too much Cs blocks active sites, reducing the rate of reaction.

Following on from this work in 2015, Hill and Torrente-Murciano reported that the conversion of this catalyst could be increased with lower Cs content if the CNTs had a higher degree of graphitisation.[72] The enhanced activity of the catalyst was attributed to the graphitised CNTs ability to facilitate electron transfer to the Ru centres.

As previously mentioned, an increase in the basicity of the support corresponds to an increase in the activity of the catalyst. This study by Hill and Torrente-Murciano illustrates that the mechanism for this is the electron donation from the support to the metal. In this case, the conductive support facilitates electron transfer from the Cs promoter thereby providing a high local electron density at the Ru sites, promoting N_2 recombination.

Doping of carbon supports with nitrogen has also been shown to improve the activity of carbon nanomaterials such as ordered mesoporous carbon,[73] CNTs[74-76] and CNFs.[77] There are a few mechanisms by which the doping increases activity in these materials. Firstly, doping carbon nanotubes with nitrogen leads to an increase in the dispersion of the Ru on the surface, giving a higher proportion of surface sites. It has also been shown that N-doping has a promoter-like effect on the catalyst, increasing the electron density of the support and thereby increasing the electron donation to the Ru nanoparticles.

The other notable carbon supports in Ru ammonia cracking catalysts are activated carbon and graphene. Activated carbon has been widely tested but is often reported to be the least active of all the carbon allotropes.[69,78] Considering the importance of graphitisation of the carbon support that was previously shown by Torrente-Murciano *et al.*, the inactivity of AC is likely due to its general lack of ordered structure, graphitisation or delocalised electron structure.

Ru on graphene was reported by Li *et al.* in 2017 to be highly active for ammonia decomposition.[79] These were produced by co-reduction of graphene oxide and Ru salt in a water-ethylene glycol mixture, giving a highly dispersed nanocomposite material. Li *et al.* attributed its high activity to the presence of oxygen containing groups on the surface of the graphene, which helped to anchor the high loading of Ru to the surface of the graphene. With an average particle size of 4 nm, the uniformity of the Ru distribution across this material is exceptionally good for wet-deposited samples, which although is not perfectly sized according to the B5-site theory, still contributed to its high activity.

Aside from carbon supports, a very widely studied group of support materials for this reaction are metal oxides, on which catalysts are typically active at higher reaction temperatures. One of the most widely used catalyst supports is Al_2O_3, which has long been used in catalysis. In ammonia decomposition, although it is often used as a benchmark catalyst, its activity is very low. As with most catalysts, this can be improved by promotion with alkali metals. Pyrz *et al.* found that the addition of K to Ru/Al_2O_3 catalyst resulted in the formation of a KRu_4O_8 hollandite that showed enhanced activity at temperatures 50-100 °C lower than the base Ru/Al_2O_3 catalyst.[80]

La_2O_3 has been used as a support to some success, as reported by Huang *et al.* in 2019.[81] In this work, it was shown that the activity of Ru/La_2O_3 is higher than that of Ru supported on Er_2O_3, SiO_2 and TiO_2 and also that the addition of KOH can increase the activity of the catalyst. The stability of this catalyst was shown to be excellent, which was attributed to the high degree of dispersion and the spatial isolation of the Ru nanoparticles.

MgO has been shown to be a highly effective support for Ru. In their preliminary study in 2004, Yin *et al.* found their Ru/MgO catalyst to be the most active in terms of TOF and E_a, beaten only by Ru/CNTs in terms of conversion.[69] In 2017, Ju *et al.* reported a highly active catalyst based on mesoporous MgO.[82] The activity of this catalyst was enhanced significantly by the mesoporous morphology, giving the catalyst a high surface area, high dispersion and enhanced metal-support interaction. When modified by KOH, the activity of this catalyst was comparable with K-Ru/CNTs under similar conditions.

Cerium Oxide (CeO_2) has been studied with some success as a tuneable support for Ru. The shape of CeO_2 nanoparticles is easy to control based on synthesis conditions allowing the synthesis of nanorods and nanospheres. A Ru catalyst supported on these materials (1 wt%) showed good conversions of 32% and 25% at 350 °C, compared to Ru on Al_2O_3 and MgO that showed 5% and 10% conversion under the same conditions.[83] This activity is attributed to the strong metal-support interaction and electronic modification of Ru by the CeO_2 support. As CeO_2 is a very basic material, relationship is in-line with expectation.[84]

Amongst some of the other ideas for support materials are waste materials such as red mud and fly ash. Red mud is composed of the oxides of Al, Si, Ca and Fe and is a by-product of the alumina production process; fly ash is generated from coal-fired power stations. These low-cost waste materials showed good activity at 550 C but were not directly competitive with the higher performing support materials mentioned above.

2.4.2.3. Other Metal Catalysts

Until recently, commercially available catalysts used in industrial ammonia cracker were primarily Ni supported on alumina. Ni has been explored extensively as an alternative to Ru in ammonia cracking catalysts. Amongst the earlier studies of supports for Ni ammonia cracking catalysts was Li *et al.* in 2006 who investigated Ru and Ni catalysts on 3 different SiO_2 supports: fumed SiO_2, MCM-41 and SBA-15.[85] Expectedly, Ru was shown to be the most active but Ni was shown in this work to be active down to 400 °C. It was also shown that the ammonia cracking over Ni catalysts is structure sensitive – with B5-like sites proposed as the active site, very similar to that of Ru catalysts. This structure sensitivity was also supported by Zhang *et al.*[86]

For promotion of Ni catalysts, lanthanide metals have been investigated as good potentials. In 2008, Ce was found to promote Ni/SBA-15 and Ni/Al_2O_3 at 450 C by Liu *et al.*[87] and Zheng *et al.* respectively.[88] Liu *et al.* further investigated La as a promoter but observed only weak promotion compared to Ce. Both investigations found the optimum ratio to be 0.3 Ce:Ni on a molar basis, and the Ce was found to be act as a structural promotor – increasing dispersion. Zheng *et al.* compared the stability of unmodified Ni/Al_2O_3 with the Ce promoted version and found that where the unmodified catalyst was unstable, the Ce promoted catalyst was stable for 80 hours.

Another lower-cost alternative to Ru is Co. Co lies only a little further from the peak of the volcano curve than Ni (Figure 2.4) and has been shown to provide good activity at low temperatures.[89] As supports for Co, carbon nanotubes have been shown to be particularly effective – as reported by Zhang *et al.* in 2013.[90] Amongst carbon supports, MWCNTs have been shown to be more effective than AC, reduced graphene oxide (RGO) and SWCNTs.[91]

Beyond carbon supports, metal oxides have been studied as supports for Co catalysts. In a study on mixed oxide systems, Podila *et al.* found that the order of activity for oxide supports tested was as follows: $La_2O_3 > CeO_2 > Al_2O_3$. Of all of the mixed metal oxide systems tested in this work, $Co/MgO\text{-}La_2O_3$ was found to be the most active due to its high basicity compared to other systems.[92]

In 2017, Torrente-Murciano *et al.* found that the use of a basic promoter such as Cs lowered the conversion compared to the unpromoted catalyst.[93] In this extensive work, Torrente-Murciano *et al.* also examined the effects of Co particle size and graphitisation of the carbon support, similar to the group's previous works on Ru. The findings of this work are summarised in Figure 2.6.

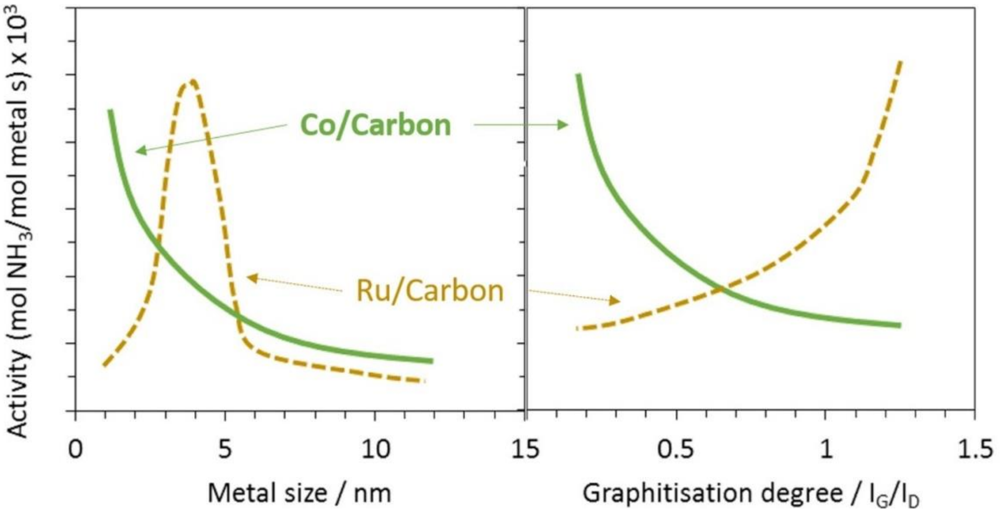

Figure 2.6. The effects of particle size and graphitisation of carbon support on the activity of Co/carbon (solid line) and Ru/carbon (dashed line) catalysts. Reproduced from Torrente-Murciano et al. 2017.[93]

In terms of particle size, Co shows the highest activity at low particle sizes (2 nm or less) whereas Ru shows the highest activity at a particle size around 3-5 nm, which supports observations reported by Garcia-Garcia.[68] In graphitisation, an even bigger difference is seen – Co shows a high activity with minimal graphitisation whereas Ru shows increased activity with increased graphitisation. Cobalt's displays inverse relationship of activity vs. graphitisation when compared to Ru. This indicates that the active site in Co catalysts is significantly different, and has a very different interaction with support materials.

2.5. Summary and Aims

The need to transition away from fossil fuels towards renewable energy sources is urgent and hydrogen is a promising alternative. However, the widespread adoption of a hydrogen economy is hindered by the challenges associated with sustainable production, storage and transportation on a large scale.

Ammonia, with its high hydrogen content and existing infrastructure for handling and transport has emerged as a great potential solution to these problems. Furthermore, of all of the zero-carbon fuels, ammonia contains the highest volumetric energy density (Figure 2.7), making it very well placed for future application. However, for ammonia to be broadly used, a key roadblock is the green, energy-efficient synthesis and cracking of ammonia.

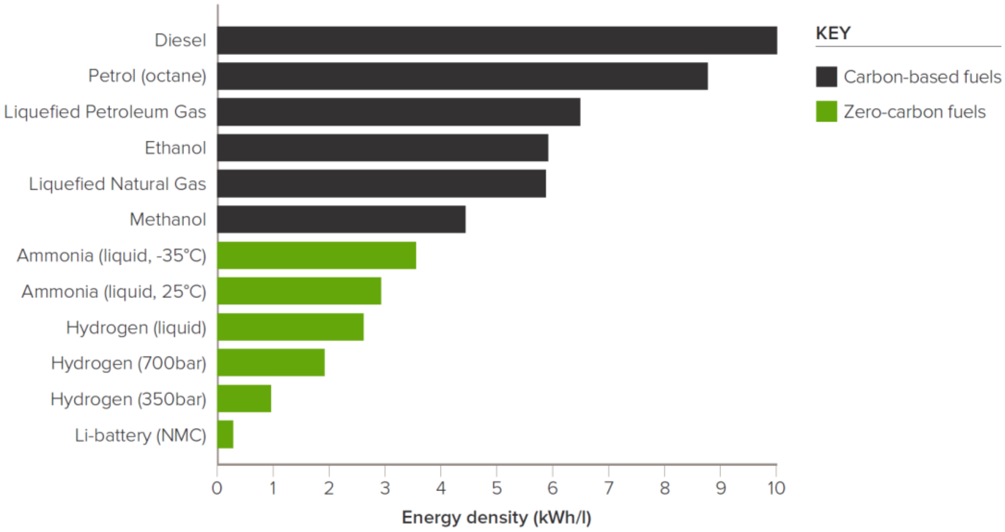

Figure 2.7. The volumetric energy density of a range of fuel options, reproduced from The Royal Society Briefing.[94]

This thesis focuses on the development of novel heterogeneous catalysts for ammonia cracking at low temperatures. I will focus on Ru as the active metal to maximise the activity of the catalyst, specifically paired with a unique support material, graphitised nanofibers (GNF). The vision is to contribute to the advancement of low-temperature ammonia cracking catalysts to enable their application in an ammonia economy.

In this thesis, I aim to:

1. Produce a Ru/GNF catalyst and characterise it.

2. Test the catalyst for ammonia decomposition and study the effect of the pre-treatment stage on the behaviour of the catalyst.
3. Use identical location AC-STEM microscopy to image the nanoparticles before and after various stages of the reaction to understand the morphological changes in the catalyst.
4. Study the catalyst by a variety of transient characterisation techniques to understand the evolution of the catalyst.

In doing this, I hope to produce a novel catalyst that is highly active towards ammonia decomposition. I also hope to contribute to the further development of this field of catalysis using novel characterisation techniques to study the evolution of catalysts over the course of a reaction.

3. Experimental

In this chapter, the experimental procedures are described, detailing the metal deposition procedure by magnetron sputtering and the main characterisation techniques used.

3.1. Magnetron Sputtering

All depositions were conducted using an AJA magnetron sputtering system. In general, the supports were placed in the glove box (N_2) and heated under vacuum for 5 hours (100 °C) to remove any moisture. The samples were stored under N_2 until they were needed for deposition, which was anywhere from 1 day – 3 months.

For the deposition, the dried supports were transferred to a custom-built stirring sample holder, on top of a quartz disc insert. The sample holder was transferred to the load-lock chamber which was then evacuated under vacuum for ~1-2 hours (or until ~10^{-7} Torr). It was then passed into the main chamber, placed onto the stirring stage and evacuated further under vacuum (until ~10^{-8} Torr). The Ru depositions were conducted at room temperature with a working pressure of 3 mTorr of Ar. Ar plasma was applied to a Ru target (Kurt J Lesker, 99.99%) with a set current for a set time, differing for each support material. The resulting material passed back to the load-lock and then into the glovebox. It was checked for homogeneity and sieved, before being placed into a vial and passed out of the glovebox. The catalysts were used without any further purification or treatment (aside from pre-treatments discussed in each chapter).

3.2. Measurement of Metal Loading

To determine loading, inductively coupled plasma-optical emission spectroscopy (ICP-OES) measurements were performed in triplicate on a PerkinElmer Optima 2000 spectrometer. The Ru/GNF catalyst (~10 mg) underwent microwave-assisted digestion at 150 °C using aqua regia (2 mL) and was then diluted to 10 mL with a 5% HCl solution. This solution was flushed through the spectrometer for 1.5 minutes before measurements were taken. The measurements at each wavelength are an average of 3 optical measurements, calibrated against known concentrations of Ru, prepared from an ICP standard (Sigma-Aldrich, 1000 mg/L) and milli-Q filtered deionised water.

3.3. Catalytic Studies

Catalytic decomposition of NH_3 was conducted in a packed bed reactor in which the reaction temperature was monitored by a thermocouple in the catalyst bed (Hiden CATLAB Microreactor). Typically, 2.5 mg of catalyst was loaded into a quartz tube (4 mm i.d.), packed with quartz wool to secure the catalyst in place. Prior to testing (unless otherwise stated) the catalyst was reduced in situ at 450°C (1°C/min ramp) for 1 hr under a 25 mL min-1 flow of 5% H_2 in Ar and 5 mL min^{-1} of He. The gas flow was switched to 25 mL min^{-1} of 5% NH_3 in Ar and 5 mL min^{-1} of He, and the temperature was ramped (1 °C/min) to the desired reaction temperature. This gives a constant WHSV of the progress of the reaction was monitored by an in-line mass spectrometer (Hiden QGA), taking a reading every ~20 s. The measured masses were 17 (NH_3), 16 (NH_2), 28 (N_2) and 2 (H_2). The output of the mass spectrometer was calibrated against known partial pressures of gas (both NH_3 and H_2). In the final rates, H_2 was used to calculate rate as it was noted to give more stable and accurate readings. The rate calculations were calculated using:

$$Rate \ = \frac{P_{H_2}\,(outlet)}{1.5 \times P_{NH_3}(inlet)} \times theoretical\ yield\ (mmol\ \min^{-1} g_{Ru}^{-1})$$

Where P_{H_2} $(outlet)$ is the partial pressure of hydrogen as is measured by the mass spectrometer and P_{NH_3} $(inlet)$ is the partial pressure of ammonia calculated from the input gas flow. The bare supports were also confirmed to be inactive for ammonia decomposition at 450 °C. For activation energy calculations, the reactor was cooled to ambient before being ramped to 450 °C once again (1 °C/min).

In general, activation energy calculations were made using the Arrhenius equation from the downwards ramp data after set periods of time on stream. These calculations use the following relationships.

$$Rate = k\ [A]^a[B]^b$$

Where *[A]* and *[B]* are the concentrations of specias A and B, and a and b their orders in the reaction. The rate constant, k, is given by the equation:

$$k = Ae^{\frac{-E_a}{RT}}$$

Where A is the pre-exponential factor, E_a is activation energy, R is the gas constant, and T is temperature.

It then follows that

$$rate \propto\ Ae^{\frac{-E_a}{RT}}$$

And therefore

$$\ln(rate) \propto\ \ln(A) - \frac{E_a}{RT}$$

The natural log of the rate for the downwards ramp of the activity measurements was plotted against 1/T (K^{-1}), and a linear fit was made of the resultant graph to give $-E_a/R$ as the gradient.

3.4. AC-STEM Imaging

Nanocluster size and atomic structure were characterized at the University of Birmingham by a JEOL JEM2100F aberration-corrected scanning transmission electron microscope (AC-STEM) equipped with a Cs probe corrector (CEOS) at a convergence angle of 19 mrad and annular dark field detector (ADF) operating with an inner angle of 31 mrad and outer angle of 82 mrad at 200 kV. The bright field (BF) detector was also used in parallel. Typically, samples were prepared via a drop casting technique, where samples were first dispersed in absolute ethanol (HPLC grade, 99.5%) using ultrasonication. The suspension was then deposited onto "lacey carbon film" Cu TEM grids (Agar Scientific). For identical location microscopy, grids were produced using the same technique, but instead using "lacey carbon film" Au H7 Finder grids (Agar Scientific) to produce an IL-grid (Identical Location grid). The IL-grids were imaged as prepared, before being placed into the reactor tube and being subjected to reaction conditions for 12 and 70 hours respectively. These grids were then imaged in identical location post reaction.

3.5. X-Ray Characterisation

X-ray photoelectron spectroscopy (XPS) was performed using a Kratos AXIS SUPRA PLUS instrument with a monochromatic Al Kα X-ray source ($h\nu = 1486.6$ eV) operated at room temperature with 10 mA emission current and 12 kV anode potential. The electron collection spot size was ca. 700 × 300 mm^2. A pass energy of 160 eV was used for the survey scans and 20 eV for the high-resolution scans. Spectra were converted into VAMAS format for further analysis. The data was processed using CasaXPS software. Charge correction in reference to C 1s in carbon materials, and metal oxide O 1s in metal oxide materials.

XPS was also performed at one of the permanently mounted ultra-high vacuum endstations on the I09 beam line[95] at Diamond Light Source. The I09 beamline consists of two light sources that cover soft (0.11 – 1.8 keV) and hard (2.1 – 15 keV) X-ray ranges. Each source has its own dedicated undulator and monochromator (soft: plane grating monochromator; hard: double crystal monochromator) and converge at the same point on the sample in the utilised endstation. Soft (SXPS) and hard (HAXPES) X-ray photoelectron spectroscopy were acquired using a Scienta EW4000 HAXPES hemispherical energy analyser. The analyser was mounted perpendicular to the incident photons, in the plane of the photon polarisation (linear horizontal). A photon energy of 480 eV was used for Ru 3d SXPS and 2500 eV for HAXPES.

In-situ EXAFS was performed on the Ru K-edge in transmission mode at the B18 beamline at the Diamond Light Source in Oxford, UK.[96] A capillary furnace setup provided by the beamline was used. The Ru/GNF powder was pressed to a pellet, which was inserted into a quartz capillary, connected to the beamline mass flow controllers using Swagelok tubing. Transmission spectra covering both the extended X-ray absorption fine structure (EXAFS) region (200 eV below the edge to 850 eV above the edge) were collected in continuous scan mode with an acquisition time of approximately 90 seconds per spectrum. The X-ray energy was selected using a double crystal Si(111) monochromator, and spectra of a Ru metal foil were measured simultaneously for energy calibration. Unless otherwise stated, the ramp rate was set to 5 °C min^{-1}, and the temperature was held for 30 minutes before sample measurement. EXAFS were taken of the sample in air at 14°C (RT), before 4% H_2 in Ar was flowed through the tube (25 mL min^{-1}). The sample was heated in 3 stages - 150 °C, 300 °C and 450 °C and measured at each stage. At this stage, the gas flow was switched to 5% NH_3 in Ar (25 mL min^{-1}), which was flowed for 30 minutes before measurement. The temperature was increased in stages to 500 °C and 550°C and measured at each stage.

Data treatment was carried out in Athena from the Demeter software package.[97] The EXAFS ($\chi(k)$) was obtained with a spline range of k = 0.5–13 Å^{-1} and a k2 weighting. The EXAFS Fourier transforms ($\chi(R)$) were obtained by using data in the k-range of 1.5–12 Å^{-1}, a k2 weighting, and a Hanning window.

4. Material – Ru/GNF

The following chapter focuses on the production of the key material used in this thesis. Firstly, I will outline the relevant background for the application of carbon supports in ammonia cracking catalysts. Then, the production of the catalysts used in this work will be outlined and the characterisation of the material will be discussed. Finally, there will be a discussion of the ammonia cracking reaction and an investigation of the effects of catalyst pre-treatment on the activity of the catalyst.

4.1. Ruthenium on Carbon Supports

Carbon materials are well known for their use in ammonia cracking, being widely used at support materials. Of all reported supports for ammonia decomposition, CNTs are often reported as the most optimal. In 2004, Yin *et al.* analysed the activity of Ru deposited on a number of supports. They found that Ru on CNTs were the most active compared to common metal oxide catalyst supports: CNTs > MgO > TiO_2 > Al_2O_3 > ZrO_2 > Activated Carbon (AC). [69]

A few years later in 2007, Li *et al.* conducted a similar study, this time focused on carbon supports and reported the following trend: Graphitic carbon (GC) > CNTs > Carbon Black (CB) > Mesoporous carbon (CMK-3) > AC.[78] In this study, limited conclusions can be drawn about the pure effect of the support in the case of CNTs and GC due to the vast differences in dispersion of the Ru on the supports. The Ru/CNTs catalyst had a dispersion of 85.6 % and an average particle size of 1.6 nm, significantly less that the reported optimum by Garcia-Garcia *et al.*[68] In contrast, the graphitic carbon sample had a dispersion of 41.8% and an average particle size of 3.2 nm – exactly in the reported optimum. The Ru/CNTs sample gave a conversion of 84.7% and the Ru/GC sample 95.0%. Despite the concerns, the study by Li *et al.* does reinforce the high activity of CNT supported catalysts and also hints at the effect of graphitisation of the carbon support on the activity of the catalyst.

In 2004, Wang *et al.* reported a highly active catalyst produced by the deposition of Ru on the surface of CNTs, and then subsequently depositing KNO_3 into the catalyst.[98] This remained the most active catalyst for ammonia decomposition until 2014, when Hill and Torrente-Murciano reported a Cs promoted Ru/CNTs catalyst for low-temperature ammonia cracking.[71] In 2015, Hill and Torrente-Murciano followed up by investigating the effects of surface graphitisation of the CNT support and found that at lower Cs loadings, an increase in graphitisation of the support increased the activity dramatically.[72] They concluded that graphitisation of the support allows "distance promotion"; whereby the graphitic carbon aids in shuttling electron density from the Cs promoter sites to the Ru active sites. This allows promotion without blocking the active sites of the Ru nanoparticles.

Based on the results of both Hill and Torrente-Murciano in 2015, and Li *et al.* in 2007, I hypothesize that a highly graphitised nanofiber material could support a highly active catalyst for ammonia decomposition. In this way, graphitised nanofibers (GNF) could act as a hybrid between CNTs and graphitic carbon, both of which have shown high activity as support for Ru ammonia cracking catalysts.

Unlike other famous carbon materials (such as CNTs), carbon nanofibers (CNFs) have not been extensively tested as supports for Ru but the few tests seen in the literature have not been overly promising. There is a glimmer of hope however - CNFs tested in the literature are often produced in-house and tend to have a low degree of graphitisation, which could have a detrimental effect on the overall rate. High purity nanofibers with a high degree of graphitisation could combine the high surface area and favourable shape of CNTs with the electronic mobility offered by graphitised carbon.

PR-24 graphitised carbon nanofibers (GNFs) (Pyrograf®-III, Applied Science, USA) are made from conical platelet of graphite stacked into long, hollow fibres.[99] These GNFs are ultra-high purity, with less than 100 ppm of iron remaining (the catalyst used to grow the fibres). PR-24 GNFs have been applied towards many catalytic applications with much success.[100,101] Much of the success of their previous application has been attributed to the "step-edges" that form where the platelets of graphite stack together. These provide an excellent anchor point for the stabilisation of nanoparticles, an example of which is displayed in Figure 4.1. Due to the high degree of graphitisation of GNF, it is also a highly conductive material, which could allow a greater degree of electron donation to supported metal. Finally, the high surface area of this material, due to its unique nanostructure, lends itself towards catalytic application.

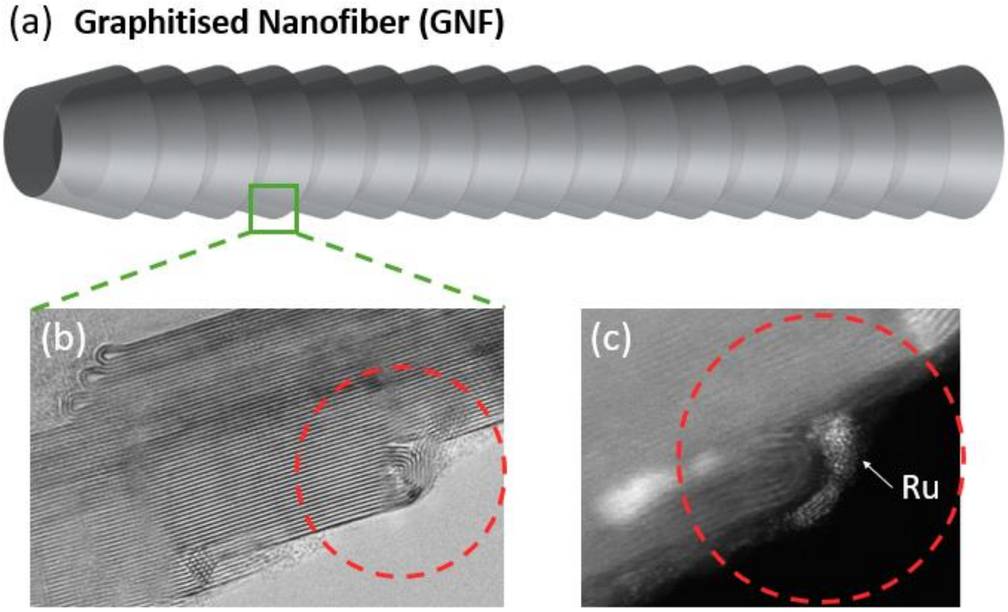

Figure 4.1. A diagram of the structure of PR-24 GNF (a), with inset bright AC-STEM images of a step edge of pristine GNF (b) and dark-field image of Ru deposited on GNF (c).

An example of the interaction of the step-edges of the GNF with a catalyst metal is seen in Figure 4.1, where a nanoparticle of Ru is seen hugging the step-edge. This behaviour is very often seen in the application of GNF as a catalyst support which is often attributed to the disruption of the π-system where the graphitic sheets curve over. These produce local concentrations of electron density at the step edges that stabilise the nanoparticles to a greater degree than the flat graphitic surface.

4.2. Aims and Objectives

This chapter's aim to describe the production, characterization, and initial catalytic testing of Ru/GNF. It also aims to understand the interaction between the Ru and the support, which will be done using AC-STEM. The final aim of this chapter is to describe the initial testing of Ru/GNF and study the effect of different pre-treatment methodologies on the catalytic activity of the material, providing an outline for the future investigation of catalyst pre-treatments.

To achieve these aims, the chapter will:

1. Outline the synthesis of Ru/GNF using magnetron sputtering
2. Present the characterisation of the material using ICP-OES and AC-STEM.
3. Evaluate the catalytic activity of the catalyst.
4. Investigate the impact of pre-treatments on the catalyst's behaviour.

4.3. Production of Ru/GNF

A Ru/GNF catalyst was prepared by magnetron sputtering deposition of Ru atoms onto PR-24 GNFs, whilst being agitated by mechanical stirring (Figure 4.2). Prior to the deposition, the sample was heated under vacuum inside a glovebox for 3 hours to remove any adsorbed water on the surface (130 °C). Once the flask had cooled, the sample was stored in a glovebox until deposition. In the deposition, 500 mg of sample was placed onto a quartz disc in the powder sample holder, and the stirrer was placed on top. The sample was degassed at high vacuum (10^{-6} Torr) before being passed into the main chamber where it was further degassed (10^{-8} Torr). The deposition was then conducted with a working pressure of 3 mTorr Ar gas. The working current was 300 mA, and the deposition was carried out for 30 minutes. A schematic diagram for this process is seen in Figure 4.2.

The catalyst loading was measured by ICP-OES using a Perkin Elmer Optima 2000. The measurements were taken in triplicate at 2 wavelengths (240 nm and 267 nm) and the final loadings were averaged. The sample was confirmed to be 0.75 wt% Ru.

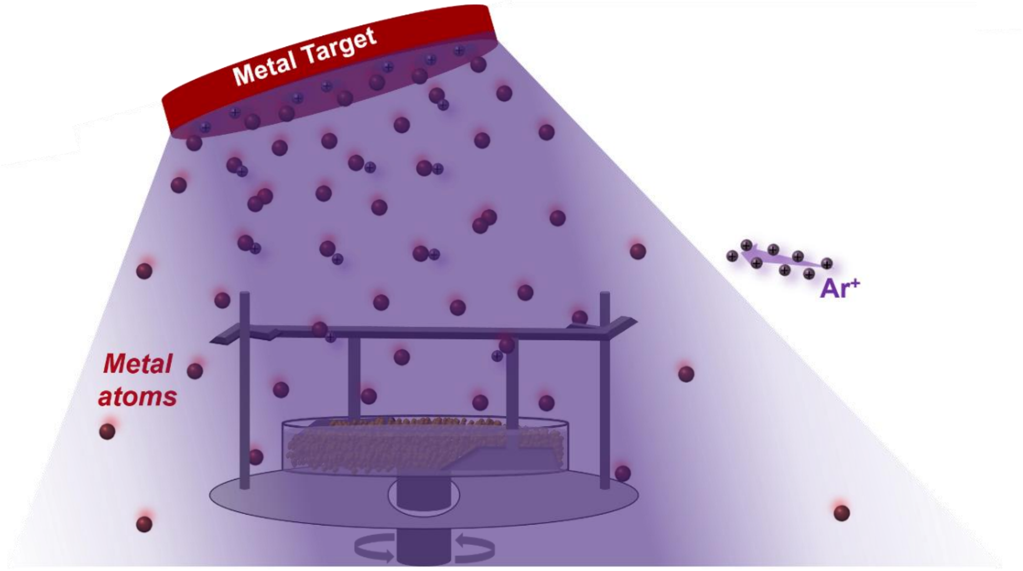

Figure 4.2. A schematic of the magnetron sputtering process. Ar ions bombard the metal target, ejecting Ru atoms in a cone that land on the sample stage. Mechanical stirring is employed to agitate the powder and ensure homogeneous distribution.

After deposition, the sample was imaged by AC-STEM to understand the morphology of the Ru nanoparticles. AC-STEM of Ru/GNF showed 2 distinct regions in the catalyst.

In the first region, the Ru predominantly exists as single atoms or very small clusters (Figure 4.3). This is due to the low loading of Ru in these areas and could also be related to the concentration of defects in these areas. Both low concentrations of metal and higher concentrations of point defects have been shown to increase the dispersion of metal atoms on carbon surfaces.[102]

It should be noted that single atoms and very small clusters are not expected to be active in ammonia decomposition, but brief analysis of these regions will be included for completeness.

Low loading regions are likely present due to the shadowing effect during magnetron sputtering deposition. GNFs that clump together are not directly exposed to the shower of Ru atoms and, therefore, have a significantly lower loading than the exposed surfaces.

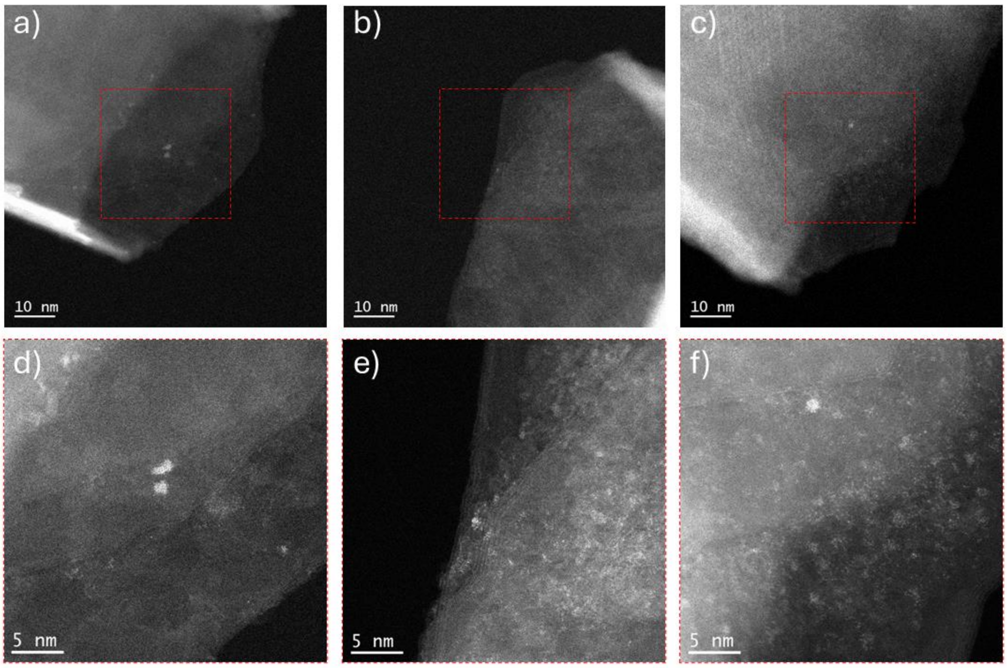

Figure 4.3. Region 1 of Ru/GNF, highlighting the presence of single-atoms and small clusters on the lesser loaded GNFs where a), b), and c) are 2 Mx magnification and d), e) and f) are the respective 5 Mx magnification images.

In the 2nd region, there is a much higher concentration of Ru which gives rise to a high coverage on the GNF surface. In these regions, the Ru forms clusters around 1-2 nm in diameter, which tend to localise in the step edges of the GNF, forming long worm-like structures (Figure 4.4. a-c). From the high magnification images, it is seen that the worms are microcrystalline chains of Ru clusters that are loosely bound to one another (Figure 4.4. d-f). These groupings form due to the low barrier for migration of Ru across carbon and low surface roughness of the graphitic support. This allows small clusters of Ru to move across the support until it encounters a feature that anchors it (such as a step edge or point defect) or another cluster, whereby it stops its migration. In GNF regions with fewer step-edges (as in Figure 4.4. c and f), the Ru clusters form less defined structures but still retain the characteristic microcrystalline grouping. The effect of this during catalysis will be further explored in the identical location AC-STEM section.

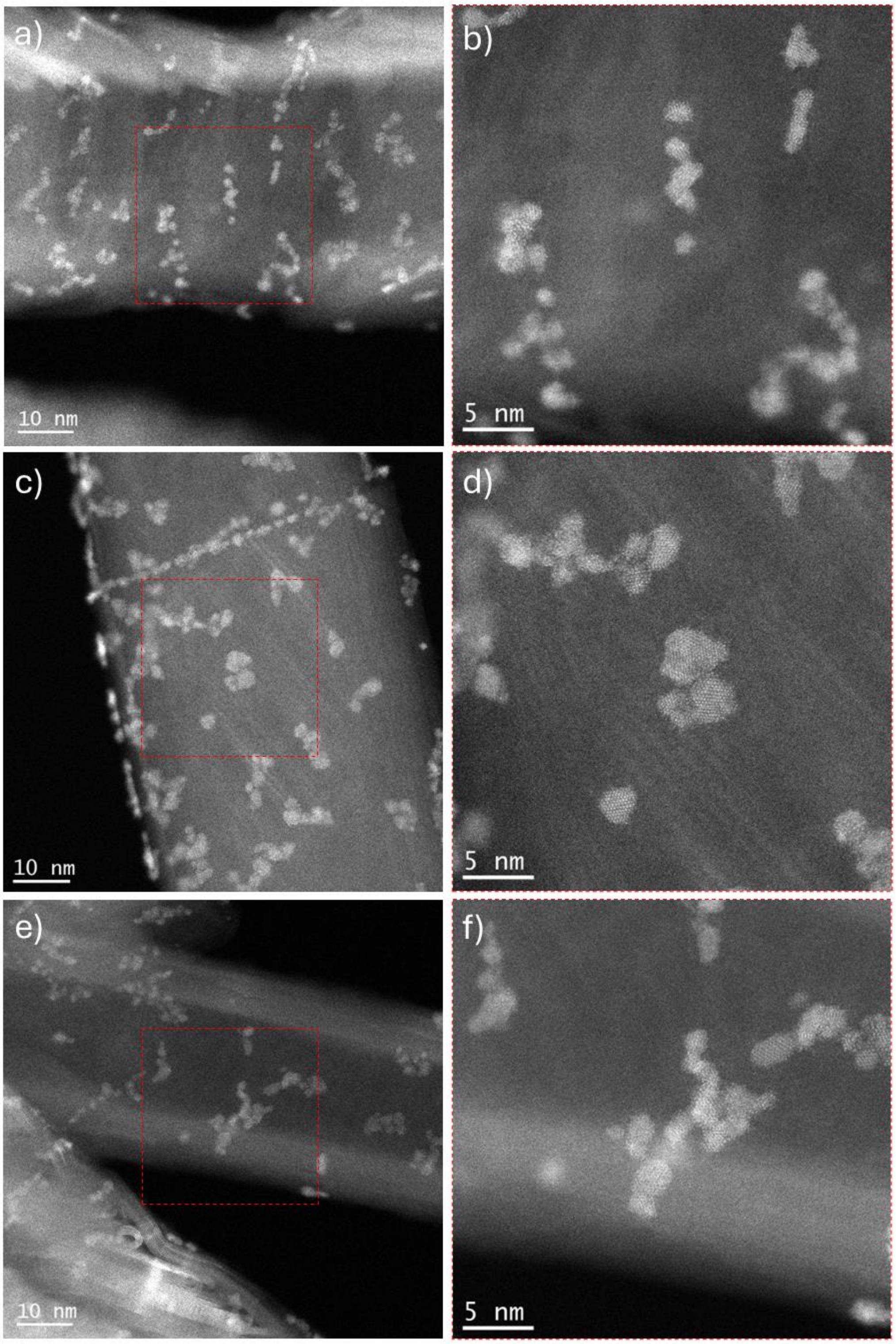

Figure 4.4. Region 2 of Ru/GNF, showing the increased concentration of Ru on the surface resulting in worm-like microcrystalline nanoparticles consisting of an agglomeration of 1-2 nm flat nanoparticles. (A), (c), and (e) are 2 Mx magnification and b), d) and f) are the respective 5 Mx magnification images.

In most cases for region 2, the nanoclusters assemble into flattened islands and form into worm-like shapes around the step edges of the GNF. Flat clusters that are next to each other have distinct boundaries and are largely amorphous. In the case of larger groupings, it is seen that crystal orientation may be shared across crystallites (as in Figure 4.4. d). Due to the shape of these particles, it is difficult to determine a size distribution, so analysis of the size distribution will be omitted for the sample as prepared.

Small islands of Ru (around 1 nm in diameter) form as Ru atoms meet other Ru atoms. These islands migrate across the Ru surface until they find some feature of the support that allows the stabilisation of the Ru. This could be a step edge (as discussed earlier), a vacancy defect, or an existing island of Ru. The result of this process is seen in AC-STEM as amorphous worm-like clusters, groups around step edges of the GNF. This effect is illustrated in Figure 4.5.

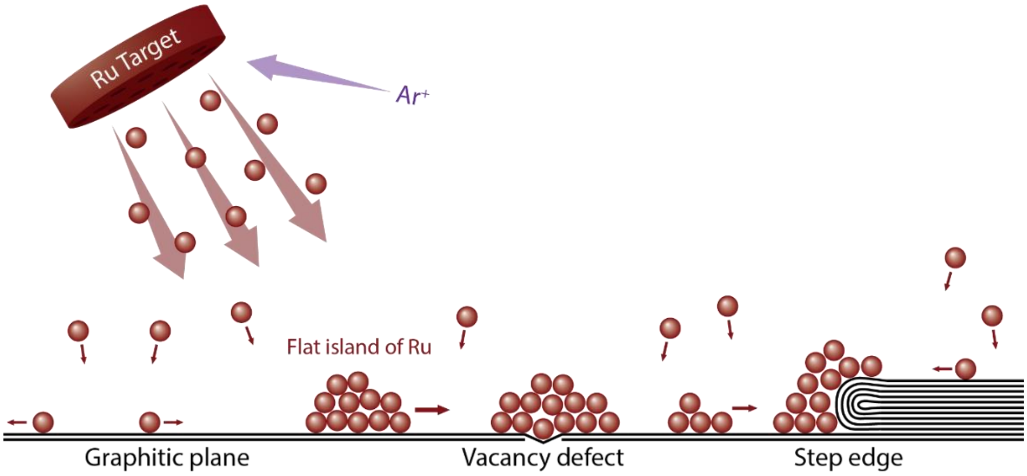

Figure 4.5. A schematic diagram of the magnetron sputtering process onto a surface of GNF. Atoms landing of the graphitic plane form flat islands of Ru that migrate until they find a stabilisation site such as a vacancy defect. Further islands migrate and stick side-on to form amorphous worms of Ru.

4.4. Catalyst Testing

The catalyst was tested for ammonia decomposition activity in a Hiden CATLAB Microreactor with an inline QGA mass spectrometer (please see experimental section for full details). The results of this experiment can be seen in Figure 4.6.

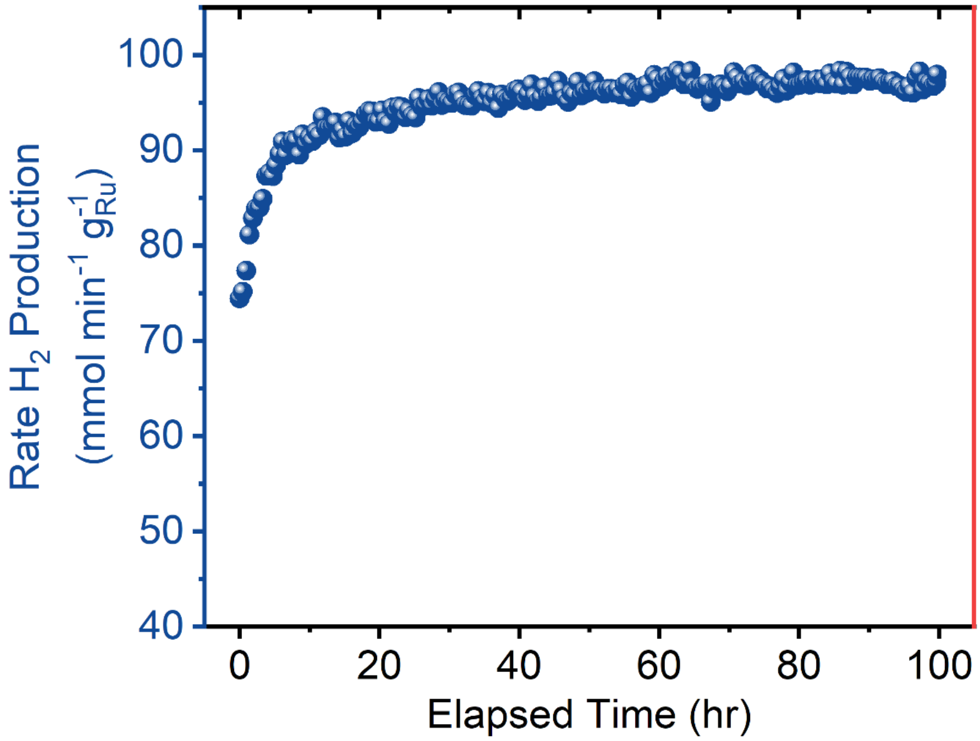

Figure 4.6. The rate of hydrogen production from ammonia for Ru/GNF over 100 hours of reaction.

The Ru/GNF catalyst displayed a high activity for ammonia decomposition and further, showed self-improvement behaviour – increasing in rate of H_2 production over the first 50 hours of reaction from 75 to 95 mmol min^{-1} g_{Ru}^{-1}. This behaviour is rarely observed (only once to my knowledge)[103] and the implications of it are significant. If a catalyst can be produced that not only maintained high activity but increases in activity over time, then it's possible that this could be applied more broadly, producing very highly active and stable catalysts. As a first port-of-call to help understand the mechanism of the self-improvement of the catalyst, several pre-treatment protocols were tested prior to the catalytic activity measurement. The aim of these tests was to understand the effect of the first few hours under reaction temperature with exposure to different gases, and to see the effect of heating and cooling the catalyst prior to the reaction.

4.5. Pre-treatment Protocols for Ammonia Decomposition Catalysts

4.5.1. Background

The pre-treatment of heterogeneous catalysts has a huge effect on their activity and selectivity. Supported metal catalysts like Ru/GNF are inherently very difficult to control finely due to the sheer degree of variation in bulk materials. The number of variables present in the final catalyst is huge. Firstly, the support material has a ligand-like effect on the metal centres and changes to the morphology or electronic structure of the support material (affected by synthesis and treatment of the support) will have a huge knock-on effect. The deposition of the metal can introduce large variation in the catalyst based on the deposition method, the rate of deposition, and uniformity that can result in huge variation in catalytic activity. Finally, the pre-treatment of the catalyst prior to the reaction can change the oxidation state of the metal, the binding of the metal nanoparticles to the support material and can even change the support itself. Each of these has a large effect on the activity and stability of the catalyst. Both the variation of the support material (including different morphologies or doping to change the electronics) and new methods for deposition have been widely studied in the ammonia cracking reaction and others to great effect.

In the literature, pre-treatment protocols are ubiquitously reported, but much detail is often left out for the sake of conciseness, often being reduced to a short few sentences in the experimental section. Here, I outline in detail the effect of pre-treatment to the catalysts. I hope to contribute to the advancement of the field by reporting different pre-treatment methods onto the catalytic activity.

In this chapter, I will categorise several reported pre-treatment procedures for ammonia decomposition from literature. I will then apply these pre-treatment procedures to the Ru/GNF catalyst discussed earlier in this chapter and compare the resultant activities and stabilities of the catalysts over short time periods. These results will display the degree to which the catalytic activity can be tuned by the pre-treatment procedure used.

This work is very elementary in its nature but is even more important because of it. It is impossible to compare catalysts to one another that have not undergone the same degree of conditions testing. At the end of this chapter, I will suggest a short list of pre-treatment experiments that could be used with any ammonia decomposition catalyst as a jumping off point for the optimisation of pre-treatment conditions.

4.5.2. Pre-treatments in Literature

By far the most common pre-treatment procedure in literature is calcination of catalysts following metal deposition. Catalysts produced by wet chemistry methods such as incipient wetness impregnation are calcined ex-situ for an extended period (6 hours or more) to decompose the impregnated metal salts, leaving metal nanoparticles.

Metal nanoparticles oxidise easily under air, so catalysts are often reduced in-situ, producing metallic nanoparticles that are more active towards catalysis. Most pre-treatment procedures for ammonia decomposition catalysts use in-situ reduction under a flow of hydrogen but some also include some ammonia treatment.

Figure 4.7 and *Figure 4.8* show a set of 16 reaction profiles including pre-treatment taken from prominent papers in the ammonia decomposition literature.[69,70,75,77,79,82,98,103-111]

These pre-treatments were organised alongside similar pre-treatment methodologies, which are labelled as “H_2 reduction”, “Cool post reduction”, “Flush post reduction”, “NH_3 reduction”, “NH_3 activation”.

Based on the archetypes that were identified, experiments were designed to test the effect of these pre-treatment conditions which will be outlined below.

A further 2 experiments were designed to account for the effects of heat treating the catalyst, similar to calcination. These are labelled “Ex-situ heat treat 48 hr” and “in-situ heat treat 6 hr”.

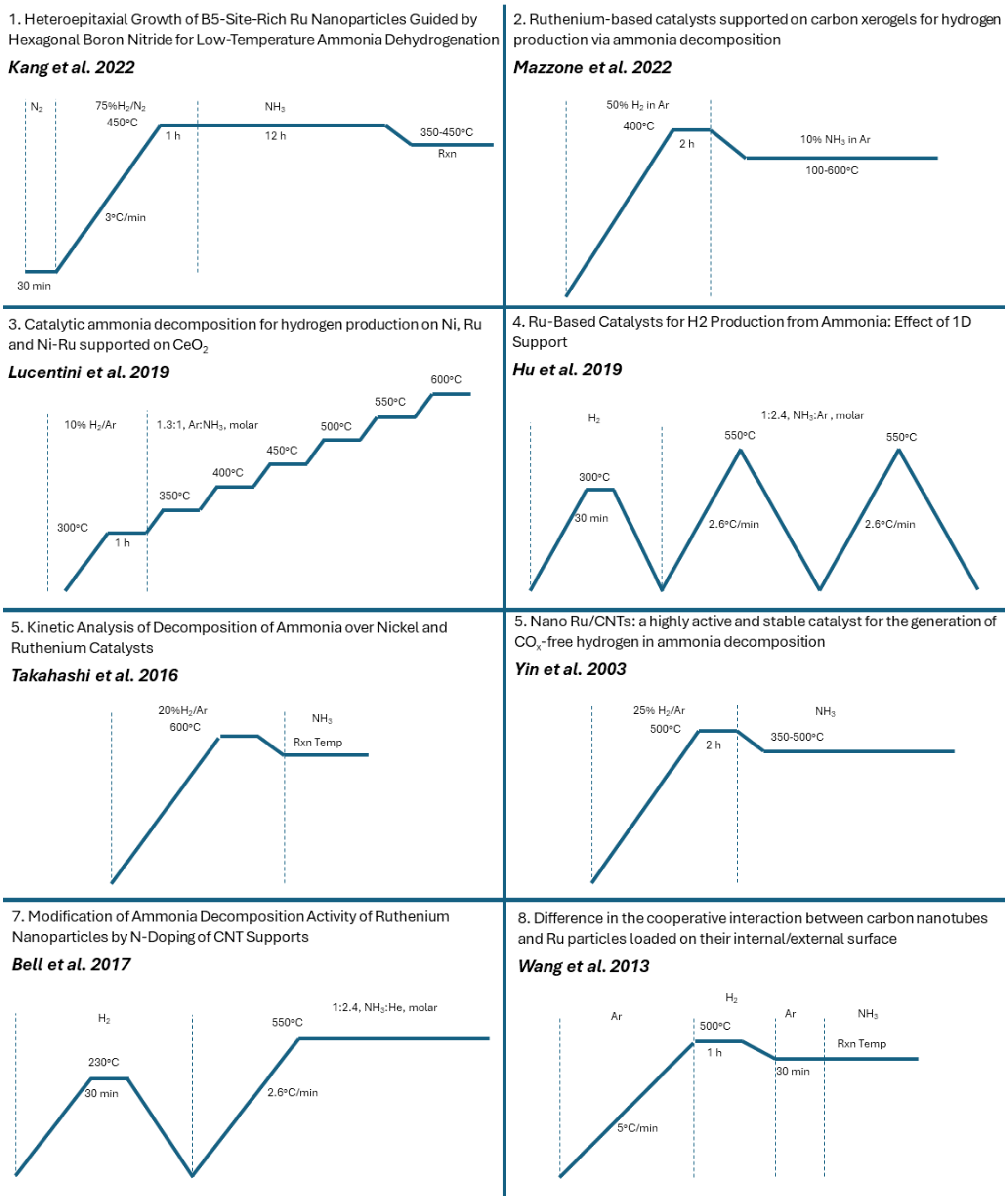
1. Heteroepitaxial Growth of B5-Site-Rich Ru Nanoparticles Guided by Hexagonal Boron Nitride for Low-Temperature Ammonia Dehydrogenation

Kang et al. 2022

2. Ruthenium-based catalysts supported on carbon xerogels for hydrogen production via ammonia decomposition

Mazzone et al. 2022

3. Catalytic ammonia decomposition for hydrogen production on Ni, Ru and Ni-Ru supported on CeO_2

Lucentini et al. 2019

4. Ru-Based Catalysts for H2 Production from Ammonia: Effect of 1D Support

Hu et al. 2019

5. Kinetic Analysis of Decomposition of Ammonia over Nickel and Ruthenium Catalysts

Takahashi et al. 2016

5. Nano Ru/CNTs: a highly active and stable catalyst for the generation of CO_x-free hydrogen in ammonia decomposition

Yin et al. 2003

7. Modification of Ammonia Decomposition Activity of Ruthenium Nanoparticles by N-Doping of CNT Supports

Bell et al. 2017

8. Difference in the cooperative interaction between carbon nanotubes and Ru particles loaded on their internal/external surface

Wang et al. 2013

Figure 4.7. Schematic diagrams displaying the pre-treatment methodologies from 8 papers on ammonia decomposition.[70,103-109]

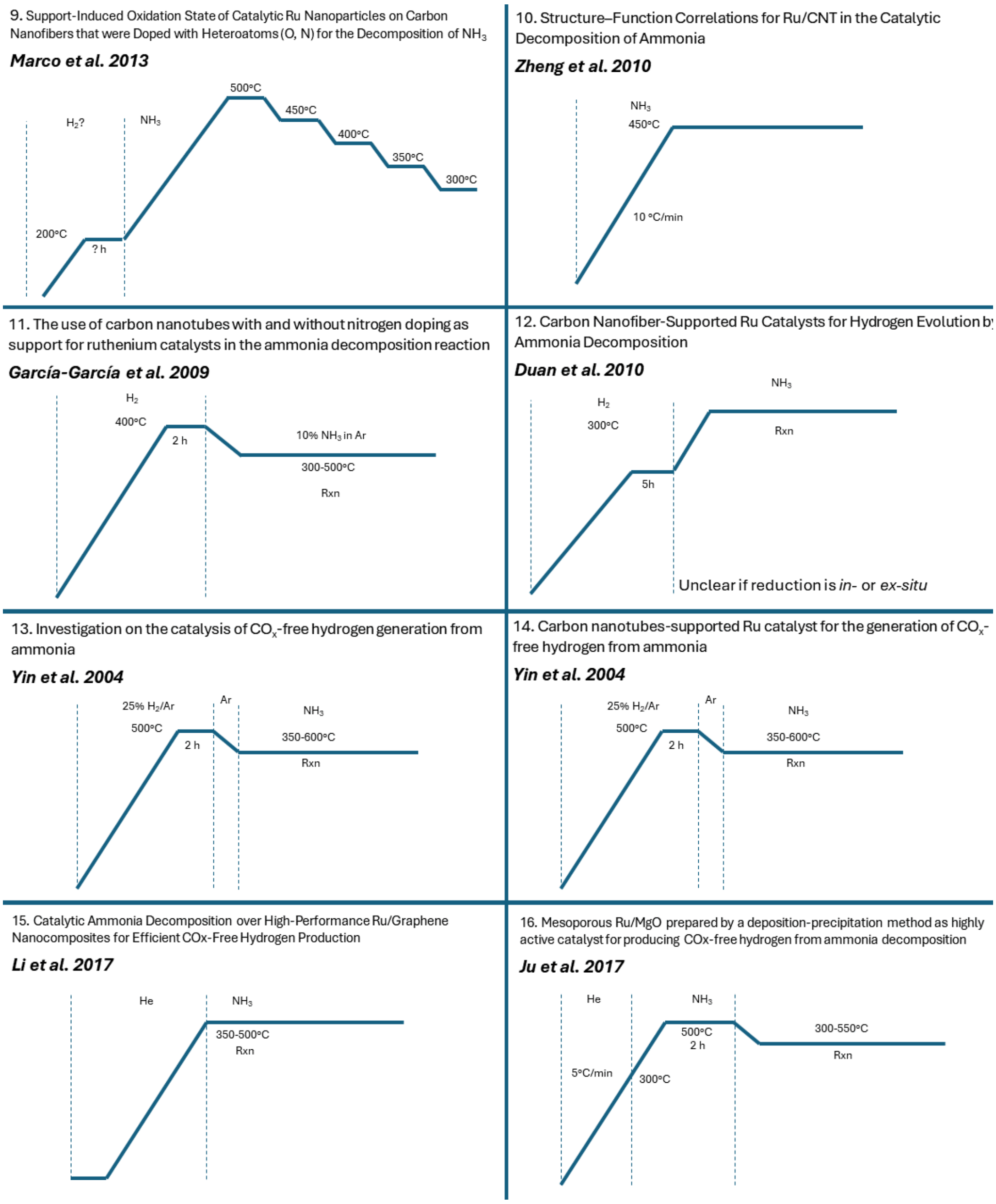

9. Support-Induced Oxidation State of Catalytic Ru Nanoparticles on Carbon Nanofibers that were Doped with Heteroatoms (O, N) for the Decomposition of NH_3

Marco et al. 2013

10. Structure–Function Correlations for Ru/CNT in the Catalytic Decomposition of Ammonia

Zheng et al. 2010

11. The use of carbon nanotubes with and without nitrogen doping as support for ruthenium catalysts in the ammonia decomposition reaction

García-García et al. 2009

12. Carbon Nanofiber-Supported Ru Catalysts for Hydrogen Evolution b Ammonia Decomposition

Duan et al. 2010

Unclear if reduction is *in-* or *ex-situ*

13. Investigation on the catalysis of CO_x-free hydrogen generation from ammonia

Yin et al. 2004

14. Carbon nanotubes-supported Ru catalyst for the generation of CO_x-free hydrogen from ammonia

Yin et al. 2004

15. Catalytic Ammonia Decomposition over High-Performance Ru/Graphene Nanocomposites for Efficient COx-Free Hydrogen Production

Li et al. 2017

16. Mesoporous Ru/MgO prepared by a deposition-precipitation method as highly active catalyst for producing COx-free hydrogen from ammonia decomposition

Ju et al. 2017

Figure 4.8. Schematic diagrams displaying the pre-treatment methodologies from 8 further papers on ammonia decomposition.[69,75,77,79,82,98,110,111]

4.5.3. Testing Pre-treatment Methodologies

The Ru/GNF catalyst reported earlier in this chapter was used to test the pre-treatment methodologies identified from the literature. These are laid out below. Unless otherwise stated, all flow rates are 25 mL min^{-1} and all heating ramp rates are 1 °C min^{-1}.

1 hr reduction – The standard approach to catalyst pre-treatment for ammonia decomposition is a simple reduction of the catalyst under hydrogen gas. For this, 5% H_2 in Ar was flowed, and the temperature was ramped from room temp to 450 °C. This was held for 1 hour before the flow was switched to 5% NH_3 in Ar for the reaction.

Cool post reduction – In a small number of papers, the system is cooled and flushed with inert gas in between the reduction step and the reaction. In this experiment, 5% H_2 in Ar was flowed, and the temperature was ramped to 450 °C and held for 1 hour before cooling to 50 °C under He flow. The flow was changed to 5% NH_3 in Ar, before heating for the reaction to 450 °C.

NH_3 activation 12 hr – Some catalysts benefit from treatment under ammonia flow prior to reaction, such as the Ru/h-BN as reported by Kang *et al.* in 2023. In this protocol, 5% H_2 in Ar was flowed, and the temperature was ramped to 450 °C and held for 1 hour. The flow was then changed to 5% NH_3 in Ar and held for 12 hours, before cooling to 50 °C under He flow. The flow was changed to 5% NH_3 in Ar before heating for the reaction to 450 °C.

NH_3 reduction – As a control experiment, one sample was not pre-treated at all and instead, 5% NH_3 in Ar began flowing and the temperature was ramped to 450 °C for the reaction.

Flush post reduction – To separate the effect of cooling and the effect of flushing with inert gas, an experiment was conducted with a He flush after reduction. 5% H_2 in Ar was flowed and the temperature was ramped to 450 °C. This was held for 1 hour, then the flow was switched to He for 1 hour before finally being switched to 5% NH_3 in Ar for the reaction.

To investigate the effect of heat treatment akin to calcination, 2 further pre-treatments were tested. These were:

Ex-situ heat treat 48 hr – This experiment was intended to mimic the calcination of catalyst under inert gas after synthesis. The catalyst was placed in a ceramic boat inside a tubular furnace. The furnace was flushed with Ar gas (5 mL min^{-1}) and temperature was ramped to 450 °C (5 °C/min) and held for 48 hours. The sample was then placed into the reactor, 5% H_2 in Ar was flowed, and the temperature was ramped to 450 °C and held for 1 hour before cooling to 50 °C under He flow. The flow was changed to 5% NH_3 in Ar, before heating for the reaction to 450 °C.

In-situ heat treat 6 hr – To examine the difference to the catalytic activity upon exposure to air, an in-situ heat treatment experiment was conducted. In the reactor, He was flowed (25 mL min^{-1}) and the temperature was ramped to 450 °C (1 °C/min) and held for 6 hours. The gas flow was switched to 5% H_2 (25 mL min^{-1}) for 1 hour to reduce the sample and then switched to 5% NH_3 (25 mL min^{-1}) for the reaction.

4.5.4. Results and Discussion

The results of pre-treatment experiments are summarised in Figure 4.9 and Figure 4.10. Firstly, as a benchmark, the reduction of the catalyst immediately prior to the reaction before switching to NH_3 results in high catalytic activity that increases as the catalyst self-improves. A 1 hour He flush in between the reduction and reaction results in a reduction in activity, but the self-improvement is retained. Replacing the H_2 reduction step with NH_3 results in an increase in the rate of self-improvement of the catalyst.

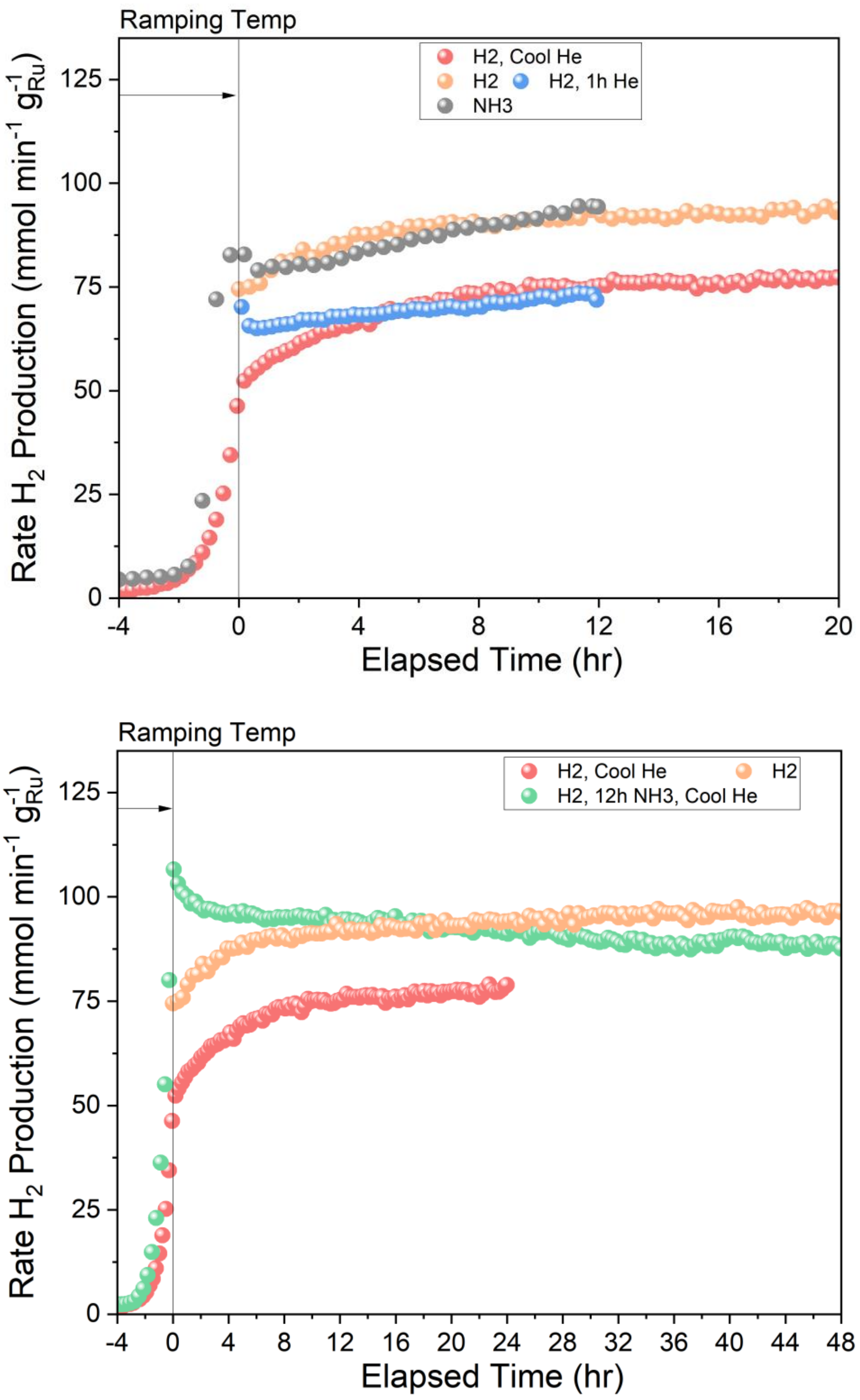

Figure 4.9. *Graphs showing the catalytic activity of Ru/GNF following (A) 4 different reduction pre-treatments over 12 - 20 hours, (B) following 3 pre-treatments over 48 hours.*

If the catalyst is cooled after reduction, the self-improvement behaviour is maintained but the activity of the catalyst is significantly lower than the benchmark catalyst. Cooling the catalyst after an initial 12 hours of reaction result in a much higher activity, but a loss of the self-improving characteristic, and a gentle deactivation of the catalyst. In this case, the catalyst undergoes self-improvement in the activation period, but upon cooling the activity no longer increases.

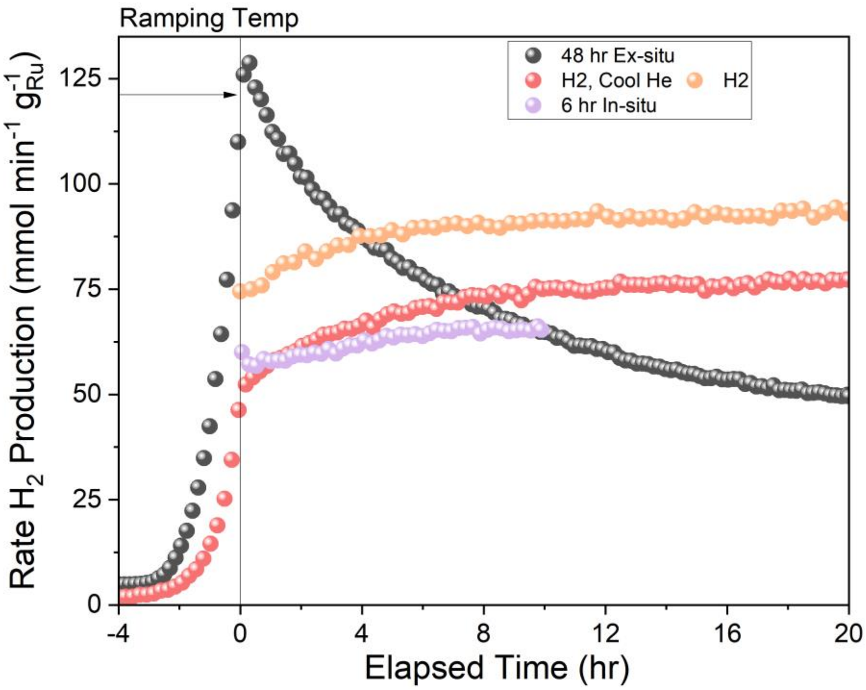

Figure 4.10. *A graph showing the catalytic activity of Ru/GNF following heat treatments in situ (6 hrs) and ex-situ (48 hrs).*

Finally, when the catalyst was treated ex-situ for 48 hours prior to the reaction, initially the rate was higher than after self-improvement at long time-periods. However, the activity decays rapidly, resulting in very poor activity after 20 hrs. When the catalyst is heat treated in-situ prior to the reaction for 6 hours, it begins at a much lower activity than benchmark and retains some self-improvement behaviour. This catalyst self-improves at a much lower rate than the catalysts that were not heat treated.

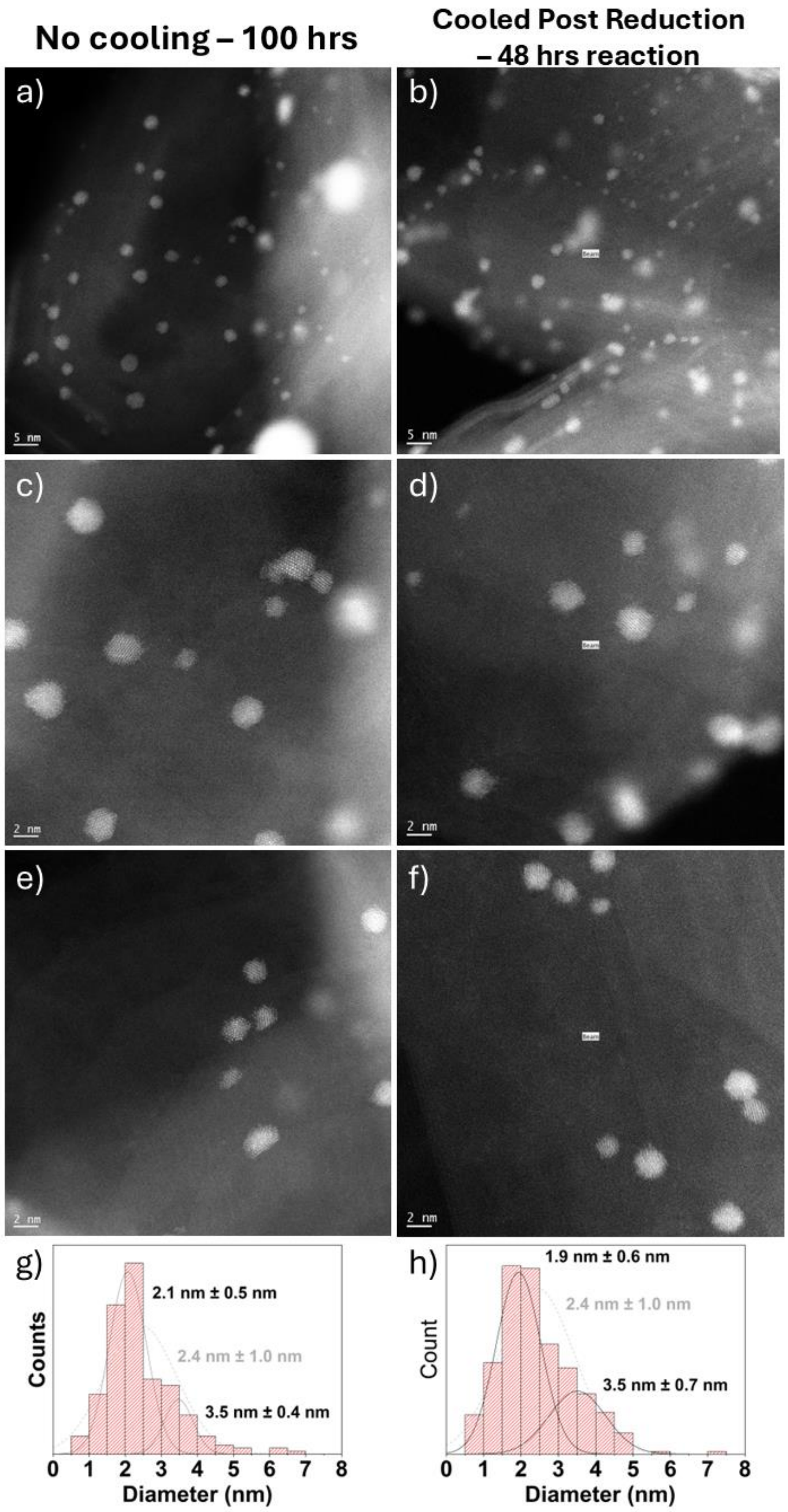

Figure 4.11. *AC-STEM images of Ru/GNF after reaction following 2 different pre-treatments. In the first set (a, c, e, g), the catalyst was reduced in-situ and was not cooled. In the second set (b, d, f, h), the catalyst was reduced in situ, cooled, then ramped back up to reaction temperature under ammonia.*

Figure 4.11 shows AC-STEM images of Ru/GNF post-reaction, comparing the catalyst when it has been cooled during the pre-treatment and when it has not been cooled. The images of both catalysts look remarkably similar and the size distributions of the nanoparticles in both catalysts are very similar, even down to the unique bimodal distribution of nanoparticles. Clearly, the cause of the reduction in activity upon cooling the catalyst cannot be a morphological change (i.e. loss of surface sites) and must be due to another factor.

From this information, it is hypothesised that the self-improvement is caused not by a morphological change, but instead by a chemical change to the metal. During the first 24 hours of the reaction, the metal undergoes a nitridation process that triggers a change in the active site. This change causes the increase in rate. The drop in activity seen after cooling is related to a reduced degree of nitridation of the Ru.

When the catalyst is reduced prior to the reaction, the result is a slower increase in activity than when the catalyst is reduced directly under ammonia flow. In this situation, the surface area has already reduced somewhat as the worm-like nanoparticles of Ru agglomerate somewhat, resulting in larger flat worms of Ru with a larger footprint (this can be seen in Figure 4.12 for reference). These larger nanoparticles are expected to have a lower proportion of surface atoms, leading to a slower nitridation process after the reduction of the nanoparticles. This results in the slower rate of increase in the 1 hr H_2 reduction compared to direct ammonia reduction. Interestingly, the final activity of the hydrogen-reduced sample is very similar to that of the ammonia-reduced sample as the sample has not sintered to a great enough extent to prevent the entire nanoparticle to be nitrided.

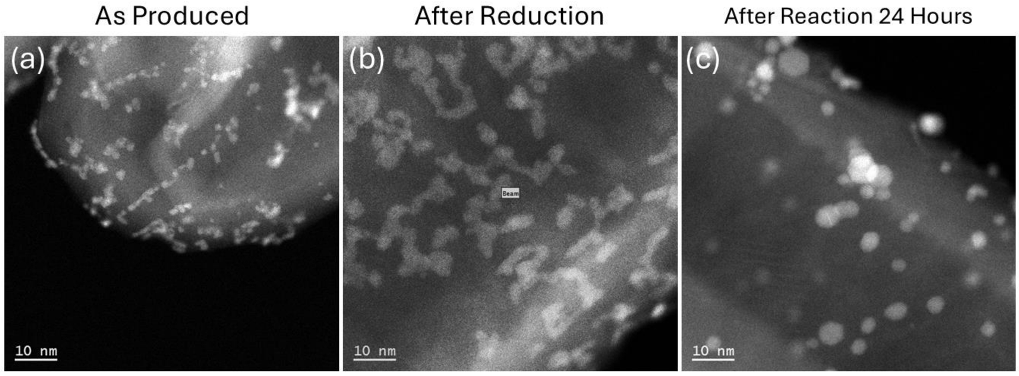

Figure 4.12. *Reference AC-STEM images of Ru/GNF samples as produced (a), after reduction (b), after reaction for 24 hours (c).*

The same cannot be said for the reduced-cooled sample, whose activity is significantly less than the hydrogen-reduced and ammonia-reduced samples. In this case, the flushing and cooling stage is significantly long enough (14 hrs total in cool, flush and heating ramp) that the catalyst is able to agglomerate into nanoparticles with a much lower proportion of surface atoms. When the reaction then begins after the catalyst has reached temperature, the nitridation is only able to take place on the surface of the nanoparticle, reducing the number of total possible surface sites. This observation suggests that even the RuN in the centre of the nanoparticles affects the activity of the catalyst.

In the flush post-reduction sample, a similar reduction in rate increase and final rate is seen to the flushed-cooled sample. It follows that the 1 hour of heating under He following reduction allows sintering to occur, which means that full nitridation of the nanoparticles cannot take place. This simple result clearly displays how crucial the initial stages of the reaction are for the catalysts' activity and stability.

When the catalyst is cooled and flushed after an initial 12-hour activation period under NH_3, the catalyst maintains the increased activity but begins to slowly deactivate. In this case, the catalyst undergoes significantly more complete nitridation than when cooled and flushed directly after reduction. However, the catalyst has not completed its self-improvement and therefore when it is flushed and cooled, it begins to deactivate once brought back into reaction conditions. If the activation stage was increased to 36-48 hours (the time until the activity plateaus), then it is likely that this degradation would likely be reduced, but this has yet to be seen.

Ex-situ heat treatment for 48 hours gives a large spike in activity, which is likely due to the formation of crystalline nanoparticles with a larger concentration of B5 sites than the catalyst before calcination. These particles aren't resistant to agglomeration however, resulting in fast deactivation of the catalyst. The 6 hour in-situ heat treatment reduces both the rate and the catalyst's ability to self-improve. The profile of this reaction is remarkably similar to the flush post-reduction sample, in that the self-improvement rate is reduced due to the agglomeration of nanoparticles prior to the activation process. Unlike the aforementioned sample, this in-situ heat treated sample also significantly reduces in final activity, which suggests an even less-complete nitridation of the nanoparticles.

This relatively small set of pre-treatment conditions tests have not only helped to identify the pre-treatment conditions that will produce the highest activity catalyst, but also the conditions that will cause the catalyst to perform worse. Further, this set of experiments has revealed the importance of NH_3 in the early stages of catalysis over Ru/GNF.

As a final note, I will suggest a short list of pre-treatment experiments to conduct on promising catalysts. These aim to provide jumping off points for further optimisation of conditions. For example, if the catalyst is most active after a H_2 reduction step, then this can be further optimised by testing longer or shorter reduction times at different temperatures. These tests will also indicate the catalysts resistance towards improper handling, such as flushing at reaction temperature and being heated outside of reaction conditions.

These pre-treatments do not include any prior calcination steps, which should be optimised before optimising pre-treatment. When optimising the calcination and testing for activity, the default 1 hr reduction methodology should be used as pre-treatment.

A short list of pre-treatment tests:

1. **1 hr reduction.** Flow H_2 at room temperature before ramping the reactor temperature to 450 °C. Hold H_2 flow for 1 hour, then switch to NH_3 and ramp to reaction temperature for the course of the reaction.
2. **1 hr NH_3 reduction.** Flow NH_3 at room temperature before ramping the reactor temperature to 450 °C and holding for 1 hour. Ramp to reaction temperature and hold for the course of the reaction.
3. **48 hr heat treatment**. Under a flow of Ar or He, heat the catalyst to reaction temperature for 48 hours, before testing the catalyst using the “1 hr reduction” pre-treatment.
4. **Flushing at Temperature.** Flow H_2 at room temperature before ramping the reactor temperature to 450 °C. Hold H_2 flow for 1 hour, flush with He for 1 hour and then switch to NH_3 flow and ramp to reaction temperature.
5. **Cooling and flushing**. Flow H_2 at room temperature before ramping the reactor temperature to 450 °C. Hold H_2 flow for 1 hour, then switch to He flow and cool to 50 °C. Switch to NH_3 flow and ramp to reaction temperature.

These treatments will provide a good foundation for the understanding and best reporting of a new catalyst. Firstly, they will provide an initial pre-treatment in which the catalyst performs best, ensuring that the measured rate is comparable with literature values. As seen from the results laid out in this chapter, the pre-treatment has a huge impact on the final catalytic activity measurement. Secondly, the understanding gained about the behaviour of the catalyst under different reaction conditions will help the researcher to best optimise their catalyst.

4.6. Conclusions and Further Work

The Ru/GNF catalyst developed and studied in this chapter demonstrates a rare self-improvement behaviour during ammonia decomposition, with catalytic activity increasing significantly over the initial hours of reaction. This enhancement is not attributable to morphological changes in the Ru nanoparticles, as evidenced by identical AC-STEM images and nanoparticle size distributions before and after activation. Instead, the data strongly support a chemically driven transformation - such as the progressive nitridation of the Ru nanoparticles - as the underlying mechanism for the observed increase in activity.

The nitridation process appears to modify the electronic structure of the active sites, enhancing their catalytic performance. Importantly, the extent and rate of this transformation are highly sensitive to the pre-treatment conditions. Protocols involving direct exposure to ammonia at reaction temperature lead to a more complete nitridation and thus faster self-improvement, while cooling or flushing steps before the reaction hinder the process, leading to reduced activity and incomplete transformation of the catalyst.

These findings show the critical role of the beginning stages of the reaction in determining final catalyst performance. Ru/GNF not only offers high initial activity but changes under reaction conditions to become even more active. This behaviour opens new avenues for designing catalysts that are not only stable but also capable of adapting and improving during operation. The remaining chapters focus first on a deeper understanding of the structure and behaviour of the nanoparticles on the surface of the GNF. Then, a deeper study is conducted by catalysis, spectroscopy and microscopy to elucidate the mechanism by which the nanoparticles self-improve by nidridation.

5. The Application of Identical Location Microscopy to Catalyst Systems

Electron microscopy is a commonly used technique for measuring the size of catalyst nanoparticles and is sometimes also used to study the morphological changes of a catalyst that occur during a reaction. Typically, this involves the analysis of images of the catalyst before and after reaction to produce size distribution histograms. These are then compared to study the changes to the nanoparticles. Due to the nature of this analysis, any individualistic structures present in nanoparticles are averaged into the normal distribution and therefore lost. In this chapter, an alternative to this "ensemble averaging" analysis is presented, whereby individual nanoparticles are studied at various points throughout the reaction.

5.1. Introduction

Heterogenous nano-catalysts are polydisperse materials with varying metal particles, with each particle possessing its distinct shape, size, and structure, and hence its unique catalytic property. When we test the performance of a catalyst, the catalytic performances of individual particles are averaged. In the case of activity per gram of metal, the integral activity is divided by the total amount of metal in the catalyst. Therefore, for convenience, it is conventional to average the size of particles and correlate the average size with the macroscopic properties of the catalyst. For example, when the average size increases, the fraction of surface atoms decreases, which is expected to lead to reduced catalyst activity.

The situation is complicated by the fact that heterogeneous catalysts with small particle sizes are not static materials. They undergo changes over time under reaction conditions, which are usually detrimental due to particle coarsening, surface poisoning, or metal leaching.[112] Therefore, heterogeneous catalysts have been extensively studied to understand how to avoid deactivation.[113] However, changes in the catalyst during the reaction can also be beneficial, but it is discussed less often. These changes usually occur in a short period of time at the early stages of the reaction and are referred to as catalyst conditioning or activation. In some rare cases, these self-improvements of the catalyst continue over several hours through the reaction as observed in hydrogen production from water[114] and from ammonia.[103] The latter reaction is particularly topical because ammonia is gaining popularity as a zero-carbon energy vector.[75,115,116] It is crucial to comprehend the catalyst evolution mechanism at the individual particle level, particularly for ruthenium, which is considered the most effective metal for NH_3 decomposition, and can be supported on the surface of metal oxide,[83,117,118] nitride,[103,106] or carbon materials.[75,104,119,120]

Our study used identical location scanning transmission electron microscopy (IL-STEM) to examine changes in a Ru catalyst during the ammonia decomposition reaction. By tracking the evolution of individual nanoclusters in specific locations, we found that both Ostwald ripening and coalescence processes occur at a local scale. The major restructuring of Ru nanoclusters occurs due to the larger fraction of surface atoms in nanoclusters compared to traditional nanoparticles and the strong bonding of Ru to the carbon support. The number of atoms in each Ru nanocluster increases as the footprint and number of layers expand during H_2 treatment. However, during the NH_3 decomposition reaction, the footprint decreases while the number of atoms continues to grow, causing the nanoclusters to become taller and progressively pyramidal with stepped edges. These nanoscale changes are correlated with the increasing rate of hydrogen production from ammonia.

The aims of this chapter are as follows:

1. To develop a method of sample production for the identical location AC-STEM analysis of Ru/GNF.

2. To study the morphology of Ru/GNF before and after several different points of a reaction.
3. To compare the identical location microscopy technique with ensemble averaging.
4. To understand the effect of the morphological changes of Ru/GNF on the activity of the catalyst.

5.2. Material preparation and catalytic performance

Using magnetron sputtering, Ru bulk metal was dispersed to an atomic state, and Ru atoms were deposited directly onto the support material, such as graphitised carbon nanofibers (GNF). This approach allows for a solvent-free assembly of metal nanoclusters with no additional agents, such as ligands or counterions, thus yielding pure metal in direct contact with support material.[121] This approach yields much better images in electron microscopy due to much less surface interference. GNF consists of a set of stacked graphitic cones (Figure 5.1. A,B) which has been shown to improve stability,[101] selectivity,[122] or reusability[123-125] of Pt, Pd, Rh, Cu, Au, Ru, Mo, and other catalysts in thermal or electrochemical catalysis.

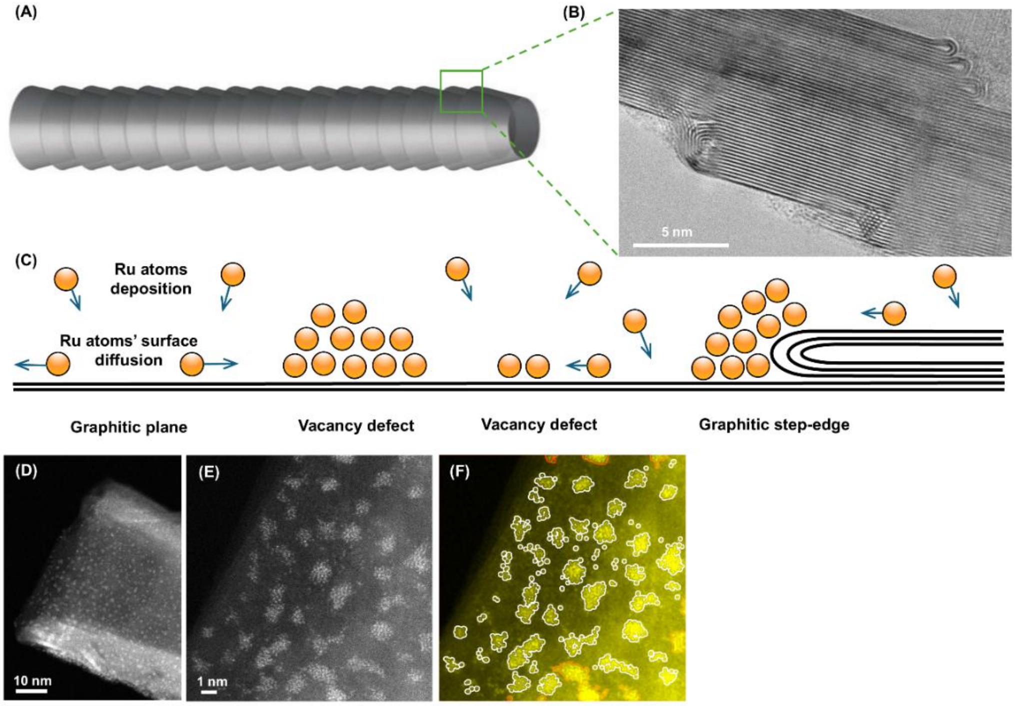

Figure 5.1. (A) Schematic and (B) TEM image show that GNF consists of a set of stacked graphitic cones. (C) Schematic representation of atomic deposition process of Ru onto a graphitic surface leading to self-assembly of nanoclusters at room temperature. (D) Annular dark field aberration-corrected STEM (AC-STEM) images of a GNF with Ru nanoclusters. GNF has a cylindrical shape with a hollow interior. High-magnification AC-STEM image of Ru nanoclusters on GNF, raw unprocessed (E) and processed by a custom Python program with Ru atoms and nanoclusters marked by white perimeters (perimeters of clusters that extend to outside the field of view are red) (F).

Inspection of as-prepared Ru/GNF indicates that during Ru deposition metal atoms diffuse on the hexagonal lattice of the support until they become immobilised at defect sites. This results in the nucleation of metal nanoclusters, the size of which is determined by the surface density of deposited metal atoms, the density of defects, temperature, and metal-supporting bonding energy, as predicted by the kinetic theory[102] (Figure 5.1 C).

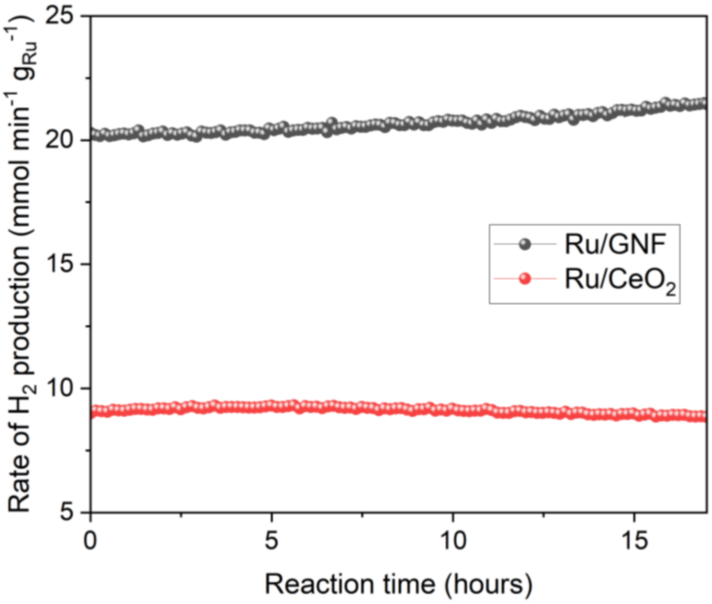

Figure 5.2. Ru/GNF and Ru/CeO₂ catalytic activity comparison for H₂ production from ammonia decomposition.

Prior to the catalytic testing for ammonia decomposition, catalysts were reduced under H_2 for 1 hour at 450 °C, a commonly used protocol to activate catalyst before admitting reactants.[72,120,126] The catalyst was then cooled to 50 °C, and 5% ammonia in argon was passed over the catalyst before the temperature was ramped. The catalytic activity of Ru on GNF was evaluated by measuring the production rate of H_2 at fixed temperature of 450 °C, typical for this reaction[52]. Interestingly, Ru/GNF shows an increase in catalytic activity over 17 hours of reaction (Figure 5.1 G), which is unusual behaviour as compared with ruthenium on traditional catalyst supports, such as Ru/CeO_2, which shows a progressively decreasing activity over time (Figure 5.2).

To understand the atomic mechanisms behind Ru/GNF self-improving activity, the catalytic material was examined by electron microscopy at different stages of the process.

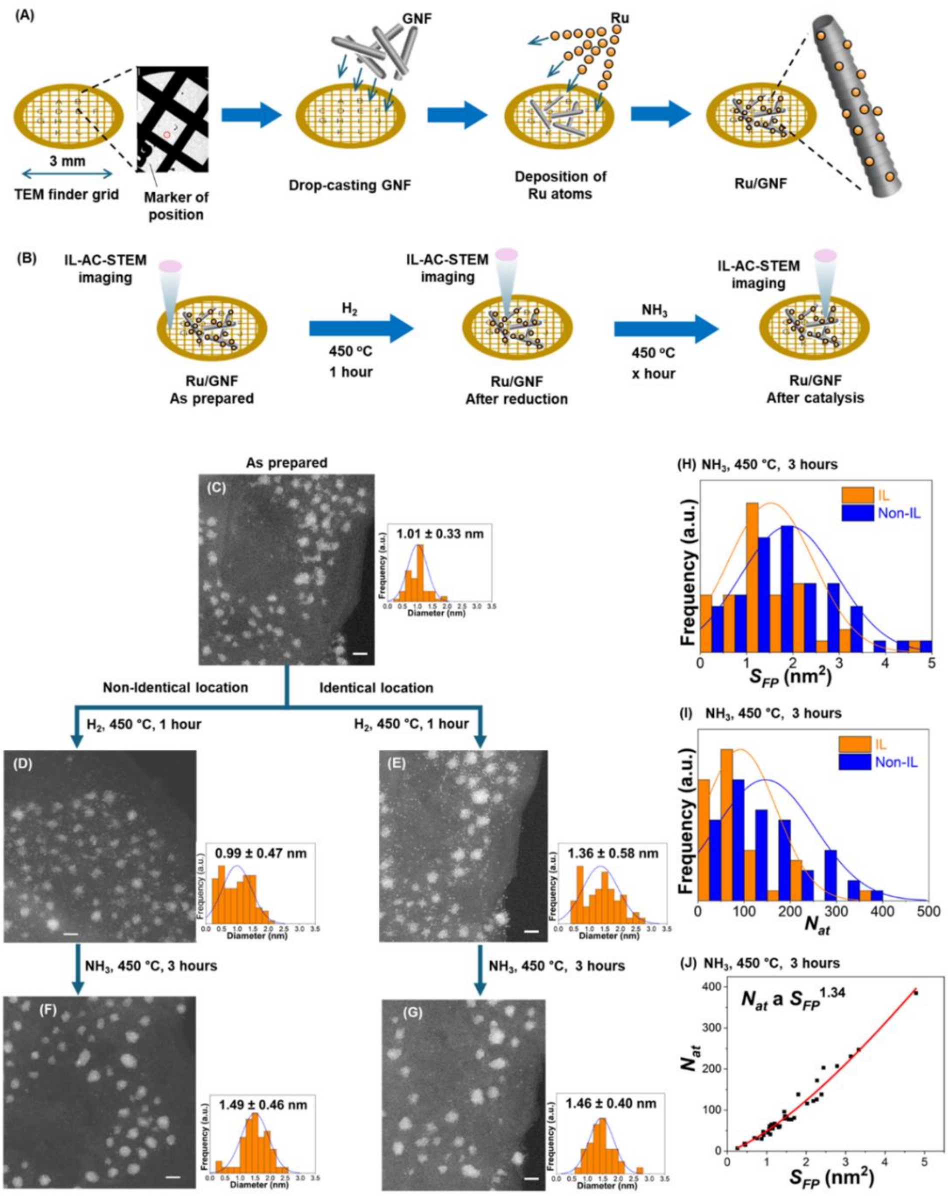

Figure 5.3. (A) Workflow of the Ru/GNF catalyst preparation on the TEM finder grid. (B) IL-STEM imaging of the nanoclusters after different stages of the reaction. AC-STEM images of as-prepared Ru/GNF (C) and after having been subjected to H2 at 450 °C (D, E) and subsequently NH3 at 450 °C (F, G) and imaged in non-identical (left) or identical (right) locations, respectively, with corresponding size distribution diagrams shown beside each STEM micrograph (scale bar, 2 nm). Distributions of the footprint area, SFP (H) and total number of atoms, N_{at} (I) in Ru nanoclusters after 3 hours NH3 at 450 °C measured for micrographs in identical and non-identical locations. Correlation of the N_{at} and S_{FP} of Ru nanoclusters after 3 hours NH3 at 450 °C (J), where R2 is 0.971.

5.2.1.1. Identical location analysis of the catalyst

It is conventional to use electron microscopy to study changes in the size of catalyst particles. This involves comparing TEM images before and after a reaction. Electron microscopy is a powerful tool that can measure changes with atomic precision at the single particle level. However, a heterogenous catalyst always has some degree of polydispersity, i.e. particles are non-identical. Therefore, structural information for individual catalytic particles is typically averaged in the distribution of sizes and shapes. The alternative to the ensemble averaging analysis is to use TEM imaging in the same areas of the sample before and after each reaction stage. We prepared the Ru/GNFs catalyst directly on TEM grids (Figure 5.3 A,B), which allows us to average information for an ensemble of particles or study the evolution of individual particles in identical locations before and after the reaction. This provides a series of stop-frame images elucidating dynamics at the single-particle level. GNF supports, consisting of a highly conducting and chemically stable graphitic lattice, lend themselves to this approach very well due to their low STEM contrast and high electron beam stability. In addition, the positions of GNFs on the TEM finder grid with alphanumerically labelled areas allow us to return to the same set of nanoclusters before and after the reaction.[127] Below, we show that applying the IL-STEM approach to Ru on GNF at various reaction stages can provide structural and dynamic information for individual particles while representing the overall sample (Figure 5.3 C-I).

Using this approach, the evolution of nanoclusters was studied in several uniquely defined areas of the sample, each approximately 20 nm by 20 nm, by imaging the same area before and after the reaction (Figure 5.3 C, E, G). STEM image analysis in this format allows qualitative assessment of atomic order in individual nanoclusters from the image and FFT plot, as well as quantitative analysis of the number of atoms (N_{at}) comprising the nanocluster and its footprint (S_{FP}) (Figure 5.3 H,I), and the number of atomic layers (N_l) which can be deduced from these parameters based on the hexagonal close packed (hcp) lattice of ruthenium. Next, the comparison of the IL and ensemble averaging (non-IL), approaches for nanocluster size analysis indicates a similar trend but differs numerically. For example, the average size of the nanoclusters in the same area of GNF increases by 35% after the H_2 treatment step and a further 7% after the first three hours of the NH_3 decomposition reaction (Figure 5.3 C,E,G), while the same analysis for different areas of GNF selected at random shows no changes after hydrogen treatment and an increase of 50% after 3 hours of reaction (Figure 5.3 C,D,F). Changes in nanoclusters' distribution within the same area hold a greater significance because we are observing the evolution of the specific set of atoms and nanoclusters in the same local nano-environment. Hence, the results obtained from the IL analysis should be considered more definitive for understanding the atomistic mechanisms of nanocluster evolution. Furthermore, changes in macroscopic properties of Ru/GNF, such as catalyst activity, can be linked to information obtained from local scale analysis without the need to gather statistics from many random areas.

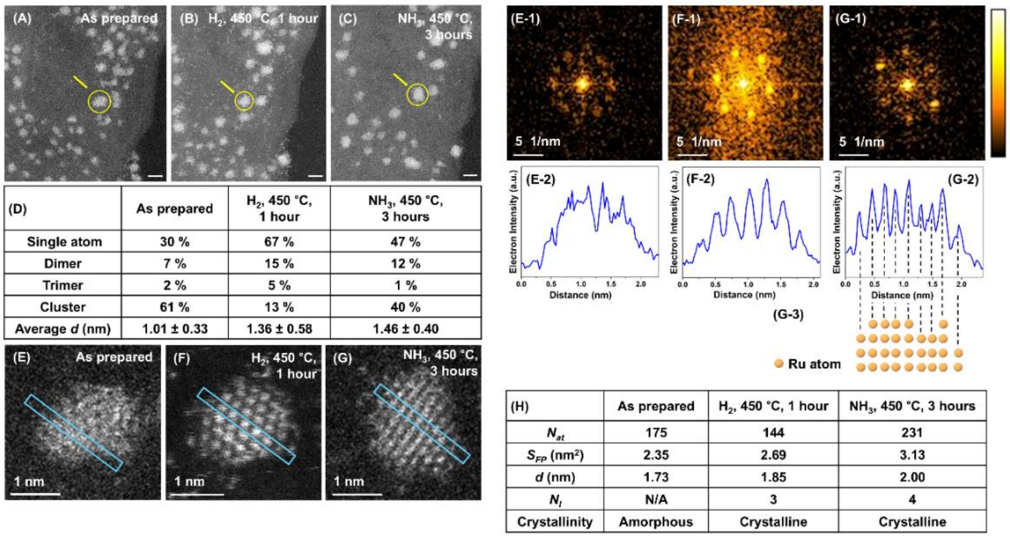

(D)	As prepared	H_2, 450 °C, 1 hour	NH_3, 450 °C, 3 hours
Single atom	30 %	67 %	47 %
Dimer	7 %	15 %	12 %
Trimer	2 %	5 %	1 %
Cluster	61 %	13 %	40 %
Average d (nm)	1.01 ± 0.33	1.36 ± 0.58	1.46 ± 0.40

(H)	As prepared	H_2, 450 °C, 1 hour	NH_3, 450 °C, 3 hours
N_{at}	175	144	231
S_{FP} (nm²)	2.35	2.69	3.13
d (nm)	1.73	1.85	2.00
N_l	N/A	3	4
Crystallinity	Amorphous	Crystalline	Crystalline

Figure 5.4. IL-STEM images of Ru/GNF at different stages: as-prepared (A), after 450 °C in H2 (B), and after 450 °C in NH3 (C) (scale bar, 2 nm). A tabulated summary of changes in the population of single atoms, dimers,

trimers and nanoclusters, and the nanoclusters' average d for each stage (D). An example of IL-STEM analysis for the evolution of a specific single Ru nanocluster (marked with the arrow in A-C) through different reaction stages (E-G), with corresponding FFT patterns (E1-G1) and intensity line profiles (E2-G2) cut along the directions marked on STEM images. Atomic columns in nanocluster (F) are aligned parallel to the electron beam of STEM, which allows determining the number of Ru atoms in each column (F3). A summary of key structural parameters for the single Ru nanocluster at different reaction stages (H), where N/A means not applicable.

5.3. Individual Ru nanocluster evolution

The IL-STEM approach's most important feature is its ability to track the evolution of individual nanoclusters step by step. If the nanocluster remains in approximately the same position with respect to the landscape of the GNF support (Figure 5.4 A-C), it can be located and examined in detail after the reduction in H_2 and after the reaction in NH_3 (Figure 5.4 E-G). The degree of metal atom ordering can be visually assessed from the STEM images or from the FFT of the images (Figure 5.4 E1-G1).[128,129] In addition, in cases where atomic columns in the metal nanocluster align with the direction of the electron beam, the intensity line profile drawn across the nanocluster can be used to count the number of atoms in each atomic column from its peak intensity (Figure 5.4 F3).[130] Simultaneously, the total N_{at} and area of S_{FP} can be conveniently determined for the same nanocluster directly from the integral intensity of the STEM image and perimeter measurement, providing a full description of its structure (Figure 5.4 H).

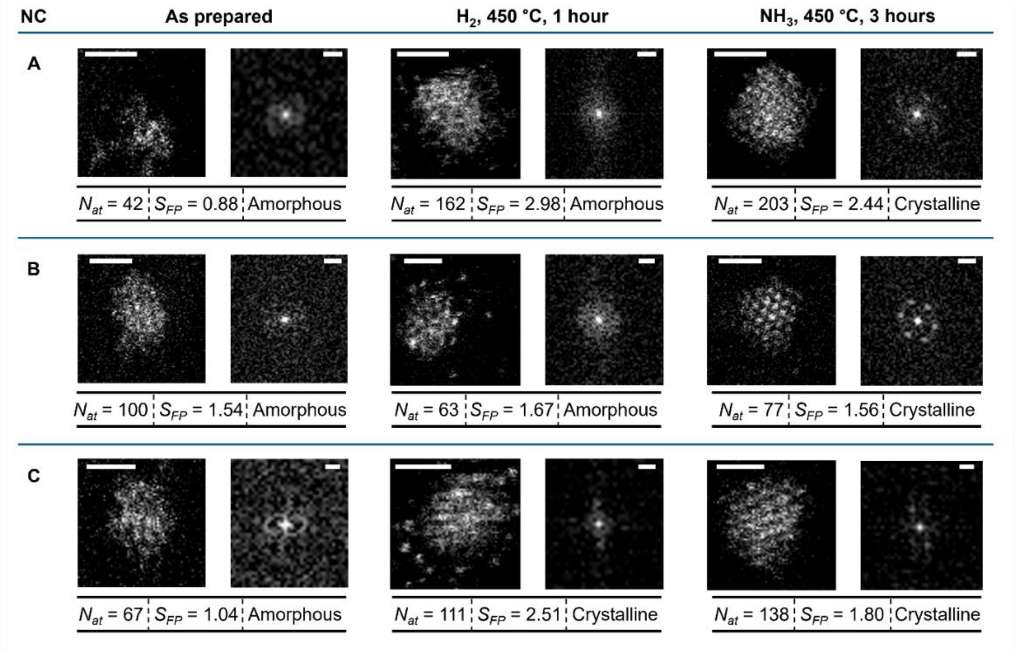

Figure 5.5. Evolution of Ru/GNF after H2 treatment for 1 hour and NH3 decomposition reaction for 3 hours: identical location observation of individual nanocluster. STEM images with FFT patterns shown on the right side, and key nanocluster parameters below each image. The scale bar in the STEM image is 1 nm. The scale bar in FFT patterns is 5 1/nm.

For example, changes in S_{FP} and N_{at} can be directly traced for 12 individual nanoclusters (Figure 5.5), showing various types of behaviour. For N_{at}, the majority undergoes an increase in H_2, followed by a further increase in NH_3 but to a lesser extent, while for S_{FP}, the majority undergoes an increase in H_2, followed by a decrease in NH_3. This implies that during the stage of NH_3 decomposition reaction, the nanocluster becomes more compact (increasing N_{at} with decreasing S_{FP}).

By plotting N_{at} against S_{FP} (Figure 5.6), one can deduce information about the 3D shape of the nanoclusters. The plot can be fitted with a power law with an exponent of 1.3, suggesting that the nanoclusters are not cylindrical or disk-shaped with S_{FP}-independent height but rather closer to hemispherical or pyramidal. A deeper level of analysis can be achieved from the image intensity profile, allowing for the intensity of the atomic columns of Ru to be examined. This intensity is proportional to the number of atoms in the respective column, thus providing the 3D shape of the nanocluster as a pyramid with stepped sides and a flattened top, with the N_l increasing from 1 at the base to 4 at the apex (Figure 5.8). Analysis of other examples of well-defined, trackable nanoclusters reveals that atomic transformations are strongly dependent on the local environment, with many nanoclusters following the same general trend as described above, i.e. both crystallinity and S_{FP} increasing after H_2 treatment, with a further increase of crystallinity but a decrease of S_{FP} after ammonia reaction (Figure 5.5).

Furthermore, analysing the AC-STEM Ru images allows us to evaluate the degree of atomic order in the nanoclusters. For example, a typical Ru nanocluster formed at room temperature on the carbon support lacks atomic ordering (Figure 5.7 E). However, after the treatment in H_2, ordered columns of atoms emerge (Figure 5.7 F). FFT image analysis confirmed that the overall trend is that the nanoclusters' degree of crystallinity increases, especially after the NH_3 step of the reaction.

5.3.1.1. Evolution of Ru nanocluster in groups

IL-STEM determined that the decrease of nanocluster S_{FP} and the increase of N_{at} and N_l contribute to the nanocluster's increasing crystallinity, as Ru nanoclusters become more compact. However, it does not explain the source of the extra Ru atoms. This was answered by considering the nearest neighbourhood of each nanocluster. We split the overall area under investigation into 9 distinct sub-areas, such that changes for several nanoclusters can be tracked from one step to another. Overall, we identified three types of behaviour of nanoclusters: (1) migration followed by coalescence, (2) migration without coalescence, and (3) Ostwald ripening. The latter appears more prevalent during the H_2 reduction step as a particular nanocluster disperses into atoms feeding into nanoclusters nearby (Figure 5.6). Based on changes in the size of nearest neighbours, the disappearing nanocluster typically transfers its atoms to at least three adjacent nanoclusters. Migration and coalescence events both appear to be present during the H_2 reduction and NH_3 decomposition and typically involve two or three nanoclusters merging into one (blue arrows in Figure 5.6). Identical location analysis revealed that during this mechanism, two or three nanoclusters move towards each other, and these become merged into a single structure.

Both Ostwald ripening and migration followed by coalescence decrease the number of nanoclusters while increase the N_{at} per cluster and height. Thus, inter-cluster separations become larger, with a wider expanse of carbon support opening up between the nanoclusters. Inspection of the space created by disappearing nanoclusters reveals the presence of single Ru atoms adsorbed on carbon support after H_2 conditions. In contrast, the fraction of single atoms after NH_3 decomposition reaction is significantly lower (Figure 5.7).

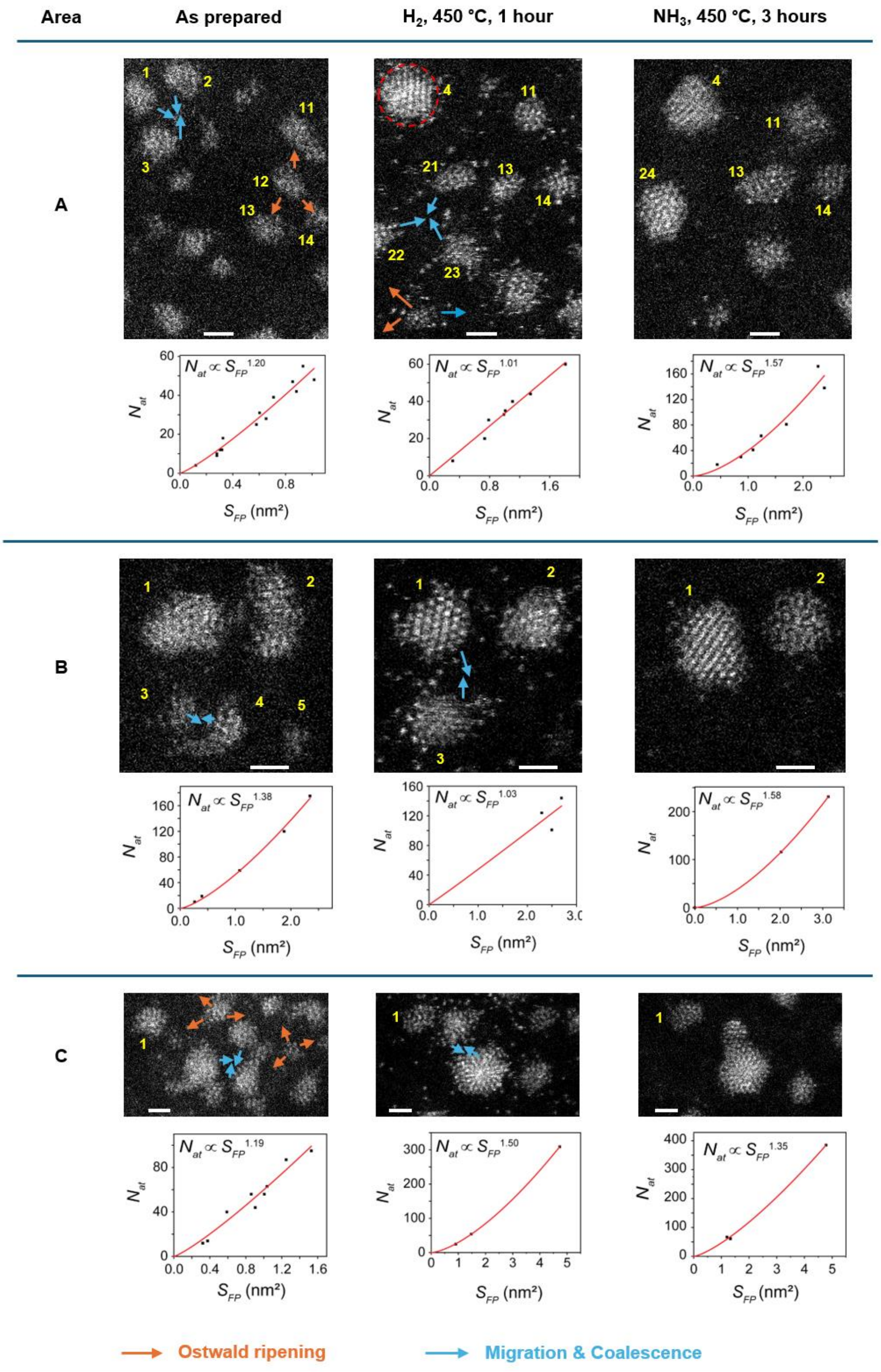

Figure 5.6. Evolution ¬of groups of nanoclusters after H_2 treatment for 1 hour (middle column) and NH_3 decomposition reaction for 3 hours (right column): identical location observation. Changes in nanoclusters are indicated by arrows (orange = Ostwald ripening; blue = migration and

coalescence). Positions of nanoclusters that disappeared due to Ostwald ripening are marked with white dotted circles. A plot correlating Nat and SFP is shown for each area beneath the micrographs. Scale bar is 1 nm. The clusters circled in red were not included in the analysis because it extends beyond the field of view.

5.3.1.2. Ru nanocluster evolution over 12 hours of NH_3 decomposition reaction

We performed identical location measurements for Ru/GNF as-prepared and after 12 hours of the ammonia decomposition reaction (Figure 5.7). Remarkably, the nanocluster S_{FP} does not increase beyond that of 3 hours reaction (Figure 5.7 C). The pyramidal shape with well-defined edges due to atomic ordering with steps appears very stable under the ammonia decomposition reaction conditions (Figure 5.7 E).

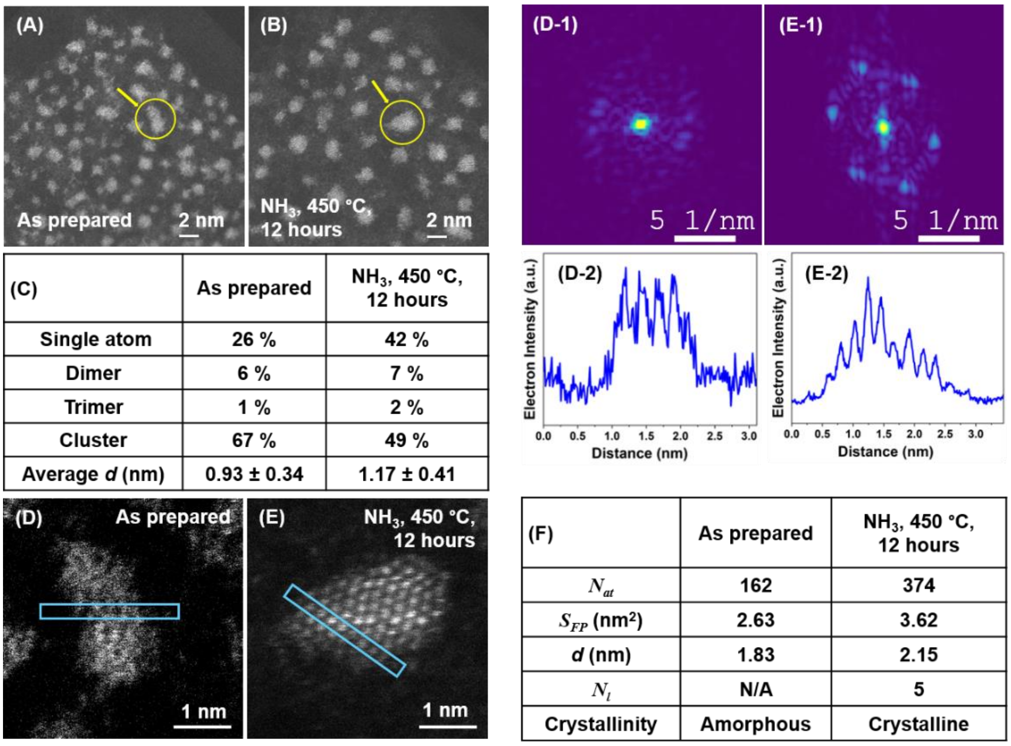

(C)	As prepared	NH_3, 450 °C, 12 hours
Single atom	26 %	42 %
Dimer	6 %	7 %
Trimer	1 %	2 %
Cluster	67 %	49 %
Average *d* (nm)	0.93 ± 0.34	1.17 ± 0.41

(F)	As prepared	NH_3, 450 °C, 12 hours
N_{at}	162	374
S_{FP} (nm²)	2.63	3.62
d (nm)	1.83	2.15
N_l	N/A	5
Crystallinity	Amorphous	Crystalline

Figure 5.7. IL-STEM images of Ru/GNF at different stages: as-prepared (A) and after 450 °C in NH3 (B). A tabulated summary of changes in the population of single atoms, dimers, trimers and nanoclusters, and the

nanoclusters' average d for each stage (C). An example of IL-STEM analysis for the evolution of a specific single Ru nanocluster (marked with the arrow in A, B) through different reaction stages (D, E), with corresponding FFT patterns (scale bar, 5 1/nm) and intensity line profiles (D2, E2) cut along the directions marked on STEM images. A summary of key structural parameters for the single Ru nanocluster at different reaction stages (F), where N/A means not applicable.

5.4. Discussion

Our study indicates that the catalytic activity of ruthenium nanoclusters on carbon increases with time, which contrasts with Ru on metal oxides, such as Ru/CeO_2 whose activity gradually decays – a typical behaviour of heterogenous catalysts (Figure 5.2). Understanding the source of the increasing activity is crucial, as it can provide a blueprint for designing new types of catalysts. Our electron microscopy measurements showed that the average number of atoms per Ru nanocluster increases in the initial 3 hours of the reaction (Figure 5.3 C-I, Figure 5.4 D) and does not increase substantially beyond this over 12 hours of reaction (Figure 5.7 C). Hence, the fraction of surface Ru atoms per nanocluster decreases and levels off, contradicting the observed rise of the activity of Ru/GNF. To explain this unexpected phenomenon, a simple averaging of structural information does not prove to be fruitful. Indeed, the ensemble-averaging analysis masks essential features of the nanocatalysts, making it challenging to relate nanoscale structure to the macroscopic properties of the material, including catalytic activity. For instance, particle average size or diameter concepts cannot be fully described at the nanoscale because of the non-spherical, irregular shapes of the metal nanoclusters, and it does not carry information about the third dimension (particle height). Furthermore, the process of averaging obscures details about various local particle environments, such as the proximity and number of nearby particles. Since the local environment can significantly impact the behaviour of individual particles, it is challenging to discern the atomic mechanisms responsible for these changes through ensemble averaging analysis.

Fortunately, IL-STEM imaging provides a solution to the issue of ensemble averaging by enabling the tracking of individual catalyst particles' evolution from one stage of the reaction to another (Figure 5.4 E,G,I). In addition, considering that the diameter of the TEM grid is macroscopic, ca. 3 mm across, the IL-STEM analysis can be performed on several areas of the grid. Hence such measurements are completely independent of each other (Figure 5.4 C-I) which ensures the experimental reproducibility as well as representativeness of the area chosen for deep analysis of the whole macroscopic sample. Using this approach allowed us to assess the evolution of individual Ru nanoclusters during catalyst activation (450 °C, H_2) and the initial phase of the ammonia decomposition reaction (450 °C, NH_3). We employed nanoclusters' footprint S_{FP} alongside the total number of atoms in the nanocluster, N_{at} that can be estimated from the integral intensity of STEM image, as more meaningful descriptors instead of the *average size* or *diameter*. Considering a close-pack of Ru metal atoms in the base layer of nanocluster, the number of layers N_l can be inferred from S_{FP} and N_{at}. These parameters, combined with the line intensity profiles, provide a comprehensive description of the three-dimensional shape of the nanoclusters and their evolution in the reaction, which was monitored by IL-STEM approach (Figure 5.5 E2-G2, Figure 18, Figure 5.7 D2-E2). This method led us to conclude that the N_{at} in each Ru nanocluster increases due to the expanding S_{FP} and the increasing N_l during H_2 treatment. However, during the NH_3 decomposition reaction, S_{FP} decreases while N_{at} continues to grow so that the nanoclusters become taller and progressively pyramidal, with stepped edges (Figure 5.8 A). The correlation of S_{FP} with N_{at} showed an increase of the scaling power n from 1.2 to 1.57, 1.38 to 1.58 and 1.19 to 1.35 in $N_{at} \sim (S_{FP})^n$ (Figure 5.6), which also confirms that clusters become more three-dimensional.

The determination of the precise atomic structure of the nanoclusters, such as in Ru/GNF, is challenging. Our IL-STEM imaging and FFT image analysis clearly indicate an increasing crystallinity of the nanoclusters during the reaction, but their structural analysis is complex. However, when the atomic columns of Ru in nanoclusters are parallel to the electron beam (Figure 5.4 F,G), the observed STEM images were consistent with Ru hcp lattice structure.

It is also important to consider the relationship of Ru atoms with the carbon lattice of GNF. Previous studies on bulk Ru have demonstrated that graphene layers grow epitaxially on the Ru (0001) surface.[131] Our DFT calculations, performed for Ru_{50} nanoclusters on graphene, clearly demonstrate that Ru atoms in the bottom layer bond firmly to the carbon atoms (dark green), as seen in structural changes before and after relaxation (Figure 5.8 E,F). This suggests that the graphitic lattice of GNF can, in principle, influence the symmetry and interatomic distances in the base layer of Ru island (Figure 5.8). Importantly, the second and third layers of atoms in Ru_{50} deviate significantly from the structure of the bottom layer (light green and yellow, respectively; Figure 5.8 F). While retaining the general structural features of the bulk Ru, the sub-2 nm nanoclusters appear to be significantly plastic due to a high fraction of surface atoms and strong bonding with carbon causing displacement of Ru atoms from hcp lattice positions both in the lateral and vertical directions. This explains the greater disorder in smaller nanoclusters observed in AC-STEM images.

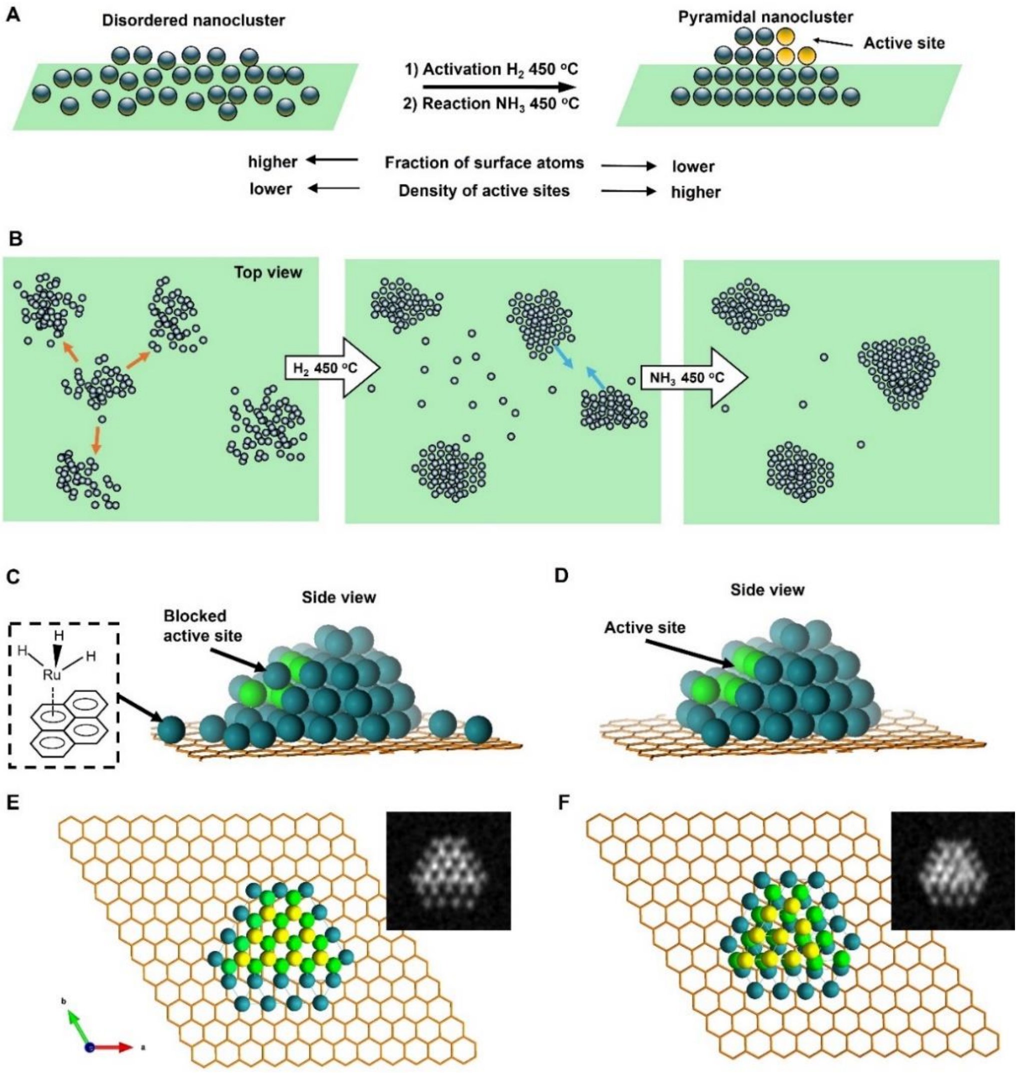

Figure 5.8. A schematic diagram illustrating changes in Ru nanoclusters in the activation step (H2, 450 °C) and during the reaction (NH3, 450 °C) (A). The nanocluster becomes more compact with the fraction of surface atoms decreasing and a truncated pyramidal shape clad with atomic steps evolving. Ostwald ripening (orange arrows) and coalescence of nanoclusters (blue arrows) are responsible for the pyramidalisation process, with the population of single Ru atoms increasing in the activation step followed by a decrease during the reaction (B). The state of the Ru nanocluster after activation in H2 (C). Most atoms are arranged in the lattice of a truncated pyramid, but there is a large number of single Ru atoms stabilised by hydride ligands and chemisorbed on the carbon surface (inset) and the surface of the pyramid, which blocks some active sites (atoms highlighted light green). During the reaction in ammonia, single Ru

atoms become integrated into atomic lattices of nanoclusters, with the edges and facets of the pyramids becoming more sharply defined, increasing the density of active sites (D). A structure of Ru50 nanocluster adsorbed on graphene before (E) and after (F) relaxation calculated by DFT. Ru atoms in the bottom layer (dark green) bind strongly to the carbon lattice while maintaining a distorted hexagonal arrangement, but Ru atoms in the second (light green) and third layers (yellow) adjust their positions more substantially during the relaxation to maximise metal-metal bonding. STEM images simulated from the DFT models are shown in the insets.

Our IL-STEM approach enables us to investigate the atomic mechanisms of nanocluster pyramidalisation by considering the evolution of each nanocluster within the context of its nearest neighbours (Figure 5.6). As the reactions occur at 450 °C, Ru atom exchange between nanoclusters and direct cluster-cluster interactions are both likely to occur. The Ru bonding energy with the carbon support can be estimated by that of Ru-graphene bonding of 188 kJ/mol,[132] but it is expected to be much higher at places of defects, such as a mono-vacancy (831 kJ/mol)[132] or step-edges of GNF. Therefore, the nanoscale landscape of the support would inevitably lead to the re-distribution of metal atoms on the surface once the temperature exceeds their surface diffusion barrier (Figure 5.8 B). Each area in IL-STEM can be split into several sub-areas where the structural evolution of a Ru nanocluster can be considered in conjunction with the evolution of its neighbours as they affect each other. For example, the area shown in Figure 5.6 a exhibits trackable nanoclusters. During the catalyst activation in H_2, three nanoclusters 1, 2 and 3 in the top-left corner moved and coalesced into a single nanocluster 4, and a nanocluster 12 on the right side disintegrated with three of its nearest neighbours, 11, 13 and 14, gaining atoms, such that the total number of nanoclusters in this area has reduced. An important feature of heating in H_2 is the explosion of the population of single atoms occupying the inter-cluster spaces (Figure 5.6, middle column). This correlates with the previous environmental STEM study of

Ru nanoparticles on graphitic and amorphous carbon that revealed a surprisingly large fraction of single atoms at 450 °C in an H_2:N_2 3:1 gas mixture at 1-20 Pa.[133] Returning to the same area after 3 hours of NH_3 decomposition catalysis reveals that 3 nanoclusters, 21, 22 and 23 have coalesce into a single clusters cluster 24. The number of single Ru atoms drastically decreased, and Ru nanoclusters became significantly more faceted, with sharp edges. The pattern of these transformations repeats from area to area, with the frequency of coalescence events seems to become more prevalent than Ostwald ripening under the reaction conditions (Figure 5.6).

The single atoms emerging under H_2 are likely produced due to the ruthenium hydride complex bonding strongly to the carbon support (Figure 5.8 C, inset), as Ru atoms stabilised with hydride ligands is known to form π-bonds effectively to aromatic molecules,[134,135] which in our case is served by the graphitic lattice of the GNF support. Under NH_3, the hydride complex breaks down, with most of the single Ru atoms returning to the nanoclusters, thus boosting their size and crystallinity, as evident from IL-STEM images. The fact that the growth of nanoclusters does not progress significantly beyond 4 nm^2 S_{FP} even after 12 hours of the reaction indicates a significant stabilising effect of the GNF surface, which limits the surface diffusion of metal atoms, hence leading to an equilibrium state with a narrow size distribution of metal nanoclusters.[102]

The role of the edges of the Ru hcp planes, particularly in a step-like arrangement, is extremely important in ammonia synthesis and decomposition reactions.[49,136-138] The strong binding energy of atomic nitrogen on Ru means that the rate-determining step in the ammonia decomposition reaction is the recombination of N atoms to N_2,[64,139] which takes place on so-called step active sites with favourable electronic and geometric properties for desorption.[140,141] The evolution of Ru on hexagonal boron nitride (hBN) driven by the epitaxial relationship between Ru hcp and hexagonal hBN lattices has recently been reported to cause the formation of ~10 nm hexagonal bifrustum nanoparticles, with long sharp edges providing a higher rate of hydrogen production from ammonia than more rounded nanoparticles.[103] In our case, the size of Ru nanoclusters is significantly smaller, in the region of 1.0-1.3 nm at the start of the process, such that a high fraction of Ru surface atoms is obtained in our nanoclusters. Importantly, our IL-STEM measurements allow monitoring the evolution of individual nanoclusters with atomic resolution, quantifying changes in their structure during catalyst activation and early stages of the reaction. This reveals the formation of truncated nano-pyramids clad with a series of atomic steps on every side (Figure 5.8 A). In light of IL-STEM analysis, both for individual nanocluster dynamics in isolation or coupled with the immediate neighbourhood, the answer to the question of what changes in Ru nanoclusters are responsible for the catalytic activity increase during the reaction's early stages becomes clearer. The overall trend is that the N_{at} and N_l of the nanoclusters increase while the S_{FP} decreases, which is correlated with the increase of the atomic order in the nanoclusters. As this process decreases the fraction of surface atoms, it should be expected to lead to lower catalytic activity. However, the atomic ordering process allows for crystal planes to be developed in nanoclusters, which are arranged in the form of a stepped structure. The stepped structure, developed from flattened disordered Ru nanoclusters during the reaction, is clearly visible in single-particle IL-STEM imaging and line profile analysis (Figure 5.5). As each step on the Ru nanocluster represents a potential active site, where the reaction proceeds several times faster than on the flat crystal plane or a disordered metal surface. This compensates for the decrease of the fraction of surface atoms, thus explaining the increasing activity of Ru/GNF catalyst during the reaction. Our DFT modelling revealed that the Ru nanoclusters on carbon exhibit significant plasticity (Figure 5.8 E, F). As a result, the exact atomic configuration in the active site of Ru/GNF may differ from the idealised models used for larger nanoparticles, which are based on bulk hcp Ru. Subtle sub-Angstrom displacements of Ru atoms within the nanocluster are difficult to discern experimentally, but they may have significant implications for the kinetics of catalysis.

We believe that the single Ru atoms on GNF play no role in catalysts, as their population drastically decreases as the catalyst becomes more active (Figure 5.4 D). Moreover, Ru atoms of surface of nanocluster which aren't in the lattice may be responsible for blocking Ru active sites at the early stage of the reaction (Figure 5.8 C), and therefore, as these atoms become incorporated in the crystal lattice of nanoclusters, accessibility of active sites improves, boosting the ammonia decomposition rate. The gradual evolution of the nanocluster's S_{FP} stabilising at around 2-4 nm^2 (ca. 1.6-2.3 nm in d) maximises the number of active sites per mass of Ru metal in the system, as an optimum size for this was predicted to be between 2-3 nm.[49] The stepped structures appear to persist over a long time, as shown by IL-STEM analysis for 12 hours of ammonia decomposition reaction (Figure 5.7). This means that the shapes that evolved during the catalyst activation in the early stages of the reaction are stable on the surface of graphitised carbon under the reaction conditions. This helps to explain the self-improving activity of Ru/GNF observed in our reaction kinetics measurements.

5.5. Conclusion

The high volumetric energy density of ammonia, compared to hydrogen and other zero-carbon technologies such as lithium batteries, gives it the potential to establish a new energy economy in the near future.[116,142] Ruthenium catalysis offers energy-efficient methods to break down ammonia into its elements, H_2 and N_2, on demand, at both small and large scales. In this work, we demonstrated that ruthenium atoms deposited directly onto the graphitic surface of GNF self-assemble into clusters with a S_{FP} of about 1 nm^2 and an irregular shape. The Ru/GNF material has shown high catalytic activity for the ammonia decomposition reaction, exceeding the activity of Ru on metal oxide supports under the same conditions, including Ru/CeO_2 regarded as one of the best catalysts. While Ru/metal oxide catalyst performance declined during the reaction, we demonstrate that the Ru/GNF catalyst increases its activity over 17 hours of the ammonia decomposition reaction. As the traditional electron microscopy analysis methods cannot explain this phenomenon, we employed the identical location aberration-corrected STEM imaging to follow the evolution of Ru nanoclusters through different stages of the reaction process to elucidate the origin of the increasing activity. Our data show that activation of the as-prepared Ru nanoclusters on GNFs at 450 °C in H_2 induces the ordering of Ru atoms within nanoclusters as well as the formation of a large fraction of single Ru atoms scattered across the graphitic support. The latter are unlikely to play any significant role increased catalytic activity of Ru/GNF, as they are only present in the very initial part of the reaction. Investigation of the evolution of individual, well-defined nanoclusters of Ru revealed that during the reaction the N_{at} and N_l mainly increased, thus reducing the fraction of surface Ru atoms. The quantitative AC-STEM image analysis in identical locations demonstrated the atomic ordering in the edges of the nanoclusters and the development of stepped structure, leading to the increased density of active sites, which more than compensates for the loss of surface area and boosts the catalytic activity of Ru/GNF measured. Furthermore, identical location AC-STEM analysis of groups of nanoclusters within the area of the nearest neighbourhood revealed that during the catalyst activation in H_2 both Ostwald ripening and coalescence are in action. However, the coalescence of nanoclusters is becoming the dominant underlying mechanism for the catalyst stepped structure formation under the reaction conditions, leading to its self-improved activity. Importantly, we demonstrated that GNFs stabilise the Ru stepped structure, not allowing them to grow beyond c.a. 4 nm^2 S_{FP}. This mechanism plays a crucial role in the enhanced activity and extended stability of the catalyst, opening a path for designing highly active and durable catalysts for ammonia decomposition reactions.

5.6. Summary and Further Discussion

This work was vital as a proof of identical location analysis in the study of nanoparticle evolution, both from the point of view of individual particle analysis and as proof that the data collected at single particle level are representative of the whole material when averaged. Effectively, IL-STEM can still produce ensemble average statistics whilst also providing a unique insight into the movement and morphological changes of individual clusters.

The technique used in this work had one drawback – the nanoparticles are not representative of a bulk catalyst as they were produced by flat deposition instead of bulk powder deposition. The method in this work involved drop-casting the GNF onto the TEM grid, then depositing the metal onto the material afterwards. This method allowed 3 things: 1) the cleanest possible surface of the GNF and Ru, 2) the removal of the "shadow-effect" due to the depositing direction being the same as the imaging direction, 3) very fine distribution and fine-tuning of the metal concentration. As a result of these 3 things, the samples produced in this manner were incredibly easy to image with little contamination, resulting in images with very high contrast between Ru and support. This allowed incredible resolution in the analysis of these samples, which is clearly seen in the finished paper.

Unfortunately, the downside of this technique is quite severe. As the material used in this study was not the same as that of the original catalyst, the conclusions drawn about the flat-deposited sample are not necessarily the same as those from the bulk sample. This was rectified in the paper by producing a catalyst by emulating the flat deposition on bulk GNF, which was then tested for catalytic activity.

From the point of view of understanding the bulk catalyst, this did not fix the issue and therefore in the continuation of this work, the catalyst was deposited in bulk first, then deposited onto the TEM grids – this will be seen in the next chapter.

6. A Catalyst that Ages like a Fine Wine

In this work, we continue the investigation of Ru/GNF – furthering the work done in the previous chapter. In this investigation, identical location microscopy was conducted using the bulk catalyst – giving data that is representative of the real catalyst material. This microscopy data is then correlated with activation energy measurements, a set of operando EXAFS data, *ex-situ* XPS data and some further catalytic investigations at different temperatures. All these data come together in this chapter to give a picture of the mechanism by which the catalyst self-improves and culminates with the potential discovery of a new mechanism for the decomposition of ammonia over Ru.

6.1. Introduction

Examples of catalysts self-improving under reaction conditions are scarce in the literature but there is one significant example. Kang *et al.* in 2023 reported a Ru/h-BN catalyst that self-improved under reaction conditions, leading them to pre-treat the catalyst for 12 hours prior to catalytic testing.[103] In this paper, the morphology of the nanoparticles was shown to have a large impact on the resultant catalyst, which increased from around 17.5% conversion at 0 hours to over 28% after 40 hours. During the first 12 hours, there was a significant decrease in activation energy from 97.4 to 83.0 kJ mol^{-1}. In this study led by Kang, the decrease in activation energy corresponds to the increase rate and they concluded that the morphology of the catalyst was the cause.

The aim of this chapter is to determine the mechanism by which Ru/GNF self-improves over the course of the reaction, with the aim to provide a framework for future catalyst design using this behaviour. This will be accomplished by:

1. Testing the catalyst for its activity in ammonia decomposition and measuring its activation energy at a number of time periods.
2. Imaging the catalyst by AC-STEM, then in identical location at different stages of the reaction in order to understand the morphological changes in the bulk catalyst.
3. Studying the catalyst by *operando* EXAFS and *ex-situ* XPS in order to understand the chemical changes happening in the catalyst over the course of the reaction.

Commonly in catalysis, characterisation is conducted for materials that are considered to be static. In some cases this is true, but most catalysts undergo transformation over the course of the reaction. This could be morphological, such as the ripening or sintering of nanoparticles, or electronic, such as the formation of a new active phase in the catalyst. In these cases, some degree of transient characterisation is required whereby the catalyst is compared across several time points of the reaction. Oftentimes, some combination of activation energy and electron microscopy before and after the reaction is adequate to understand the changes that the catalyst undergoes, but this is not always the case.

In this chapter, we present a case in which the simpler forms of transient characterisation fail to reveal the root of the transformation seen and more unique methods of characterisation were required.

6.2. Results

6.2.1. Catalyst Testing

The catalyst was tested for ammonia decomposition activity in a Hiden CATLAB Microreactor with an inline QGA mass spectrometer (please see experimental section for full details). The results are displayed in Figure 6.1.

The Ru/GNF catalyst displayed a high activity for ammonia decomposition and further, showed self-improvement – increasing in rate of H_2 production over the first 12 hours of reaction from 75 to 90 mmol min^{-1} g$_{Ru}$$^{-1}$.

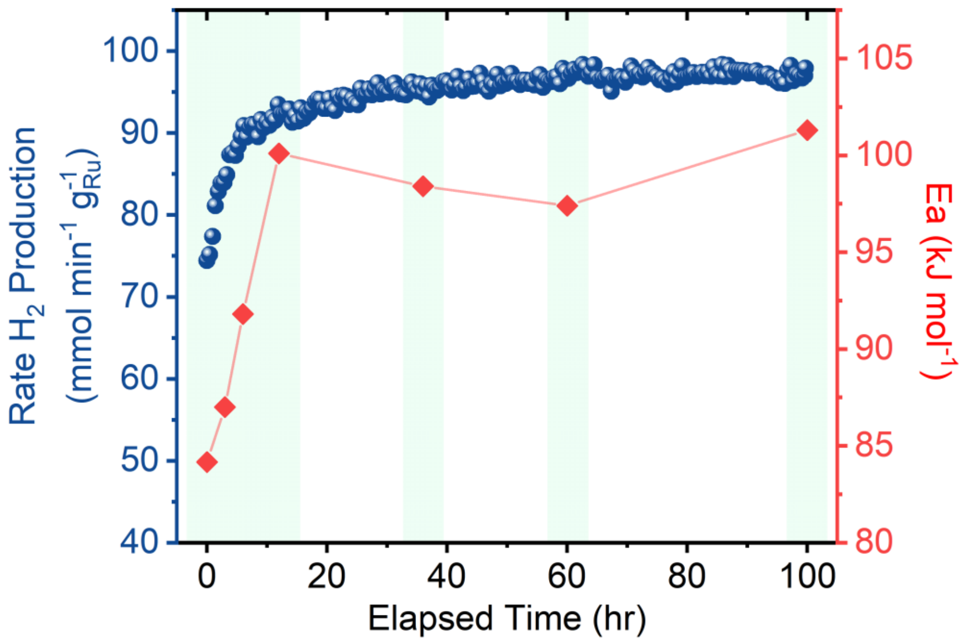

Figure 6.1. *a) The rate of hydrogen production from ammonia decomposition over Ru/GNF over 100 hours, plotted with the activation energy of the reaction measured at various time points.*

First, the activation energy of the Ru/GNF catalyst was tested at different time periods of the reaction. At the start of the reaction (immediately following the reduction step), the activation energy was measured at ~87 kJ mol^{-1} which decreased to ~85 kJ mol^{-1} after the first 12 hours of reaction. The activation energy then increased to ~93 kJ mol^{-1} after 60 hours, and finally to ~107 kJmol^{-1} after 100 hours. The initial measurements of 87 and 86 kJ mol^{-1} are in the range of typical E_a values for Ru/CNT or Ru/CNF catalysts, which tends to be reported as between 55 and 90 kJ mol^{-1}.{Lucentini, 2021 #85} After 100 h, the E_a of this catalyst lies far outside of expected values, which raises significant questions about the cause, especially when coupled with the gentle increase and plateau in rate. This large change in the activation energy is very characteristic of a change in mechanism or active site (or both).

If the activation energy of the catalyst gets higher, then the efficiency of each site reduced. Indeed, using the Arrhenius equation we can predict that an increase in Ea from 85 to 107 kJ mol^{-1} would result in a decrease in rate of ~40 times. Thus, the only way that the rate can increase despite the increase in activation energy is a vast increase in the number of sites. To this author's knowledge, this *in-situ* change in mechanism or active site has never before been reported for ammonia decomposition.

There are 2 potential changes to the catalyst that could help to explain this unique behaviour. First, a change in the morphology of the Ru nanoparticles. This is commonly seen during ammonia decomposition, whereby the particles agglomerate or change shape and can lead to altered binding of Ru to the NH_3 or intermediates. Secondly, a change in the electronic environment of the Ru particles. During the reaction, the surface morphology may change, N could be doped into the carbon support, or some other process could occur to change the bonding of Ru to C. These branches of explanation were explored in tandem by (in majority) microscopy and spectroscopy respectively.

6.2.2. Electron Microscopy

Aberration corrected – scanning transmission electron microscopy (AC-STEM) was conducted on the catalyst at the University of Birmingham using a JEOL JEM2100F aberration-corrected scanning transmission electron microscope (AC-STEM) equipped with a Cs probe corrector (CEOS) to study the changes of the morphology over the course of the reaction. Two methodologies were used in this work to study Ru/GNF; bulk microscopy (AC-STEM) and identical location microscopy (IL-AC-STEM). These are outlined in Figure 6.2.

It is common to use electron microscopy to study changes in the size of catalyst particles. This involves comparing micrographs of the catalyst before and after a reaction. Electron microscopy is a powerful tool that can measure changes with nanoscale precision at the single particle level. However, a heterogenous catalyst always has some degree of polydispersity, i.e. particles are non-identical. Therefore, structural information for individual catalytic particles is typically averaged in the distribution of sizes and shapes (here we refer to this method as bulk microscopy or ensemble averaging).

In bulk, the samples were imaged as-prepared, after-reduction (1 hour) and after reaction (24 hrs, 48 hrs, 70 hrs and 100 hrs). Typically, 2.5 mg of catalyst were placed into a quartz reactor tube, held in place by 2 plugs of quartz wool. The catalyst was placed into the reactor (Hiden CATLAB Microreactor) subjected to the following conditions:

- **As prepared.** This catalyst was imaged without any treatment.
- **After reduction.** The reactor was flushed with He gas for 30 mins (30 mL min^{-1}). The flow was then switched to 5% H_2 in Ar (25 mL min^{-1}) and the temperature was ramped to 450°C and held for 1 hour. The reactor was cooled to room temperature and then flushed with He (30 mL min^{-1}).
- **After reaction (X hours).** The reactor was flushed with He gas for 30 mins (30 mL min^{-1}). The flow was then switched to 5% H_2 in Ar (25 mL min^{-1}) and the temperature was ramped to 450°C (1°C min^{-1}) and held for 1 hour. The gas flow was switched to 5% NH_3 in Ar (25 mL min^{-1}) and conditions were held for X hours. The reactor was cooled to room temperature (1 °C min^{-1}) and then flushed with He (30 mL min^{-1}). X refers to the amount of time under reaction conditions.

The catalyst powder is then removed from the reactor, separated from the quartz wool mechanically, and then dropcast onto a lacey carbon 300-mesh Cu TEM grid (Agar Scientific). Typically when dropcasting, a very small quantity of catalyst powder in placed into a vial (<0.3 mg) and ~1 mL of propan-2-ol (HPLC grade) is added. The mixture is then sonicated until a suspension is produced of the catalyst in solvent. This suspension is then dropped onto the TEM grid (on a piece of filter paper). Once the solvent has evaporated, the process is repeated until the filter paper around the grid is visibly light grey in colour.

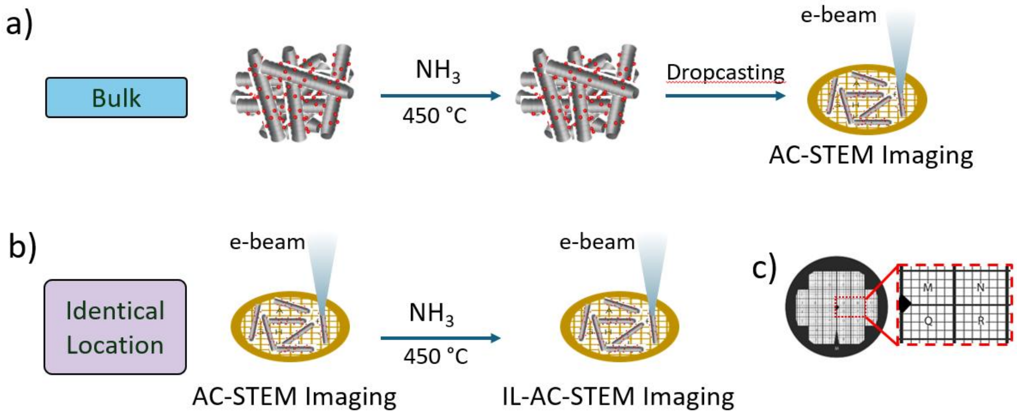

Figure 6.2. *A schematic showing the procedure for imaging Ru/GNF in bulk (a) and in identical location (b). The H7-finder grid used to conduct identical location microscopy is shown in image (c).*

The alternative to the ensemble averaging analysis is to image the same areas of the sample before and after each reaction stage. This provides a series of stop-frame images elucidating dynamics at the single-particle level. GNF supports, consisting of a highly conducting and chemically stable graphitic lattice, lend themselves to this approach very well due to their low TEM contrast and high electron beam stability. In addition, the TEM finder grid with alphanumerically labelled areas allows us to return to the same GNF and indeed the same set of nanoclusters before and after the reaction.

In the identical-location methodology, the as-prepared catalyst is dropcast onto a "lacey carbon on Au H7-finder grid" (Agar Scientific). The sample was sent for imaging before reaction, and the locations of each image was noted (based on the H7-finder grid reference regions) to keep track of them for the post-reaction imaging. Into the reactor tube was placed a quartz wool plug, and the grid was dropped into the tube to rest on top. The tube was then placed into the reactor and subjected to reaction conditions (please see Bulk, "after reaction X hours") for 12 hrs and 70 hrs respectively. The grids were then removed from the reactor and imaged at UoB in the same areas as before reaction.

6.2.2.1. Bulk AC-STEM

The catalyst was also imaged after various stages of the reaction – after reduction for 1 hour (AR), then after 24 hrs (A24), 48 hours (A48), 70 hours (A70), and 100 hours (A100) of reaction respectively. Each histogram contains the width of at least 200 particles. Representative images of Ru/GNF, Ru/GNF-AR and A24 can be seen in Figure 6.3, and those of Ru/GNF- A48, A70 and A100 can be seen in Figure 6.4. Size distribution analysis was conducted of each sample, measuring the diameter of the particle on its thinnest dimension, which is presented in Figure 6.3 and Figure 6.4 alongside the associated micrographs.

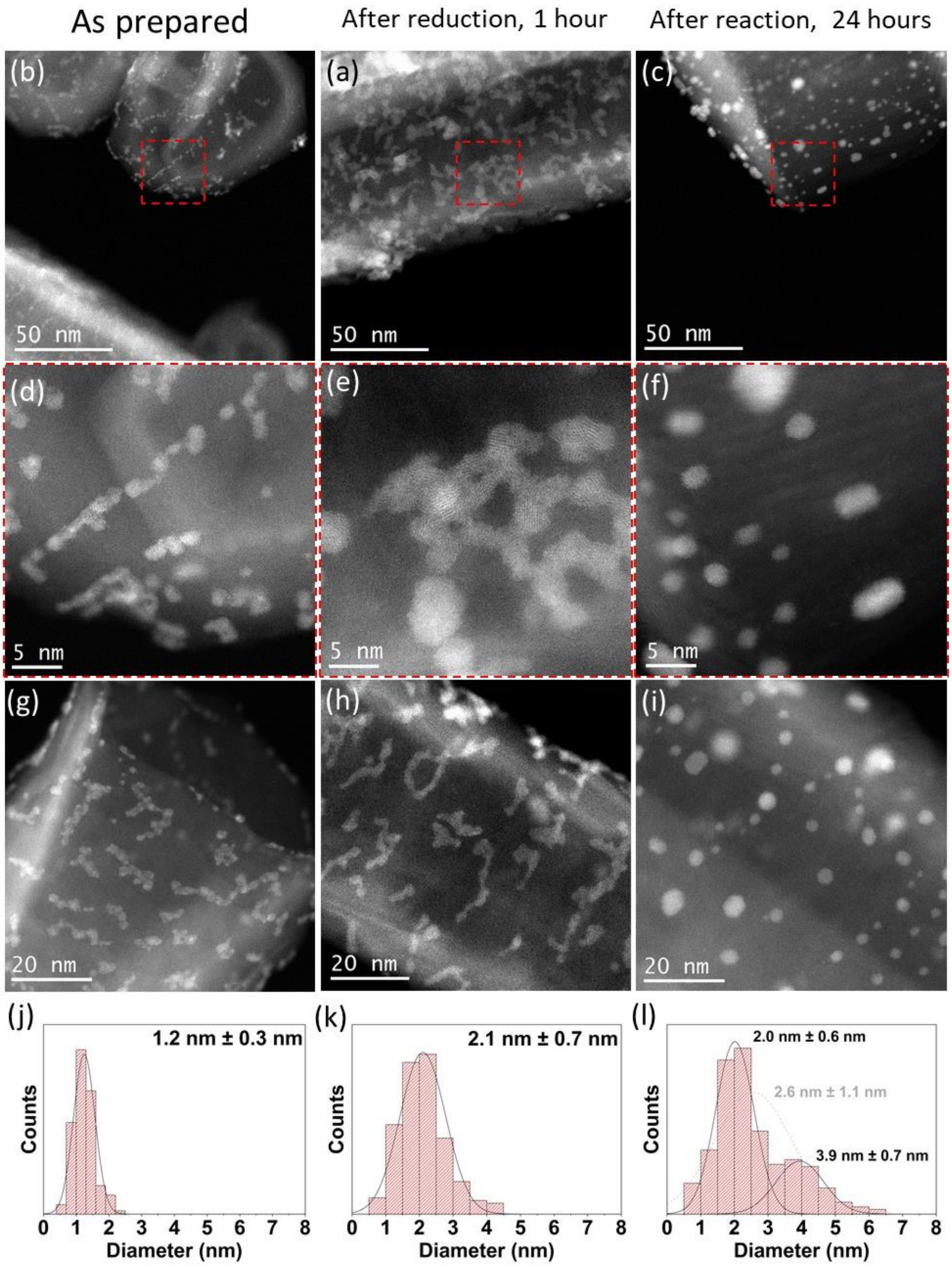

Figure 6.3. *AC-STEM micrographs and size distribution histograms of Ru/GNF after various stages of reaction. The images are of the catalyst as prepared (a, d, g, and j), after reduction for 1 hour (b, e, h, k) and after reaction for 24 hours (c, f, i, l).*

In Ru/GNF-AR, there is a significant increase in size as the particles begin to coalesce into larger amorphous clusters. This increase in size is expected for samples that are exposed to elevated temperature, and the ripening process has clearly begun in this sample. In terms of morphology, the flattened islands remain clear in their characteristic shape but begin to merge with the neighbouring clusters and become less distinct. The change in shape and size displays the low binding strength of Ru to C, allowing the metal atoms to move across the surface once kinetic energy is put into the system.

After 24 hours of NH3 decomposition, the ripening process has progressed and the nanoparticles became larger and more spherical in shape. These are more typical in shape and therefore, size distribution analysis can be conducted on this sample. Qualitatively, the particles in these images appear more much more crystalline than the semi-crystalline or amorphous particles in the after-reduction sample. In the size distribution histogram, there is also a bimodal distribution, but the cause of this is unclear. The 24-hour sample of Ru/GNF showed significant size distribution increase, and the morphology of the Ru particles changed from flat worms, to more spherical and crystalline.

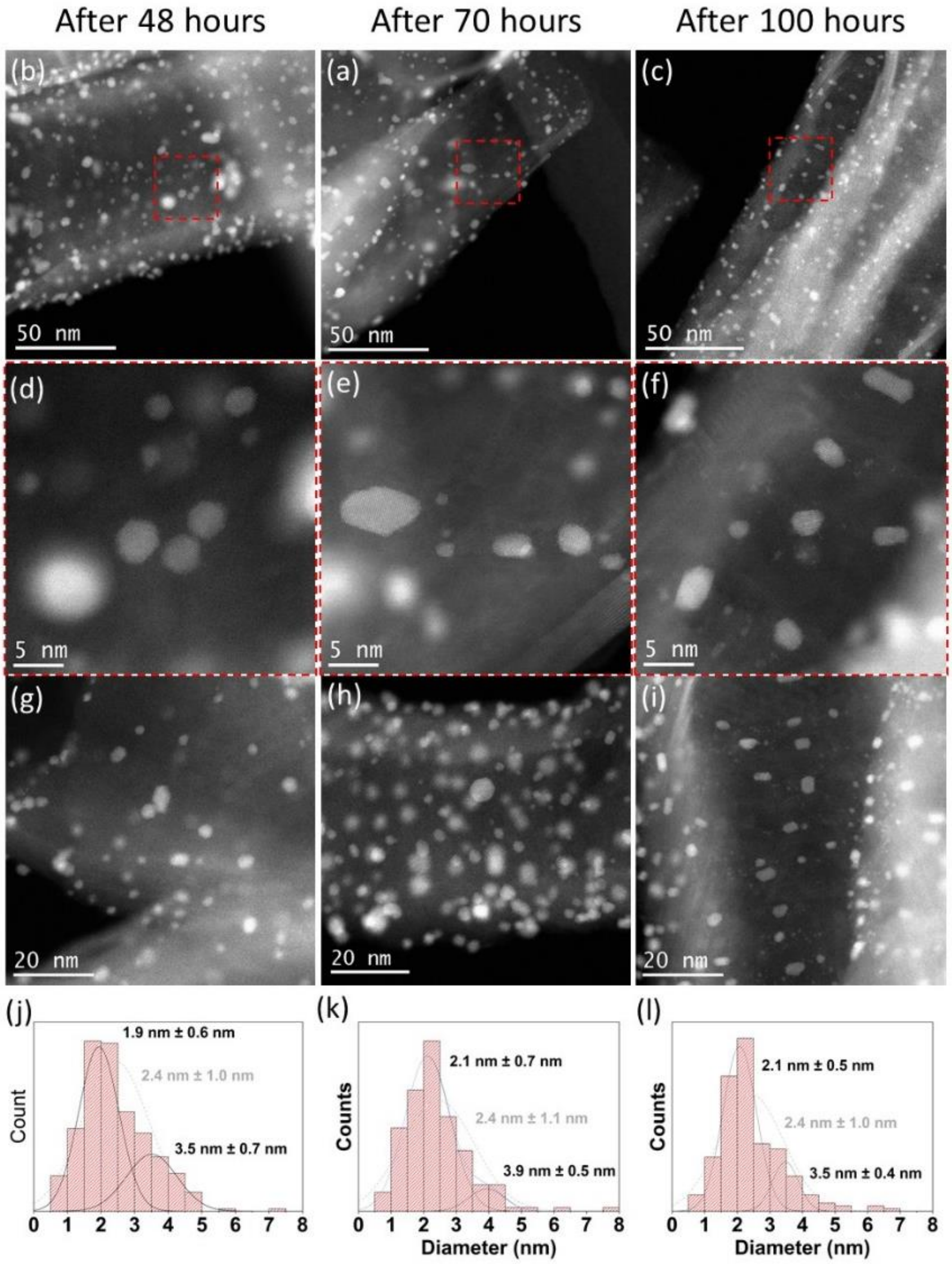

Figure 6.4. *AC-STEM micrographs of Ru/GNF after various stages of reaction. The images are of the catalyst after reaction for 48 hours (a, d, g, and j), after reaction for 70 hours (b, e, h, k) and after reaction for 100 hours (c, f, i, l).*

After 48 hours of reaction, there is very little change to the size distribution of the nanoparticles, with the histogram remaining identical (within error). This indicates that the particles have already reached a stable size by 24 hours.

After 70 hours and 100 hours of the reaction, the size distributions remain constant, indicating that once they have undergone the initial rearrangement at the beginning of the reaction, they remain very stable. Qualitatively, the particles also remain identical to those of the 24 hr sample and 48 hr sample.

Overall, the bulk microscopy analysis shows a gradual increase in size distribution until 24 hours, where the size remains constant (within error). Qualitative analysis of the images shows that crystallinity of the nanoparticles increases and that they become more spherical in shape throughout the course of the reaction, but this change mainly occurs in the first 24 hours of the reaction.

Typically in heterogeneous catalysis, a larger size distribution indicates a loss of active sites in the catalyst due to a decreased surface area to volume ratio, but in this system this does not occur. It is widely accepted in ammonia decomposition catalysts that the most active site is a B5-site (please see introduction). It has been shown that although increasing the size of nanoparticles decreases the overall surface area, it can also result in an increase in B5 sites. The optimum size for these has been reported to be between 1.8–2.5 nm in diameter,[68] which is consistent with the mean diameter of Ru/GNF from 24 hrs onwards.

The initial rearrangement of nanoparticles at the start of the reaction clearly correlates to the large initial increase in rate and is therefore concluded to be a key factor. That being said, the productivity of the catalyst continues to increase (albeit at a slower rate) after 24 hrs but the size of the nanoparticles remains identical. Therefore, there are clearly further processes in Ru/GNF that contribute towards the increase that are as yet not described.

In terms of activation energy, the initial dip from 87 to 85 kJ mol^{-1} correlates well with the increase in size of the nanoparticles at early times, attributed to the increase in the number of B5 sites. After longer time periods however, the bulk microscopy displays little to no change in the Ru nanoparticles.

Analysis of the bulk microscopy begins to explain initial trends in the activity of Ru/GNF for ammonia cracking. However, the trends in both rate and activation energy cannot be explained purely from size distribution analysis or qualitative analysis of the Ru nanoparticles.

6.2.2.2. Identical Location AC-STEM

Bulk analysis of the nanoparticles can only reveal so much information, but analysis of individual nanoparticles throughout the reaction can reveal things that were previously inaccessible.

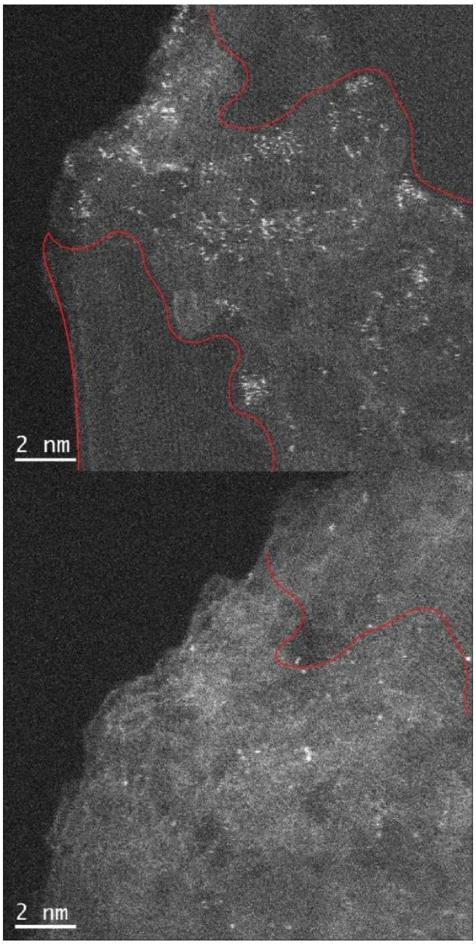

Figure 6.5. Identical location AC-STEM micrographs of Ru/GNF region 1. The previously pristine GNF surface decorated with Ru single atoms has been covered with a shifting of amorphous carbon that scatters the Ru single atoms.

In identical location, studying the low-loading areas (Ru-GNF1) shows that the previously clean and sparsely decorated regions become covered in a shifting of amorphous carbon that distributes the single atoms all over the surface of the GNF. In Figure 6.5 (a), the previously pristine regions highlighted in red help to give an impression of the change. As these single atom regions do not contribute to the catalysis, we will ignore these areas with respect to further electron microscopy analysis. After catalysis, the more highly loaded regions give rise to wider Ru particles that shorten and become more spherical in shape.

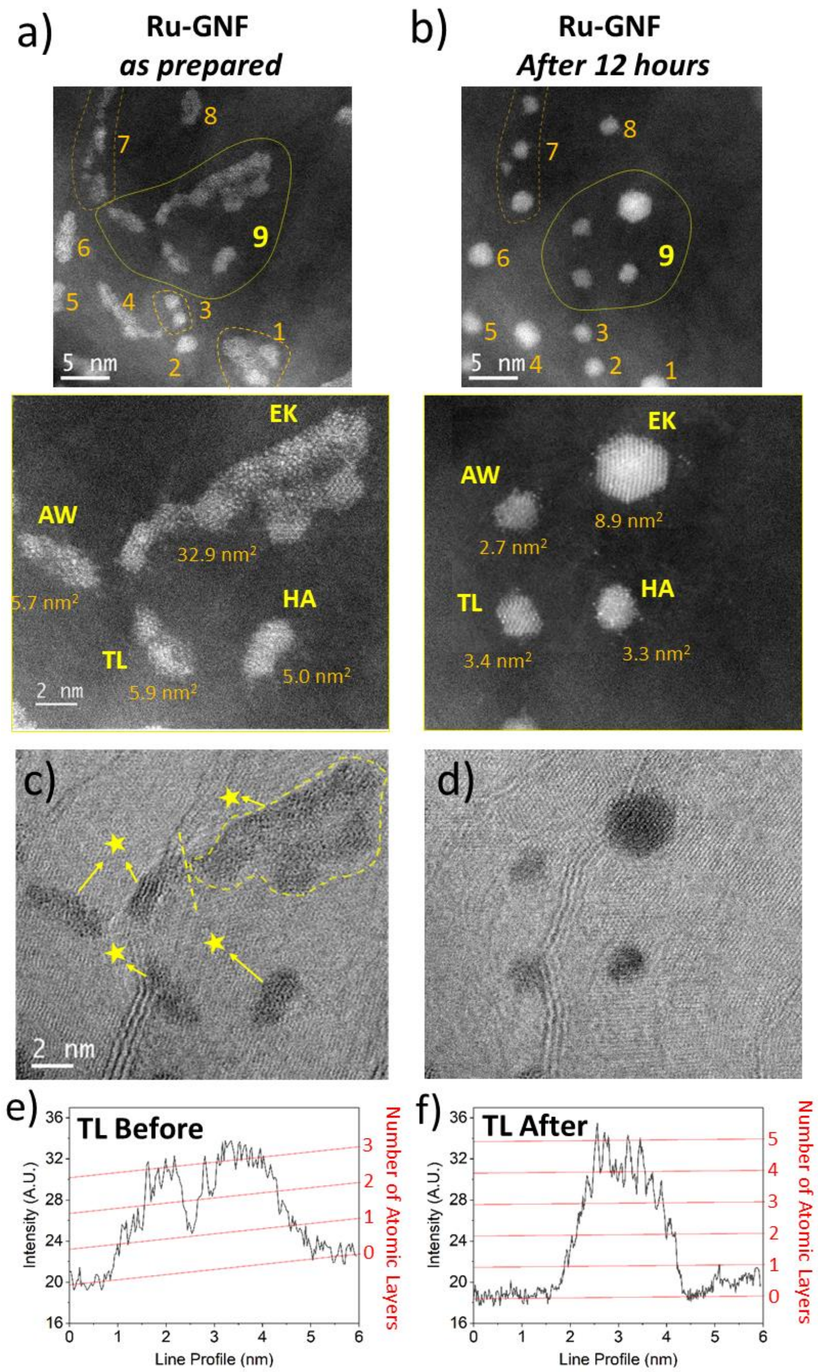

Figure 6.6. *AC-STEM images of Ru before and after 12 hours of catalysis from the same location (a, b). The cluster groups are labelled 1-9 before and after to follow the evolution. A family of 4 clusters in location 9 are highlighted for study. Bright field images (c) and (d) show the position of the particles relative to the carbon environment and illustrate migration across the surface. (E) and (f) show an example of line profile of TL clusters as prepared and after 12 hours of catalysis, respectively, to determine the number of layers of each cluster.*

In Figure 6.6 (a) and (b), we study a family of 4 clusters of Ru atoms before and after 12 hrs of reaction. In the as-prepared image we see very typical flat, amorphous, microcrystalline particles. As the Ru atoms are deposited onto the surface, the low energy barrier for Ru migration on the graphitic surface causes them to clump around stabilisation sites. These sites can be vacancy defects, step edges etc. These particles are the result of multiple smaller particles stuck together side-by-side as the Ru was deposited on the surface.

Figure 6.6. (a) and (b) illustrate the evolution of the clusters before and after reaction. After 12 hours of reaction, the particles become more uniformly crystalline, and in each case the footprint of the particle on the surface decreases. This decrease in projected area is also accompanied by a significant increase in the number of layers in each particle as they become more 3 dimensional. Figure 6.6 (e,f) shows a line-profile through the centre of the nanoparticle TL before an after reaction. The number of atomic layers is seen to increase from 3 to 5 after 12 hours of reaction.

Bright field images (c) and (d) better display the local carbon environment, highlighting the presence of step edges near this family of particles. As seen in Figure 6.6 (c), particles EK and TL both migrate towards a step edge, whereas AW migrates across the surface, and coalesces with the tail of EK. This indicates the presence of some other stabilisation site on the C surface that is not visible in electron microscopy, such as a vacancy defect or a doped pyridinic N atom.

Analysis of the carbon environment of the clusters in this way provides useful insight into the role of the GNF support in preventing sintering of Ru into large, inactive nanoparticles. In this case, both step edges and defects in the graphitic lattice play a significant role in anchoring the nanoparticles.

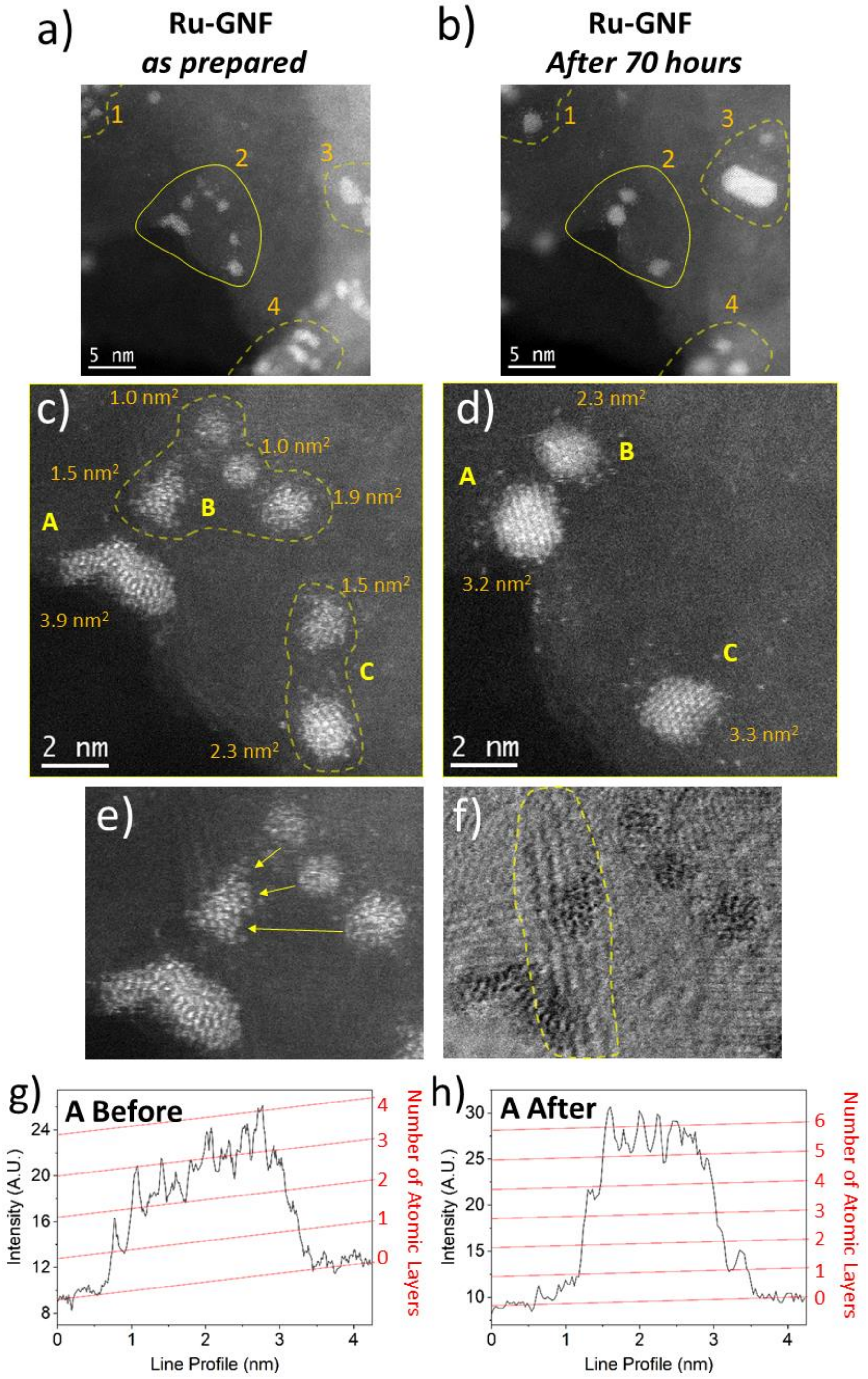

Figure 6.7. *AC-STEM images of Ru before and after 70 hours of catalysis from the same location (a, b). The cluster groups are labelled 1-4 before and after to follow the evolution. A family of clusters in location 2 are highlighted for study (c,d). Images (c) and (d) show the position of the particles relative to the carbon environment. (E) and (f) show an example of line profile of cluster A as prepared and after 70 hours of catalysis, respectively, to determine the number of layers of each cluster.*

The family of clusters in Figure 6.7 (a) in the as-prepared sample are a set of clusters that formed far enough apart (or near enough to stabilisation sites) that they remain distinct. Prior to reaction they are amorphous and somewhat diffuse – with an indistinct border of single atoms around their perimeter. After the reaction the crystallinity clearly increases.

Particle A remains in the same location but decreases in area and becomes taller. Group B undergoes an unusual change, highlighted in Figure 6.7 (c), whereby B1 remains in the same location, and B2-4 migrate and coalesce with B1. The bright field in (d) shows the reason for this behaviour – the existence of a step edge underneath B1 that acts to stabilise the cluster. The stabilisation provided by this step edge is also evidenced by the proximity of A and B after reaction. The binding of A and B to the step edge is strong enough to prevent these particles from coalescing together, despite their proximity. The evolution of particles in this region clearly evidences the role that step edges play to stabilise Ru particles against agglomeration.

AC-STEM analysis shows an initial change in the morphology of the Ru nanoparticles from flat worm-like islands of Ru to more spherical, rounded nanoparticles around 2.4 nm in diameter. The particles also increase in crystallinity significantly during this process, becoming more faceted and uniform in shape.

It has been shown that the most active site for ammonia decomposition, the B5 site, requires very precise geometry. The amorphous morphology of the nanoparticles before reaction results in a small number of these sites. As the particles become more crystalline the number of B5 sites naturally increases, increasing rate. Further, the increase in the number of layers in the nanoparticles results in a greater number of step edges on the Ru surface, giving rise to an increase in B5 sites.

More detailed analysis of the identical location AC-STEM reveals the reason behind the high stability of the catalyst with respect to sintering; the step-edges of GNF. Under reaction conditions, the particles migrate further across the surface until they reach a stabilisation site, such as a step edge, whereby they remain anchored and cease to agglomerate.

Although we have gained insight into the increase in rate through the formation of B5 sites, the increase in activation energy or longer-term increase in rate are not explained by any of these changes of the Ru nanoparticles. To explain these observations, we must instead turn to spectroscopy.

6.2.3. X-Ray Spectroscopy

Although AC-STEM has provided useful insight into the formation of active sites at the beginning stages of the reaction, there are clearly further processes at play that affect the activity of this catalyst.

To understand the changes to the electronic environment of the catalyst and binding of the Ru, *in-operando* Extreme X-ray Absorption Fine Structure (EXAFS) and *ex-situ* X-ray Photoelectron Spectroscopy (XPS) were conducted of the catalyst, which will be described in this section.

6.2.3.1. In-operando EXAFS

In-operando EXAFS was conducted of Ru/GNF at diamond light source in Harwell, Oxfordshire. The sample was placed into a quartz tube in between plugs of quartz wool, as shown in Figure 6.8.

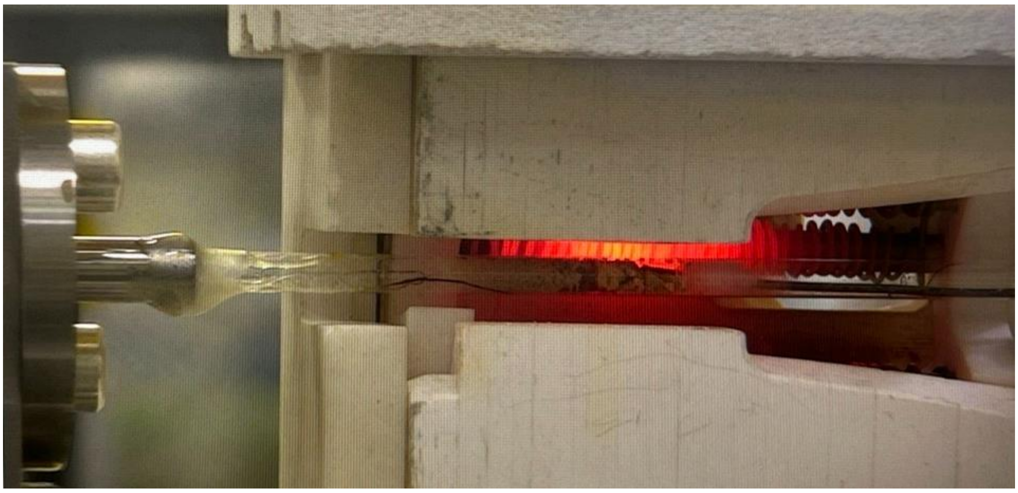

Figure 6.8. *A picture of the experimental set-up for conducting operando EXAFS at Diamond Light Source. The sample is inside a quartz tube, and pictured next to the heating element.*

The temperature of the reactor was monitored by a thermocouple (pictured on the right of Figure 6.8), and gas was flowed through the tube continuously during the measurement.

The experimental procedure can be seen in Figure 6.9, with EXAFS taken after each of the following steps (after 30 mins of time at each stage to equilibrate).

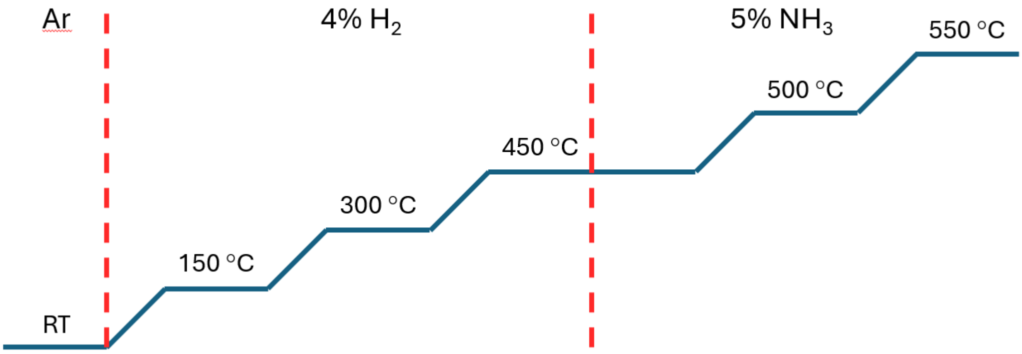

Figure 6.9. *A schematic diagram of the operando EXAFS experiment, displaying temperature and gas flow of each measurement.*

EXAFS data was processed using the Artemis software package, where plots were extracted of radial distance (R) against the intensity χ(R). This method of displaying EXAFS data allows us to understand the distribution of Ru-X bond distances present in the sample in “R-space”. These spectra are plotted in Figure 6.10, labelled with the associated conditions of the reaction (temperature and gas composition).

There are 2 significant bond distances present in Figure 6.10, 1.5 Å and 2.4 Å. Peaks at 1.5 Å are Ru-C (often seen in Ru single atoms) or Ru-N peaks, but it is difficult to state for certain which is present based solely on the R value. This must instead by done by a process of trial-and-error fitting, based on crystal structures of the associated species. Fitting values are then evaluated of Ru-N and Ru-C to evaluate the most likely fit for the peak. Further analytical techniques can also be considered in the peak assignment. Peaks at 2.4 Å are Ru-Ru (crystalline Ru) as evidenced by their dominant presence in the Ru foil spectrum.

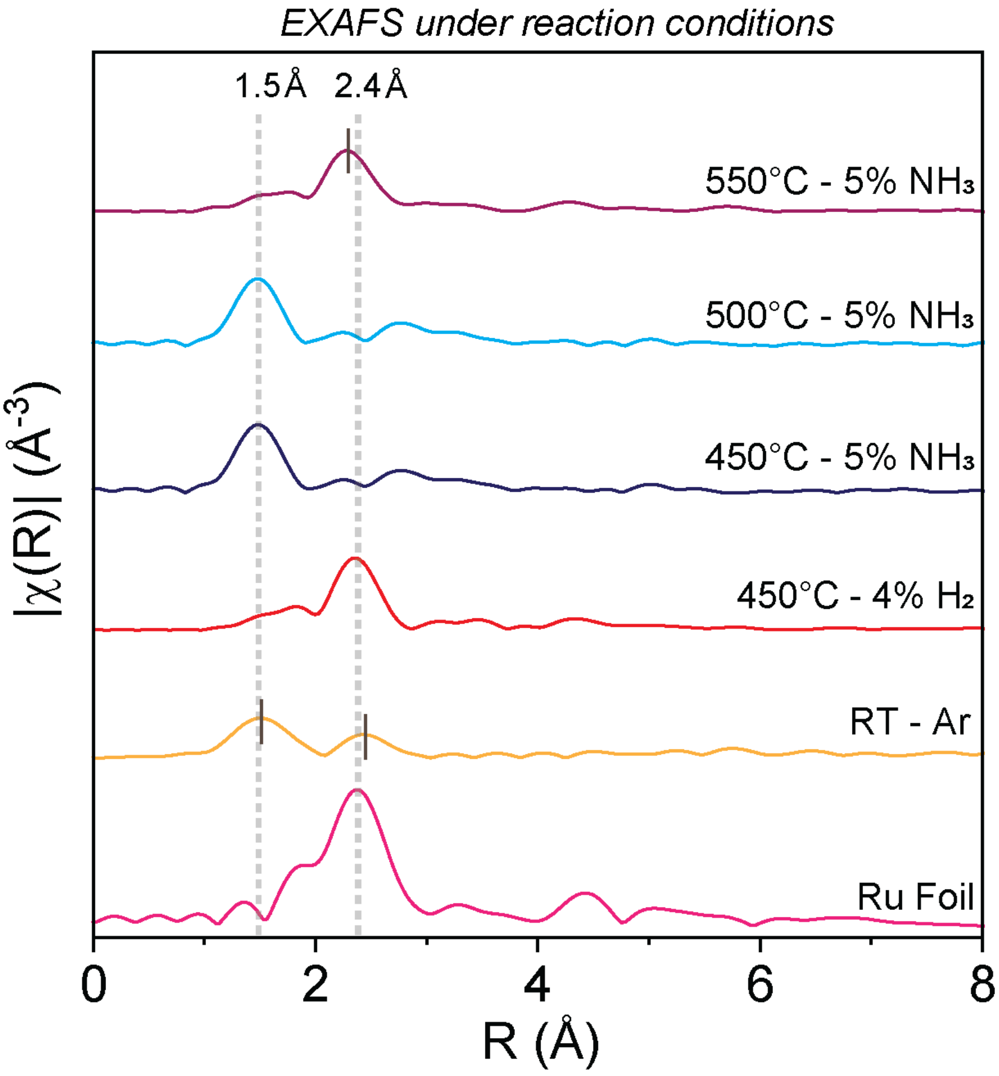

Figure 6.10. *EXAFS plots showing Ru bond distances (x-axis) and intensity (y-axis). Each plot signifies the sample under different stages of the experiment, as it was exposed to different conditions.*

At room temperature under a flow of argon gas, Ru/GNF displays peaks 1.5 Å and 2.4 Å. The 1.5 Å peak in this measurement is indicative of Ru-C bonding, which corresponds well to the microscopy of the as-prepared sample, which shows flat islands of Ru across the surface of the GNF support. These make up most of the Ru bonds, but the peak at 2.4 Å shows the presence of crystalline Ru in the core of the nanoclusters.

When the gas flow is changed to 4% H_2 and the catalyst is heated to 150, 300, and 450 °C, the Ru-C peak almost entirely disappears, and the Ru-Ru peak becomes dominant. This again matches the microscopy well, as the images of the after-reduction sample showed an increase in the size of the nanoclusters, which results in more crystalline Ru.

When the flow was switched to 5% NH_3, the Ru-Ru peak completely disappeared and was replaced by a new peak at 1.5 Å. Consideration of fitting parameters showed that this peak was most likely Ru-N, which matched well with imaging of the sample after reduction, as it showed a very low concentration of single atoms and a large increase in height of the nanoparticles. Ru-N bonds in this case suggest that the Ru nanoparticles undergo bulk nitridation whilst in reaction conditions, to the point that there is no crystalline Ru remaining.

The Ru-N peak in EXAFS in NH_3 atmosphere can be rationalised, as the rate determining step of NH_3 cracking of Ru is N_2 desorption, leading to a high concentration of surface N*. However, N* species would be expected to only be present on the surface of the particle, not throughout the entirety. To the author's knowledge, this behaviour has never been reported.

At 500 °C the sample remains identical to 450 °C, but upon heating to 550 °C the sample undergoes another change. At 550 °C, the Ru-N peak is vastly reduced and the Ru-Ru peak at 2.4 Å is reformed, suggesting that the RuN nanoparticles are metastable until 550 °C, whereby they undergo a sintering process and deactivate, leading to the peak at 2.4 Å, metallic Ru.

6.2.3.2. *X-Ray Photoelectron Spectroscopy*

Ex-situ x-ray photoelectron spectroscopy (XPS) was conducted of Ru/GNF as prepared, and then after 8 hour of reaction at 450 °C, 475 °C, and 500 °C. The N 1s spectra can be seen in Figure 6.11. The data were charge referenced against the adventitious carbon peak at a binding energy of 284.8 eV.

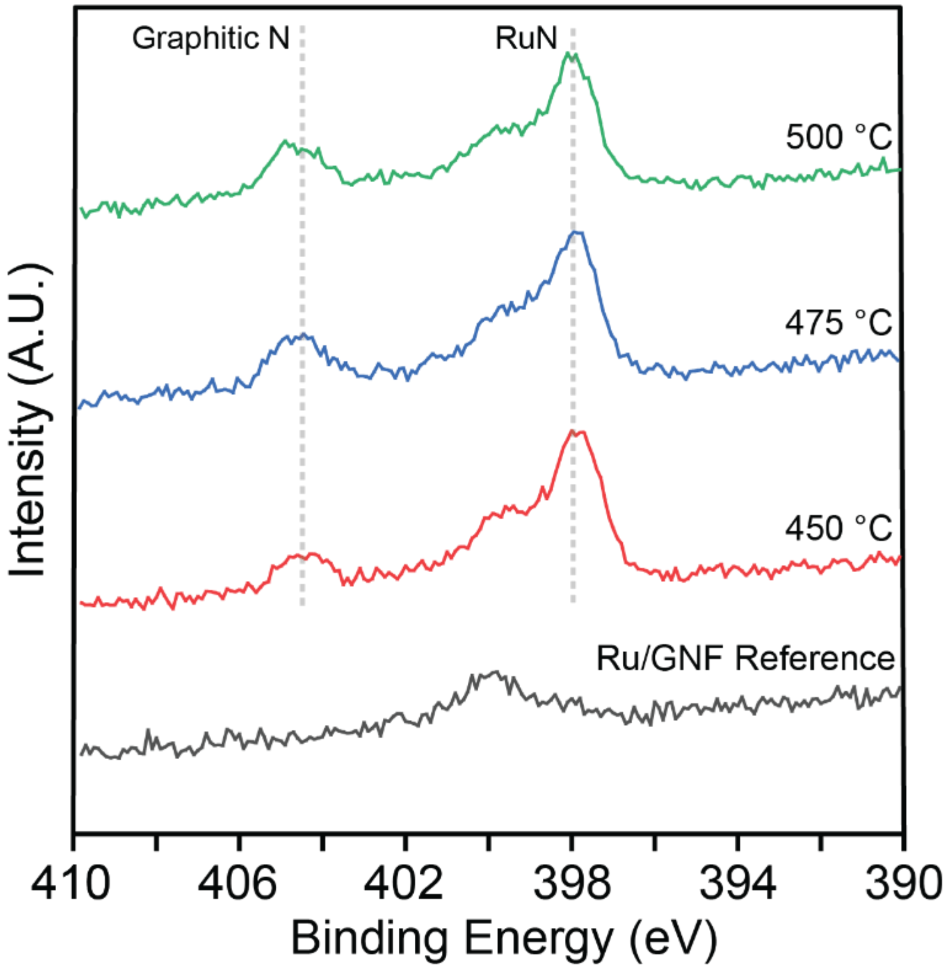

Figure 6.11. *N1s XP spectra of Ru/GNF as-prepared (grey), and after reaction for 8 hours at 450 °C (red), 475 °C (blue) and 500 °C (green).*

XPS is used to analyse the electronic environment of a particular element in the material. By studying the N 1s spectra, we can understand where in the structure N in present (what electronic environments it inhabits). In the Ru/GNF reference spectrum, a small peak can be seen at ~400 eV, which is attributed to a small concentration of pyrrolic N in Ru/GNF. In all cases after reaction, 2 new peaks grow at ~398.5 eV and ~404 eV, which are independent of temperature. The peak at 404 eV can be attributed to pyridinic oxide, which indicates the presence of pyridinic N atoms in Ru/GNF after reaction that, when exposed to air, oxidise. The peak at 398.5 eV has been reported to be pyridinic N but has also been reported to be a metal nitride species. In this case, based on EXAFS data it is very likely that both pyridinic N and RuN are present in the sample.

The XPS spectra after reaction show strong evidence of in-situ N doping of the GNF support material. N-doping of carbon supports has been shown to have a "promoter-like" effect on the rate of the result Ru/C catalyst.[74] Nitrogen's higher electronegativity and its non-bonding lone pair make electron rich sites that can interact with the Ru nanoparticles. Replacement of C with N in the GNF also increases basicity of the support, which increases the electron donation into the Ru nanoparticles.

The increased electron donation to Ru results in a stabilisation of the N* surface nitride, which results in the N_2 dissociation becoming harder (hence the increase in E_a). However, the increased stability of RuN results in bulk nitridation of Ru. As Ru is nitride, a new mechanism can take place, which is illustrated in Figure 6.12.

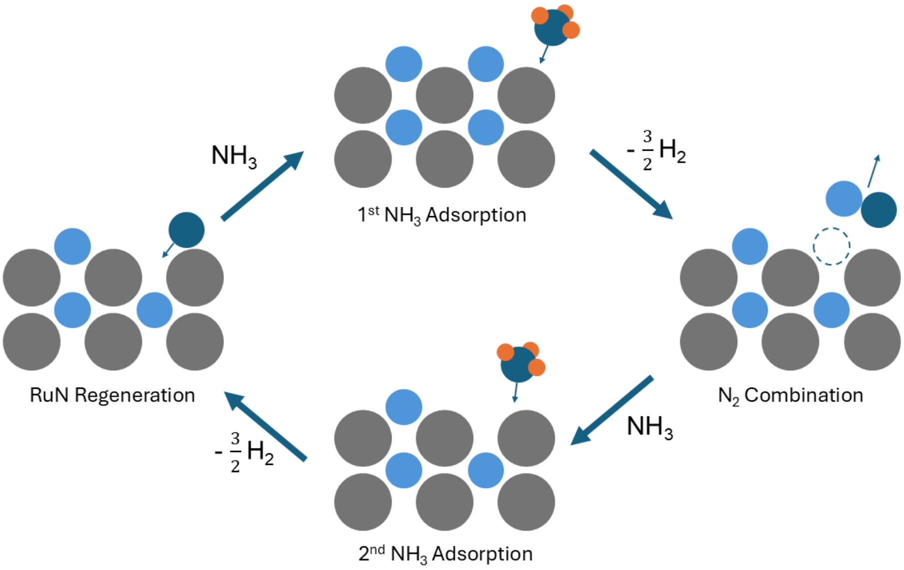

Figure 6.12. *A suggested mechanism for ammonia decomposition over a RuN catalyst produced in-situ.*

Firstly, ammonia adsorbs onto the surface of RuN and undergoes dehydrogenation. The N* surface nitride from the dehydrogenated ammonia recombines with a lattice N from RuN and desorbs, leaving a N vacancy in RuN. In the 2nd cycle, ammonia adsorbs, dehydrogenates, and then fills in the vacancies, regenerating the RuN.

Previously, the N_2 recombination was rate determining as it required 2 surface nitrides to meet at a B5 site to desorb. In this new mechanism, any lattice nitride on the surface can act to recombine with the surface nitride. In this way, only one surface nitride is required in the N recombination step. This massively increases in the number of active sites, which counteracts the increase in E_a and increases the overall rate.

Examples of catalysts self-improving under reaction conditions are scarce in the literature but there is one significant example. Kang *et al.* in 2023 reported a Ru/h-BN catalyst that self-improved under reaction conditions, leading them to pre-treat the catalyst for 12 hours prior to catalytic testing.[103] In this paper, the morphology of the nanoparticles was shown to have a large impact on the resultant catalyst, which increased from around 17.5% conversion at 0 hours to over 28% after 40 hours. During the first 12 hours, there was a significant decrease in activation energy from 97.4 to 83.0 kJ mol^{-1}.

In Kang *et al.* 2023, it was reported that a change in the morphology of the nanoparticles from flat to faceted hexagonal was responsible for this 60% increase in activity. Using the insights gained in this work, it seems plausible that localised in-situ nitrogen doping could have taken place in this h-BN catalyst too. In this case, the mechanism did not change but the increase in localised electron donation resulted in lower E_a and therefore an increase in rate. This change, coupled with the morphological change as described in this work may have had a synergistic effect, increasing the rate.

On a separate tangent, Bell *et al.* in 2017 reported on the N-doping of CNT supports.[74] In this paper, they produced a set of catalysts with various degrees of N doped into the carbon lattice via hydrothermal treatment with 2 different dopants – aqueous ammonia (NH_4OH), and cetyltrimethylammonium bromide (CTAB). It was shown that doping the CNTs with aqueous ammonia before deposition of Ru resulted in a markedly higher activity of the catalysts (42% higher), whilst also showing an increased activation energy. The size distribution histograms in this work also showed that there was no change (within error) to the size of the nanoparticles in the N-doped sample vs. the pure CNT catalyst.

This paper is a case whereby the change in mechanism that we reported in this work may occur (to a lesser degree), allowing an increase in rate where the activation energy would indicate otherwise.

Neither of these cases are categorical proofs of the conclusions of this work but do begin to suggest that this behaviour may have occurred in previous works. But to the difficulty of detection and complexity of the characterisation required, it has gone unnoticed.

6.3. Conclusion and Future Work

In this chapter, I have described the extensive characterisation and testing of Ru/GNF and built up a picture of the mechanism by which it self-improves. Firstly, although the rate of reaction increased during the first 12 hours of reaction, so too did the E_a. This effect is completely opposite to expectation, which was the first indication of a unique transformation.

Initial electron microscopy studies using ensemble averaging uncovered no such interesting effects. A 2nd study using identical location imaging revealed new information. Over the course of the reaction, clusters were seen to migrate to anchor positions along the step edges, where there are local high densities of electrons. This allowed the prevention of coalescence into large, inactive nanoparticles whilst the catalyst underwent a 2nd change.

In chapter 3, it was found that the first 24 hours of reaction are important for the self-improvement of the catalyst. Pre-treatment protocols involving direct exposure to ammonia at reaction temperature led to a more complete nitridation and thus faster self-improvement, while cooling or flushing steps before the reaction hindered the process, leading to reduced activity and incomplete transformation of the catalyst. There, I hypothesised that some chemical change such as nitridation of the Ru nanoparticles was the cause for the increase in rate.

In-operando EXAFS and ex-situ XPS confirmed that there was indeed nitridation of Ru and N-doping of the carbon support over the course of the reaction. These 2 observations helped to bring light to the overall mechanism of the catalysts' self-improvement – a change in reaction mechanism akin to Mars van Krevelen. Whilst the evidence for this specific mechanism is by no means conclusive, there is clear evidence that there is a significant shift in mechanism or active site in this catalyst. Either way, this work goes a long way towards the final understanding of this catalyst, which will help to guide future catalyst development to harness similar effects.

7. Overall Conclusions

In this thesis, I have explored the development of a novel ruthenium-based catalyst supported on graphitised nanofibres (Ru/GNF) for the low-temperature decomposition of ammonia. Firstly, I identified the key challenges in ammonia cracking, particularly the need for catalysts that are both highly active and stable under reaction conditions. Through a combination of catalyst synthesis, catalytic testing, advanced microscopy, and spectroscopy, this study has provided new insights into the behaviour of Ru catalysts on carbon supports. Importantly, I have demonstrated a rare and valuable phenomenon: catalyst self-improvement during operation.

The Ru/GNF catalyst was shown to increase in activity over time, a behaviour that was investigated in depth using identical location scanning transmission electron microscopy (IL-STEM). This technique allowed for the tracking of individual nanoclusters before and after reaction, revealing that the catalyst undergoes a transformation from flat, amorphous clusters to more crystalline, pyramidal structures with stepped edges. These morphological changes were found to correlate with an increase in the number of active B5 sites, which are known to be critical for ammonia decomposition. The step-edges of the GNF support played a key role in stabilising the Ru nanoclusters, preventing excessive sintering and maintaining a high density of active sites.

Further investigation using in-operando EXAFS and ex-situ XPS has revealed that the self-improvement of the catalyst is not purely morphological but also involves a chemical transformation. The Ru nanoparticles were found to undergo bulk nitridation during the reaction, forming a RuN phase that is proposed to change the reaction mechanism. This transformation leads to an increase in the number of active sites and a shift in the rate-determining step, which helps to explain the observed increase in activity despite a rise in activation energy. These findings suggest that the Ru/GNF catalyst operates with dynamic mechanism that evolves under reaction conditions, offering a new perspective on catalyst design for ammonia decomposition. The insights gained from this work provide a strong foundation for the development of next-generation catalysts that are not only efficient but also capable of adapting and improving during use.

Following on from this thesis, the first point of focus should be to assess the application of Ru/GNF in a prototype ammonia cracker under realistic conditions. This would help to benchmark the catalyst and highlight any issues in scale-up, thermal management, or pressure drop due to particle size.

In terms of furthering the specifics of the hypothesis laid out in this thesis, I would recommend first starting with a isotopic labelling experiment. In this experiment, labelled NH_3 could be introduced after the self-improvement period and the mass of the resultant N_2 could be measured. If the measured mass has some $^{14}N^{15}N$, then it confirms that the lattice RuN nitrogen is involved in the reaction, giving firm evidence for the hypothesis.

Aside from these, an excellent point of focus would be to attempt to produce catalysts that mimic the self-improvement of this catalyst. These could be other RuC catalysts such as Ru on nitrogen-doped graphene or carbon nanohorns. An alternative pathway might be to investigate whether similar self-improving behaviour can be produced in more abundant metal catalysts like Ni or Co. This might involve alloying or some support engineering to mimic the structure and electronic environment in Ru/GNF.

8. Bibliography

1 Thomas, N. C. The role of hydrogen as a future fuel. *Science Progress (1933-)* **72**, 37-52 (1988).

2 Winsche, W. E., Hoffman, K. C. & Salzano, F. J. Hydrogen: Its Future Role in the Nation's Energy Economy. *Science* **180**, 1325-1332, doi:10.1126/science.180.4093.1325 (1973).

3 Bockris, J. O. M. The hydrogen economy: Its history. *International Journal of Hydrogen Energy* **38**, 2579-2588, doi:https://doi.org/10.1016/j.ijhydene.2012.12.026 (2013).

4 Staffell, I. *et al.* The role of hydrogen and fuel cells in the global energy system. *Energy & Environmental Science* **12**, 463-491, doi:10.1039/C8EE01157E (2019).

5 Muradov, N. in *Compendium of Hydrogen Energy* (eds Velu Subramani, Angelo Basile, & T. Nejat Veziroğlu) 489-522 (Woodhead Publishing, 2015).

6 Ursua, A., Gandia, L. M. & Sanchis, P. Hydrogen Production From Water Electrolysis: Current Status and Future Trends. *Proceedings of the IEEE* **100**, 410-426, doi:10.1109/JPROC.2011.2156750 (2012).

7 Agency, I. R. E. Hydrogen: A renewable energy perspective. *IRENA* (2019).

8 Lucentini, I., Garcia, X., Vendrell, X. & Llorca, J. Review of the Decomposition of Ammonia to Generate Hydrogen. *Industrial & Engineering Chemistry Research* **60**, 18560-18611, doi:10.1021/acs.iecr.1c00843 (2021).

9 Robertson, I. M. *et al.* Hydrogen Embrittlement Understood. *Metallurgical and Materials Transactions A* **46**, 2323-2341, doi:10.1007/s11661-015-2836-1 (2015).

10 Züttel, A. Hydrogen storage methods. *Naturwissenschaften* **91**, 157-172, doi:10.1007/s00114-004-0516-x (2004).

11 Nijkamp, M. G., Raaymakers, J. E. M. J., van Dillen, A. J. & de Jong, K. P. Hydrogen storage using physisorption – materials demands. *Applied Physics A* **72**, 619-623, doi:10.1007/s003390100847 (2001).

12 Eberle, U., Felderhoff, M. & Schüth, F. Chemical and Physical Solutions for Hydrogen Storage. *Angewandte Chemie International Edition* **48**, 6608-6630, doi:https://doi.org/10.1002/anie.200806293 (2009).

13 Klerke, A., Christensen, C. H., Nørskov, J. K. & Vegge, T. Ammonia for hydrogen storage: challenges and opportunities. *Journal of Materials Chemistry* **18**, 2304-2310, doi:10.1039/B720020J (2008).

14 Zamfirescu, C. & Dincer, I. Using ammonia as a sustainable fuel. *Journal of Power Sources* **185**, 459-465, doi:https://doi.org/10.1016/j.jpowsour.2008.02.097 (2008).

15 Choudhary, T. V., Sivadinarayana, C. & Goodman, D. W. Catalytic ammonia decomposition: COx-free hydrogen production for fuel

cell applications. *Catalysis Letters* **72**, 197-201, doi:10.1023/A:1009023825549 (2001).

16 Papavinasam, S. in *Corrosion Control in the Oil and Gas Industry* (ed Sankara Papavinasam) 41-131 (Gulf Professional Publishing, 2014).

17 Aziz, M., Wijayanta, A. T. & Nandiyanto, A. B. D. Ammonia as Effective Hydrogen Storage: A Review on Production, Storage and Utilization. *Energies* **13**, 3062 (2020).

18 Dincer, I., Rosen, M. A. & Al-Zareer, M. in *Comprehensive Energy Systems* (ed Ibrahim Dincer) 470-520 (Elsevier, 2018).

19 Ober, J. A. Mineral commodity summaries 2018. 204 (Reston, VA, 2018).

20 Schüth, F., Palkovits, R., Schlögl, R. & Su, D. S. Ammonia as a possible element in an energy infrastructure: catalysts for ammonia decomposition. *Energy & Environmental Science* **5**, 6278-6289, doi:10.1039/C2EE02865D (2012).

21 Parks, G. T. a. G. (ed U.S. Department of Energy) (2006).

22 Erdemir, D. & Dincer, I. A perspective on the use of ammonia as a clean fuel: Challenges and solutions. *International Journal of Energy Research* **45**, 4827-4834, doi:https://doi.org/10.1002/er.6232 (2021).

23 Andersson, J. & Grönkvist, S. Large-scale storage of hydrogen. *International Journal of Hydrogen Energy* **44**, 11901-11919, doi:https://doi.org/10.1016/j.ijhydene.2019.03.063 (2019).

24 Nkosi, B. *et al.* Hydrochlorination of acetylene using gold catalysts: A study of catalyst deactivation. *Journal of Catalysis* **128**, 366-377, doi:https://doi.org/10.1016/0021-9517(91)90295-F (1991).

25 Kirkpatrick, W. H., Seale, Virgil L . Dewatering or demulsification of hydrocarbon oils with chemical means. US patent (1960).

26 Thomas, C. L. & Barmby, D. S. The chemistry of catalytic cracking with molecular sieve catalysts. *Journal of Catalysis* **12**, 341-346, doi:https://doi.org/10.1016/0021-9517(68)90118-8 (1968).

27 Lloyd, L. *Handbook of Industrial Catalysts*. (Springer US, 2011).

28 Roduner, E. Understanding catalysis. *Chemical Society Reviews* **43**, 8226-8239, doi:10.1039/C4CS00210E (2014).

29 Laidler, K. J. A glossary of terms used in chemical kinetics, including reaction dynamics (IUPAC Recommendations 1996). *Pure and Applied Chemistry* **68**, 149-192, doi:doi:10.1351/pac199668010149 (1996).

30 Parlett, C. M. A., Wilson, K. & Lee, A. F. Hierarchical porous materials: catalytic applications. *Chemical Society Reviews* **42**, 3876-3893, doi:10.1039/C2CS35378D (2013).

31 Dumesic, J. A., Huber, G. W. & Boudart, M. in *Handbook of Heterogeneous Catalysis*.

32 Williams, M., Minjares, R. A TECHNICAL SUMMARY OF EURO 6/VI VEHICLE EMISSION STANDARDS. *ICCT* (2016).

33 Ross, K., Chmiel, J. F. & Ferkol, T. The impact of the Clean Air Act. *J Pediatr* **161**, 781-786, doi:10.1016/j.jpeds.2012.06.064 (2012).

34 Malthus, T. *An Essay on the Principle of Population.*, (Oxford University Press, 1798).

35 von Liebig, J. *Die organische Chemie in ihrer Anwendung auf Agricultur und Physiologie*. (Vieweg, 1841).

36 Crookes, W. Address of the President Before the British Association for the Advancement of Science, Bristol, 1898. *Science* **8**, 561-575 (1898).

37 Chen, S., Perathoner, S., Ampelli, C. & Centi, G. in *Studies in Surface Science and Catalysis* Vol. 178 (eds Stefania Albonetti, Siglinda Perathoner, & Elsje Alessandra Quadrelli) 31-46 (Elsevier, 2019).

38 Liu, H. Ammonia synthesis catalyst 100 years: Practice, enlightenment and challenge. *Chinese Journal of Catalysis* **35**, 1619-1640, doi:https://doi.org/10.1016/S1872-2067(14)60118-2 (2014).

39 Wang, L. *et al.* Greening Ammonia toward the Solar Ammonia Refinery. *Joule* **2**, 1055-1074, doi:https://doi.org/10.1016/j.joule.2018.04.017 (2018).

40 Rennie, R. *A Dictionary of Chemistry*. (Oxford University Press, 2016).

41 Ertl, G. Surface Science and Catalysis—Studies on the Mechanism of Ammonia Synthesis: The P. H. Emmett Award Address. *Catalysis Reviews* **21**, 201-223, doi:10.1080/03602458008067533 (1980).

42 Mittasch, A. & Frankenburg, W. in *Advances in Catalysis* Vol. 2 (eds W. G. Frankenburg, V. I. Komarewsky, & E. K. Rideal) 81-104 (Academic Press, 1950).

43 Rouwenhorst, K. H. R., Krzywda, P. M., Benes, N. E., Mul, G. & Lefferts, L. in *Techno-Economic Challenges of Green Ammonia as an Energy Vector* (eds Agustin Valera-Medina & Rene Banares-Alcantara) 41-83 (Academic Press, 2021).

44 Dumesic, J. A., Topsøe, H., Khammouma, S. & Boudart, M. Surface, catalytic and magnetic properties of small iron particles: II. Structure sensitivity of ammonia synthesis. *Journal of Catalysis* **37**, 503-512, doi:https://doi.org/10.1016/0021-9517(75)90185-2 (1975).

45 Dumesic, J. A., Topsøe, H. & Boudart, M. Surface, catalytic and magnetic properties of small iron particles: III. Nitrogen induced surface reconstruction. *Journal of Catalysis* **37**, 513-522, doi:https://doi.org/10.1016/0021-9517(75)90186-4 (1975).

46 Somorjai, G. A. & Materer, N. Surface structures in ammonia synthesis. *Topics in Catalysis* **1**, 215-231, doi:10.1007/BF01492277 (1994).

47 Strongin, D. R., Carrazza, J., Bare, S. R. & Somorjai, G. A. The importance of C7 sites and surface roughness in the ammonia synthesis reaction over iron. *Journal of Catalysis* **103**, 213-215, doi:https://doi.org/10.1016/0021-9517(87)90109-6 (1987).

48 Katy, G. S. B. a. L., J R and Lee, J M and Leftin, H P and Katy, P J.S. and Van Dijk, C P. Supplemental ammonia synthesis. United States patent (1986).

49 Jacobsen, C. J. H. *et al.* Structure sensitivity of supported ruthenium catalysts for ammonia synthesis. *Journal of Molecular Catalysis A: Chemical* **163**, 19-26, doi:https://doi.org/10.1016/S1381-1169(00)00396-4 (2000).

50 Forni, L., Molinari, D., Rossetti, I. & Pernicone, N. Carbon-supported promoted Ru catalyst for ammonia synthesis. *Applied Catalysis A: General* **185**, 269-275, doi:https://doi.org/10.1016/S0926-860X(99)00144-1 (1999).

51 Tadros, T. in *Encyclopedia of Colloid and Interface Science* (ed Tharwat Tadros) 820-820 (Springer Berlin Heidelberg, 2013).

52 Mukherjee, S., Devaguptapu, S. V., Sviripa, A., Lund, C. R. F. & Wu, G. Low-temperature ammonia decomposition catalysts for hydrogen generation. *Applied Catalysis B: Environmental* **226**, 162-181, doi:https://doi.org/10.1016/j.apcatb.2017.12.039 (2018).

53 Guthrie, W. L., Sokol, J. D. & Somorjai, G. A. The decomposition of ammonia on the flat (111) and stepped (557) platinum crystal surfaces. *Surface Science* **109**, 390-418, doi:https://doi.org/10.1016/0039-6028(81)90496-9 (1981).

54 Shustorovich, E. & Bell, A. T. Synthesis and decomposition of ammonia on transition metal surfaces: bond-order-conservation-Morse-potential analysis. *Surface Science Letters* **259**, L791-L796, doi:https://doi.org/10.1016/0167-2584(91)90311-E (1991).

55 Ertl, G. & Huber, M. Mechanism and kinetics of ammonia decomposition on iron. *Journal of Catalysis* **61**, 537-539, doi:https://doi.org/10.1016/0021-9517(80)90403-0 (1980).

56 Hashimoto, K. & Toukai, N. Decomposition of ammonia over a catalyst consisting of ruthenium metal and cerium oxides supported on Y-form zeolite. *Journal of Molecular Catalysis A: Chemical* **161**, 171-178, doi:https://doi.org/10.1016/S1381-1169(00)00332-0 (2000).

57 Löffler, D. G. & Schmidt, L. D. Kinetics of NH3 decomposition on iron at high temperatures. *Journal of Catalysis* **44**, 244-258, doi:https://doi.org/10.1016/0021-9517(76)90395-X (1976).

58 Mansilla, C., Avril, S., Imbach, J. & Le Duigou, A. CO2-free hydrogen as a substitute to fossil fuels: What are the targets? Prospective assessment of the hydrogen market attractiveness. *International Journal of Hydrogen Energy* **37**, 9451-9458, doi:https://doi.org/10.1016/j.ijhydene.2012.03.149 (2012).

59 Yin, S. F., Xu, B. Q., Zhou, X. P. & Au, C. T. A mini-review on ammonia decomposition catalysts for on-site generation of hydrogen for fuel cell applications. *Applied Catalysis A: General* **277**, 1-9, doi:https://doi.org/10.1016/j.apcata.2004.09.020 (2004).

60 Tamaru, K. Adsorption measurements during the decomposition of ammonia on a tungsten catalyst. *Transactions of the Faraday Society* **57**, 1410-1415, doi:10.1039/TF9615701410 (1961).

61 Matsushita, K.-I. & Hansen, R. S. Adsorption and Decomposition of Ammonia on a Polycrystalline Tungsten Filament. *Journal of Chemical Physics* **52**, 4877-4889, doi:10.1063/1.1673726 (1970).

62 Danielson, L. R., Dresser, M. J., Donaldson, E. E. & Dickinson, J. T. Adsorption and desorption of ammonia, hydrogen, and nitrogen on ruthenium (0001). *Surface Science* **71**, 599-614, doi:https://doi.org/10.1016/0039-6028(78)90450-8 (1978).

63 Ganley, J. C., Thomas, F. S., Seebauer, E. G. & Masel, R. I. A Priori Catalytic Activity Correlations: The Difficult Case of Hydrogen Production from Ammonia. *Catalysis Letters* **96**, 117-122, doi:10.1023/B:CATL.0000030108.50691.d4 (2004).

64 Hansgen, D. A., Vlachos, D. G. & Chen, J. G. Using first principles to predict bimetallic catalysts for the ammonia decomposition reaction. *Nature Chemistry* **2**, 484-489, doi:10.1038/nchem.626 (2010).

65 Appl, M. in *Ullmann's Encyclopedia of Industrial Chemistry* (2011).

66 Amano, A. & Taylor, H. The Decomposition of Ammonia on Ruthenium, Rhodium and Palladium Catalysts Supported on Alumina. *Journal of the American Chemical Society* **76**, 4201-4204, doi:10.1021/ja01645a057 (1954).

67 Papapolymerou, G. & Bontozoglou, V. Decomposition of NH3 on Pd and Ir Comparison with Pt and Rh. *Journal of Molecular Catalysis A: Chemical* **120**, 165-171, doi:https://doi.org/10.1016/S1381-1169(96)00428-1 (1997).

68 García-García, F. R., Guerrero-Ruiz, A. & Rodríguez-Ramos, I. Role of B5-Type Sites in Ru Catalysts used for the NH3 Decomposition Reaction. *Topics in Catalysis* **52**, 758-764, doi:10.1007/s11244-009-9203-7 (2009).

69 Yin, S.-F. *et al.* Investigation on the catalysis of COx-free hydrogen generation from ammonia. *Journal of Catalysis* **224**, 384-396, doi:https://doi.org/10.1016/j.jcat.2004.03.008 (2004).

70 Yin, S.-F., Xu, B.-Q., Ng, C.-F. & Au, C.-T. Nano Ru/CNTs: a highly active and stable catalyst for the generation of COx-free hydrogen in ammonia decomposition. *Applied Catalysis B: Environmental* **48**, 237-241, doi:https://doi.org/10.1016/j.apcatb.2003.10.013 (2004).

71 Hill, A. K. & Torrente-Murciano, L. In-situ H2 production via low temperature decomposition of ammonia: Insights into the role of cesium as a promoter. *International Journal of Hydrogen Energy* **39**, 7646-7654, doi:https://doi.org/10.1016/j.ijhydene.2014.03.043 (2014).

72 Hill, A. K. & Torrente-Murciano, L. Low temperature H2 production from ammonia using ruthenium-based catalysts: Synergetic effect of promoter and support. *Applied Catalysis B: Environmental* **172-173**, 129-135, doi:https://doi.org/10.1016/j.apcatb.2015.02.011 (2015).

73 Ren, S., Huang, F., Zheng, J., Chen, S. & Zhang, H. Ruthenium supported on nitrogen-doped ordered mesoporous carbon as highly active catalyst for NH3 decomposition to H2. *International Journal of Hydrogen Energy* **42**, 5105-5113, doi:https://doi.org/10.1016/j.ijhydene.2016.11.010 (2017).

74 Bell, T. E., Zhan, G., Wu, K., Zeng, H. C. & Torrente-Murciano, L. Modification of Ammonia Decomposition Activity of Ruthenium

Nanoparticles by N-Doping of CNT Supports. *Topics in Catalysis* **60**, 1251-1259, doi:10.1007/s11244-017-0806-0 (2017).

75 García-García, F. R., Álvarez-Rodríguez, J., Rodríguez-Ramos, I. & Guerrero-Ruiz, A. The use of carbon nanotubes with and without nitrogen doping as support for ruthenium catalysts in the ammonia decomposition reaction. *Carbon* **48**, 267-276, doi:https://doi.org/10.1016/j.carbon.2009.09.015 (2010).

76 Chen, J. *et al.* Effects of nitrogen doping on the structure of carbon nanotubes (CNTs) and activity of Ru/CNTs in ammonia decomposition. *Chemical Engineering Journal* **156**, 404-410, doi:https://doi.org/10.1016/j.cej.2009.10.062 (2010).

77 Marco, Y., Roldán, L., Armenise, S. & García-Bordejé, E. Support-Induced Oxidation State of Catalytic Ru Nanoparticles on Carbon Nanofibers that were Doped with Heteroatoms (O, N) for the Decomposition of NH3. *ChemCatChem* **5**, 3829-3834, doi:https://doi.org/10.1002/cctc.201300455 (2013).

78 Li, L., Zhu, Z. H., Yan, Z. F., Lu, G. Q. & Rintoul, L. Catalytic ammonia decomposition over Ru/carbon catalysts: The importance of the structure of carbon support. *Applied Catalysis A: General* **320**, 166-172, doi:https://doi.org/10.1016/j.apcata.2007.01.029 (2007).

79 Li, G., Kanezashi, M. & Tsuru, T. Catalytic Ammonia Decomposition over High-Performance Ru/Graphene Nanocomposites for Efficient COx-Free Hydrogen Production. *Catalysts* **7**, 23 (2017).

80 Pyrz, W., Vijay, R., Binz, J., Lauterbach, J. & Buttrey, D. J. Characterization of K-Promoted Ru Catalysts for Ammonia Decomposition Discovered Using High-Throughput Experimentation. *Topics in Catalysis* **50**, 180-191, doi:10.1007/s11244-008-9095-y (2008).

81 Huang, C. *et al.* Ru/La2O3 catalyst for ammonia decomposition to hydrogen. *Applied Surface Science* **476**, 928-936, doi:https://doi.org/10.1016/j.apsusc.2019.01.112 (2019).

82 Ju, X. *et al.* Mesoporous Ru/MgO prepared by a deposition-precipitation method as highly active catalyst for producing COx-free hydrogen from ammonia decomposition. *Applied Catalysis B: Environmental* **211**, 167-175, doi:https://doi.org/10.1016/j.apcatb.2017.04.043 (2017).

83 Hu, X.-C. *et al.* Ceria-supported ruthenium clusters transforming from isolated single atoms for hydrogen production via decomposition of ammonia. *Applied Catalysis B: Environmental* **268**, 118424, doi:https://doi.org/10.1016/j.apcatb.2019.118424 (2020).

84 Cui, Z., Gan, J., Fan, J., Xue, Y. & Zhang, R. Size-Dependent Surface Basicity of Nano-CeO2 and Desorption Kinetics of CO2 on Its Surface. *Industrial & Engineering Chemistry Research* **57**, 10977-10984, doi:10.1021/acs.iecr.8b01247 (2018).

85 Li, X.-K., Ji, W.-J., Zhao, J., Wang, S.-J. & Au, C.-T. Ammonia decomposition over Ru and Ni catalysts supported on fumed SiO2,

MCM-41, and SBA-15. *Journal of Catalysis* **236**, 181-189, doi:https://doi.org/10.1016/j.jcat.2005.09.030 (2005).

86 Zhang, J., Xu, H. & Li, W. Kinetic study of NH3 decomposition over Ni nanoparticles: The role of La promoter, structure sensitivity and compensation effect. *Applied Catalysis A: General* **296**, 257-267, doi:https://doi.org/10.1016/j.apcata.2005.08.046 (2005).

87 Liu, H., Wang, H., Shen, J., Sun, Y. & Liu, Z. Promotion effect of cerium and lanthanum oxides on Ni/SBA-15 catalyst for ammonia decomposition. *Catalysis Today* **131**, 444-449, doi:https://doi.org/10.1016/j.cattod.2007.10.048 (2008).

88 Zheng, W., Zhang, J., Ge, Q., Xu, H. & Li, W. Effects of CeO2 addition on Ni/Al2O3 catalysts for the reaction of ammonia decomposition to hydrogen. *Applied Catalysis B: Environmental* **80**, 98-105, doi:https://doi.org/10.1016/j.apcatb.2007.11.008 (2008).

89 Hu, X.-C. *et al.* Transition metal nanoparticles supported La-promoted MgO as catalysts for hydrogen production via catalytic decomposition of ammonia. *Journal of Energy Chemistry* **38**, 41-49, doi:https://doi.org/10.1016/j.jechem.2018.12.024 (2019).

90 Zhang, H. *et al.* Controlling Co-support interaction in Co/MWCNTs catalysts and catalytic performance for hydrogen production via NH3 decomposition. *Applied Catalysis A: General* **464-465**, 156-164, doi:https://doi.org/10.1016/j.apcata.2013.05.046 (2013).

91 Zhang, H. *et al.* Tuning catalytic performances of cobalt catalysts for clean hydrogen generation via variation of the type of carbon support and catalyst post-treatment temperature. *International Journal of Hydrogen Energy* **39**, 17573-17582, doi:https://doi.org/10.1016/j.ijhydene.2014.07.183 (2014).

92 Podila, S., Alhamed, Y. A., AlZahrani, A. A. & Petrov, L. A. Hydrogen production by ammonia decomposition using Co catalyst supported on Mg mixed oxide systems. *International Journal of Hydrogen Energy* **40**, 15411-15422, doi:https://doi.org/10.1016/j.ijhydene.2015.09.057 (2015).

93 Torrente-Murciano, L., Hill, A. K. & Bell, T. E. Ammonia decomposition over cobalt/carbon catalysts—Effect of carbon support and electron donating promoter on activity. *Catalysis Today* **286**, 131-140, doi:https://doi.org/10.1016/j.cattod.2016.05.041 (2017).

94 The role of hydrogen and ammonia in meeting the net zero challenge. (The Royal Society, 2021).

95 Lee, T.-L. & Duncan, D. A. A Two-Color Beamline for Electron Spectroscopies at Diamond Light Source. *Synchrotron Radiation News* **31**, 16-22, doi:10.1080/08940886.2018.1483653 (2018).

96 Dent, A. J. *et al.* B18: A core XAS spectroscopy beamline for Diamond. *Journal of Physics: Conference Series* **190**, 012039, doi:10.1088/1742-6596/190/1/012039 (2009).

97 Ravel, B. a. N., M. *ATHENA, ARTEMIS, HEPHAESTUS*: data analysis for X-ray absorption spectroscopy using *IFEFFIT*. *Journal of*

Synchrotron Radiation **12**, 537-541, doi:10.1107/S0909049505012719 (2005).

98 Wang, S. J. *et al.* Investigation on modification of Ru/CNTs catalyst for the generation of COx-free hydrogen from ammonia. *Applied Catalysis B: Environmental* **52**, 287-299, doi:https://doi.org/10.1016/j.apcatb.2004.05.002 (2004).

99 Paleo, A. J. *et al.* Vapor grown carbon nanofiber based cotton fabrics with negative thermoelectric power. *Cellulose* **27**, 9091-9104, doi:10.1007/s10570-020-03391-4 (2020).

100 Burwell, T. *et al.* Direct formation of copper nanoparticles from atoms at graphitic step edges lowers overpotential and improves selectivity of electrocatalytic CO2 reduction. *Communications Chemistry* **7**, 140, doi:10.1038/s42004-024-01218-y (2024).

101 del Carmen Gimenez-Lopez, M., Kurtoglu, A., Walsh, D. A. & Khlobystov, A. N. Extremely Stable Platinum-Amorphous Carbon Electrocatalyst within Hollow Graphitized Carbon Nanofibers for the Oxygen Reduction Reaction. *Advanced Materials* **28**, 9103-9108, doi:https://doi.org/10.1002/adma.201602485 (2016).

102 Popov, I. *et al.* Chemical Kinetics of Metal Single Atom and Nanocluster Formation on Surfaces: An Example of Pt on Hexagonal Boron Nitride. *Nano Letters* **23**, 8006-8012, doi:10.1021/acs.nanolett.3c01968 (2023).

103 Kang, S. *et al.* Heteroepitaxial Growth of B5-Site-Rich Ru Nanoparticles Guided by Hexagonal Boron Nitride for Low-Temperature Ammonia Dehydrogenation. *Advanced Materials* **35**, 2203364, doi:https://doi.org/10.1002/adma.202203364 (2023).

104 Mazzone, S. *et al.* Ruthenium-based catalysts supported on carbon xerogels for hydrogen production via ammonia decomposition. *Applied Catalysis A: General* **632**, 118484, doi:https://doi.org/10.1016/j.apcata.2022.118484 (2022).

105 Lucentini, I., Casanovas, A. & Llorca, J. Catalytic ammonia decomposition for hydrogen production on Ni, Ru and NiRu supported on CeO2. *International Journal of Hydrogen Energy* **44**, 12693-12707, doi:https://doi.org/10.1016/j.ijhydene.2019.01.154 (2019).

106 Hu, Z., Mahin, J., Datta, S., Bell, T. E. & Torrente-Murciano, L. Ru-Based Catalysts for H2 Production from Ammonia: Effect of 1D Support. *Topics in Catalysis* **62**, 1169-1177, doi:10.1007/s11244-018-1058-3 (2019).

107 Takahashi, A. & Fujitani, T. Kinetic Analysis of Decomposition of Ammonia over Nickel and Ruthenium Catalysts. *JOURNAL OF CHEMICAL ENGINEERING OF JAPAN* **49**, 22-28, doi:10.1252/jcej.14we431 (2016).

108 Bell, T. E., Zhan, G., Wu, K., Zeng, H. C. & Torrente-Murciano, L. Modification of Ammonia Decomposition Activity of Ruthenium Nanoparticles by N-Doping of CNT Supports. *Top Catal* **60**, 1251-1259, doi:10.1007/s11244-017-0806-0 (2017).

109 Wang, L., Chen, J., Ge, L., Rudolph, V. & Zhu, Z. Difference in the cooperative interaction between carbon nanotubes and Ru particles loaded on their internal/external surface. *RSC Advances* **3**, 12641-12647, doi:10.1039/C3RA41208C (2013).

110 Zheng, W. *et al.* Structure–Function Correlations for Ru/CNT in the Catalytic Decomposition of Ammonia. *ChemSusChem* **3**, 226-230, doi:https://doi.org/10.1002/cssc.200900217 (2010).

111 Duan, X. *et al.* Carbon Nanofiber-Supported Ru Catalysts for Hydrogen Evolution by Ammonia Decomposition. *Chinese Journal of Catalysis* **31**, 979-986, doi:https://doi.org/10.1016/S1872-2067(10)60097-6 (2010).

112 Zhang, S. *et al.* In-Situ Studies of Nanocatalysis. *Accounts of Chemical Research* **46**, 1731-1739, doi:10.1021/ar300245g (2013).

113 Tao, F. & Crozier, P. A. Atomic-Scale Observations of Catalyst Structures under Reaction Conditions and during Catalysis. *Chemical Reviews* **116**, 3487-3539, doi:10.1021/cr5002657 (2016).

114 Aygün, M. *et al.* Palladium Nanoparticles Hardwired in Carbon Nanoreactors Enable Continually Increasing Electrocatalytic Activity During the Hydrogen Evolution Reaction. *ChemSusChem* **14**, 4973-4984, doi:https://doi.org/10.1002/cssc.202101236 (2021).

115 Larichev, Y. V., Moroz, B. L. & Bukhtiyarov, V. I. Electronic state of ruthenium deposited onto oxide supports: An XPS study taking into account the final state effects. *Applied Surface Science* **258**, 1541-1550, doi:https://doi.org/10.1016/j.apsusc.2011.09.127 (2011).

116 MacFarlane, D. R. *et al.* A Roadmap to the Ammonia Economy. *Joule* **4**, 1186-1205, doi:https://doi.org/10.1016/j.joule.2020.04.004 (2020).

117 Jeon, N. *et al.* Y-Doped BaCeO3 Perovskite-Supported Ru Catalysts for COx-Free Hydrogen Production from Ammonia: Effect of Strong Metal–Support Interactions. *ACS Sustainable Chemistry & Engineering* **10**, 15564-15573, doi:10.1021/acssuschemeng.2c04995 (2022).

118 Murakami, K. & Sekine, Y. Recent progress in use and observation of surface hydrogen migration over metal oxides. *Physical Chemistry Chemical Physics* **22**, 22852-22863, doi:10.1039/D0CP04139D (2020).

119 Czerw, R. *et al.* Identification of Electron Donor States in N-Doped Carbon Nanotubes. *Nano Letters* **1**, 457-460, doi:10.1021/nl015549q (2001).

120 Yin, S. F. *et al.* Carbon nanotubes-supported Ru catalyst for the generation of COx-free hydrogen from ammonia. *Catalysis Today* **93-95**, 27-38, doi:https://doi.org/10.1016/j.cattod.2004.05.011 (2004).

121 Kohlrausch, E. C. *et al.* A high-throughput, solvent free method for dispersing metal atoms directly onto supports. *Journal of Materials Chemistry A* **9**, 26676-26679, doi:10.1039/D1TA08372D (2021).

122 Agasti, N. *et al.* Cerium Oxide Nanoparticles Inside Carbon Nanoreactors for Selective Allylic Oxidation of Cyclohexene. *Nano Letters* **20**, 1161-1171, doi:10.1021/acs.nanolett.9b04579 (2020).

123 Rance, G. A., Solomonsz, W. A. & Khlobystov, A. N. Click chemistry in carbon nanoreactors. *Chemical Communications* **49**, 1067-1069, doi:10.1039/C2CC38035H (2013).

124 Lebedeva, M. A. *et al.* Chemical reactions at the graphitic step-edge: changes in product distribution of catalytic reactions as a tool to explore the environment within carbon nanoreactors. *Nanoscale* **8**, 11727-11737, doi:10.1039/C6NR03360A (2016).

125 Aygün, M., Chamberlain, T. W., Gimenez-Lopez, M. d. C. & Khlobystov, A. N. Magnetically Recyclable Catalytic Carbon Nanoreactors. *Advanced Functional Materials* **28**, 1802869, doi:https://doi.org/10.1002/adfm.201802869 (2018).

126 García-García, F. R., Gallegos-Suarez, E., Fernández-García, M., Guerrero-Ruiz, A. & Rodríguez-Ramos, I. Understanding the role of oxygen surface groups: The key for a smart ruthenium-based carbon-supported heterogeneous catalyst design and synthesis. *Applied Catalysis A: General* **544**, 66-76, doi:https://doi.org/10.1016/j.apcata.2017.06.030 (2017).

127 Lodge, R. W., Rance, G. A., Fay, M. W. & Khlobystov, A. N. Movement of palladium nanoparticles in hollow graphitised nanofibres: the role of migration and coalescence in nanocatalyst sintering during the Suzuki–Miyaura reaction. *Nanoscale* **10**, 19046-19051, doi:10.1039/C8NR05267K (2018).

128 Cao, K. *et al.* Atomic mechanism of metal crystal nucleus formation in a single-walled carbon nanotube. *Nature Chemistry* **12**, 921-928, doi:10.1038/s41557-020-0538-9 (2020).

129 Cao, K. *et al.* Comparison of atomic scale dynamics for the middle and late transition metal nanocatalysts. *Nature Communications* **9**, 3382, doi:10.1038/s41467-018-05831-z (2018).

130 Biroju, R. K. *et al.* Pt147 Nanoclusters Soft-Landed on WS2 Nanosheets for Catalysis and Energy Harvesting. *ACS Applied Nano Materials* **4**, 13140-13148, doi:10.1021/acsanm.1c02683 (2021).

131 Sutter, P. W., Flege, J.-I. & Sutter, E. A. Epitaxial graphene on ruthenium. *Nature Materials* **7**, 406-411, doi:10.1038/nmat2166 (2008).

132 Jovanović, A. Z., Mentus, S. V., Skorodumova, N. V. & Pašti, I. A. Reactivity Screening of Single Atoms on Modified Graphene Surface: From Formation and Scaling Relations to Catalytic Activity. *Advanced Materials Interfaces* **8**, 2001814, doi:https://doi.org/10.1002/admi.202001814 (2021).

133 Ward, M. R., Mitchell, R. W., Boyes, E. D. & Gai, P. L. Visualization of atomic scale reaction dynamics of supported nanocatalysts during oxidation and ammonia synthesis using in-situ environmental (scanning) transmission electron microscopy. *Journal of Energy Chemistry* **57**, 281-290, doi:https://doi.org/10.1016/j.jechem.2020.08.069 (2021).

134 Matsubara, Y., Fujita, E., Doherty, M. D., Muckerman, J. T. & Creutz, C. Thermodynamic and Kinetic Hydricity of Ruthenium(II) Hydride

Complexes. *Journal of the American Chemical Society* **134**, 15743-15757, doi:10.1021/ja302937q (2012).

135 Fryzuk, M. D., Petrella, M. J., Coffin, R. C. & Patrick, B. O. Hydride complexes of ruthenium derived from the heterolytic activation of dihydrogen by amidophosphine complexes. *Comptes Rendus. Chimie* **5**, 451-460, doi:10.1016/s1631-0748(02)01403-0 (2002).

136 Dahl, S. *et al.* Role of Steps in ${\mathrm{N}}_{2}$ Activation on Ru(0001). *Physical Review Letters* **83**, 1814-1817, doi:10.1103/PhysRevLett.83.1814 (1999).

137 Ding, J. *et al.* Confined Ru Nanocatalysts on Surface to Enhance Ammonia Synthesis: An In situ ETEM Study. *ChemCatChem* **13**, 534-538, doi:https://doi.org/10.1002/cctc.202001423 (2021).

138 Ishikawa, A., Doi, T. & Nakai, H. Catalytic performance of Ru, Os, and Rh nanoparticles for ammonia synthesis: A density functional theory analysis. *Journal of Catalysis* **357**, 213-222, doi:https://doi.org/10.1016/j.jcat.2017.11.018 (2018).

139 Hayashi, F. *et al.* Ammonia decomposition by ruthenium nanoparticles loaded on inorganic electride C12A7:e−. *Chemical Science* **4**, 3124-3130, doi:10.1039/C3SC50794G (2013).

140 Arevalo, R. L., Aspera, S. M., Sison Escaño, M. C., Nakanishi, H. & Kasai, H. First principles study of methane decomposition on B5 step-edge type site of Ru surface. *Journal of Physics: Condensed Matter* **29**, 184001, doi:10.1088/1361-648X/aa66c7 (2017).

141 Casey-Stevens, C. A., Lambie, S. G., Ruffman, C., Skúlason, E. & Garden, A. L. Geometric and Electronic Effects Contributing to N2 Dissociation Barriers on a Range of Active Sites on Ru Nanoparticles. *The Journal of Physical Chemistry C* **123**, 30458-30466, doi:10.1021/acs.jpcc.9b09563 (2019).

142 the Royal Society, p. b. Ammonia: zero-carbon fertiliser, fuel and energy store. (2020).